



HAL
open science

Control of Excitonic Properties of Transition Metal Dichalcogenides Monolayers

Bo Han

► **To cite this version:**

Bo Han. Control of Excitonic Properties of Transition Metal Dichalcogenides Monolayers. Physics [physics]. INSA de Toulouse, 2020. English. NNT : 2020ISAT0021 . tel-03346369

HAL Id: tel-03346369

<https://theses.hal.science/tel-03346369>

Submitted on 16 Sep 2021

HAL is a multi-disciplinary open access archive for the deposit and dissemination of scientific research documents, whether they are published or not. The documents may come from teaching and research institutions in France or abroad, or from public or private research centers.

L'archive ouverte pluridisciplinaire **HAL**, est destinée au dépôt et à la diffusion de documents scientifiques de niveau recherche, publiés ou non, émanant des établissements d'enseignement et de recherche français ou étrangers, des laboratoires publics ou privés.

Université Fédérale



Toulouse Midi-Pyrénées

THÈSE

En vue de l'obtention du
DOCTORAT DE L'UNIVERSITÉ DE TOULOUSE
Délivré par l'Institut National des Sciences Appliquées de
Toulouse

Présentée et soutenue par

Bo HAN

Le 16 septembre 2020

Contrôle des Propriétés Excitoniques de Monocouches de
Dichalcogénures de Métaux de Transition

Ecole doctorale : **SDM - SCIENCES DE LA MATIERE - Toulouse**

Spécialité : **Nanophysique**

Unité de recherche :

LPCNO-IRSAMC - Laboratoire de Physique et Chimie des Nano-Objets

Thèse dirigée par

Xavier MARIE et Cédric ROBERT

Jury

Mme Catherine JOURNET-GAUTIER, Rapporteur

M. Guillaume CASSABOIS, Rapporteur

M. Fabian CADIZ, Examineur

Mme Bénédicte WAROT-FONROSE, Examinatrice

M. Xavier MARIE, Directeur de thèse

M. Cédric ROBERT, Co-directeur de thèse

Université Fédérale



Toulouse Midi-Pyrénées

THÈSE

**En vue de l'obtention du
DOCTORAT DE L'UNIVERSITÉ DE TOULOUSE
Délivré par l'Institut National des Sciences Appliquées de
Toulouse**

Présentée et soutenue par

Bo HAN

Le 16 septembre 2020

**Contrôle des Propriétés Excitoniques de Monocouches de
Dichalcogénures de Métaux de Transition**

Ecole doctorale : **SDM - SCIENCES DE LA MATIERE - Toulouse**

Spécialité : **Nanophysique**

Unité de recherche :

LPCNO-IRSAMC - Laboratoire de Physique et Chimie des Nano-Objets

Thèse dirigée par

Xavier MARIE et Cédric ROBERT

Jury

Mme Catherine JOURNET-GAUTIER, Rapporteure

M. Guillaume CASSABOIS, Rapporteur

M. Fabian CADIZ, Examineur

Mme Bénédicte WAROT-FONROSE, Examinatrice

M. Xavier MARIE, Directeur de thèse

M. Cédric ROBERT, Co-directeur de thèse

“為天地立心，為生民立命，為往聖繼絕學，為萬世開太平。”

——張載，北宋

Contents

Acknowledgements	I
List of publications and conferences	IV
Abstract	V
Résumé en Français	VI
Introduction	VII
1 Transition Metal Dichalcogenides	1
1.1 Crystal symmetry and band structure	2
1.2 Exciton states	5
1.3 Spin/Valley polarization	8
1.4 Van der Waals heterostructure	9
2 Experimental Techniques	10
2.1 Sample fabrication	11
2.1.1 All-dry viscoelastic stamping method and fabrication setups . . .	11
2.1.2 Identification of TMD monolayer and measurement of hBN thickness	12
2.2 Optical spectroscopy experiments	14
2.2.1 Confocal microscopy setups	14
2.2.2 Differential Reflectivity	17
2.2.3 Photoluminescence	21
2.3 Effects of hBN encapsulation on the optical and exciton properties	24
2.4 Conclusion	25
3 Spin-Forbidden Dark Excitons in MoSe₂ and MoS₂ Monolayers	26
3.1 Exciton fine structures in TMD Monolayers	27
3.1.1 Symmetry analysis of exciton states	28
3.1.2 Exciton states coupling and interaction with magnetic field	29
3.2 Spin-forbidden dark excitons in MoSe ₂ monolayer	31
3.3 Spin-forbidden dark excitons in MoS ₂ monolayer	35
3.4 Conclusion	40
4 Control of the Exciton Radiative Lifetime and Linewidth	41
4.1 Homogeneous linewidth	42
4.2 Purcell effect	44
4.3 Simulation of the optical field intensity	44
4.4 Sample fabrication and experimental methods	46

4.4.1	Sample Fabrication	46
4.4.2	Experimental methods	47
4.5	Tuning of the spontaneous emission rate	48
4.5.1	Purcell effect on neutral exciton dynamics and linewidth	48
4.5.2	Relaxation and recombination dynamics of exciton and trion	54
4.6	Conclusion	58
5	Exciton Upconversion in Transition Metal Dichalcogenide Monolayers	59
5.1	Upconversion in MoSe ₂ and MoTe ₂ monolayers	60
5.1.1	Upconversion probed in MoSe ₂ monolayers	61
5.1.2	Exciton states in MoTe ₂ monolayer	63
5.1.3	Energy separations between A:1s and A:2s states	66
5.2	Model on exciton upconversion	68
5.2.1	General upconversion regimes in semiconductors	68
5.2.2	Resonant interband Auger process	69
5.3	Conclusion	78
	Conclusions	79
	Perspectives	82
A	Other Exciton Upconversion Mechanisms	85
A.1	Resonant intraband Auger process	85
A.2	Two step absorption	87
	Bibliography	89

Acknowledgements



Neon Sunset along Garonne River, Toulouse, France.

Three years ago, I was thrilled to be accepted as a PhD student of the Quantum Optoelectronics group in LPCNO, INSA. Toulouse is a picturesque and charming city. Toulousain are so nice that I do not even feel isolated, though this was the first time I spent years abroad. The pillaring aerospace manufacturer, the pride of France, Airbus, headquarters Toulouse. I will always remember the neon sunset and jet contrail along the Garonne river. From here, I know the key ingredient to a good science is actually people. Our group has the best members that rejoice each other and work together to defend our excellent scientific reputations. This three-year PhD has been the treasure of my life.

I would first express my gratitude to Catherine JOURNET-GAUTIER, Guillaume CASSABOIS, Fabian CADIZ and Bénédicte WAROT-FONROSE to join the jury of my PhD defense in this hard time. They have given very professional and strict examinations on the quality of this thesis.

Tons of gratitudes to my PhD supervisors, Xavier MARIE and Cédric ROBERT. Both of them are the strongest supports of our group to ensure we survive this competitive research field. I was really bad at writing. I hope Xavier and Cédric did not suffer too much on the manuscript. Xavier is the top-of-line guy in this field with a strong spirit and personality. We stay in the same office, which ensures we can discuss very often. He is extremely patient to the me and makes things easier to understand. Cédric is an outstanding CNRS agent in charge of the experiments and setups in our group. If you

consider the entire France has only three or four positions in our field and Cédric got it, you would believe he is a badass guy. I have learned lots of experimental skills and techniques from him. The efforts I have made with them guarantee the accomplishment of this thesis.

Bernhard URBASZEK is our “bartender” who take cares of everything. He is absolutely one of the strongest supports to the group. I appreciate his optimistic attitudes towards everything. Bernhard cheers up the PhDs and Postdocs when we are in low mood. We discussed many things from excitons to swimming pools. He is able to make the situations not so disappointing and always comes up a way to solve the problem. Thanks to Bernhard for organizing the picnic before my flight departure. Next time Bernhard comes to China, I will introduce to him my parents who have much better cooking skills than me.

Thierry AMAND is an honored member of our group. He is really passionated guy about Physics. Though he retired last year, he pays constant visit to the group. We worked together on the spin-forbidden dark excitons on the Molybdenum-based TMD MLs, the complex group theory and numerical fittings. I am really glad that Thierry came to my PhD defense. Talking with Thierry is like reading an encyclopedia. Amazing and personable guy he is. I hope Thierry stay healthy and happy.

Delphine LARGARDE is our “baby sitter” . She manages all the setups and fundings. I am glad that I did not mess up with the setups and cause too many troubles for her during this three years. I will remember the sweet chocolate cookies from Delphine.

Emmanuel Courtade is my “golden boy” . He is a reliable friend. We talked about everything like Physics, boring sample fabrications, job hunting, tinder and fun things. We worked together on the experimental part of the PRX paper of exciton upconversion. I have learned many good qualities from Emmanuel. I wish him good luck in the future, with both the life and work. If possible he comes to China, we probably will go the Chongqing hotpot again that conquered his french appetite when we were in Paris.

Shivangi SHREE starts the PhD research a few months before me. We worked on the experimental parts of the PRB paper of exciton-phonon coupling. Shivangi is really kind-hearted and willing to try new things. I think she will become a good swimmer and good luck for her Postdoc work in Seattle and a good future life.

Pierre RENUCCI is the “sweet heart” , very charming french gentleman. We spent several days in the cold Denver and then were told that the APS March meeting was cancelled. Not so bad experiences with Pierre in Denver on the matches of Real Madrid smashing FC Barcelona and Denver Nuggets nailing down Toronto Raptors.

Andrea BALOCCHI, Hélène CARRERE and Laurent LOMBEZ are the permanent members of our group. They are specialist in semiconductor, spin physics and solar cells. Even though we do not work in same field, it is good to know these interesting researches in the group. I will remember the nice swimming experiences with Andrea and Alejandro. I hope we could do more training if there is no Covid-19. Good luck for Laurent on his work and the AFM measurement that takes plenty of time.

Jean-François LEHERISSIER and Lei REN are our new members. Jean-François was our technician. He would check if everything is alright when he walks by and fixes things. I hope him good luck in Bordeaux. Lei is a young PhD student in the group. I somehow recruited him. I hope Lei makes some badass physics during his PhD and figure out what

he is really up to in the future. Congratulations to Lei for getting the french driving license, something I wanted but did not manage.

Our former Postdocs Gang WANG and Honghua FANG were someones really important to me. We all have backgrounds from Jilin University. Gang guided me to the Toulouse group and then started his adventures in Cambridge. He really helped me to solve many confusions about work and life. Gang won “Thousand Talent Program” for young outstanding scientists and got an academic position in Beijing Institute of Technology. I hope him to continue the scientific success. Honghua spent one year in Toulouse. We worked together on many projects, for example the PRL paper of controlling the spontaneous emission rate. Honghua also won “Thousand Talent Program” for young outstanding scientists and got an academic position in Qinghua University in Beijing. His family had some difficulties, but now everything is back on track. I wish his family to be happy, healthy and safe especially after baby Yikai comes to the world.

Ioannis PARADEISANOS, Joshya Shyamala RAJAGOPAL and Hans TORNATZKY are our new Postdocs. They are all motivated and ambitious researchers. Ioannis shares very practical information with me on finding a Postdoc. We get along initially because of Gang. Ioannis is a man of focus and commitment and sheer will like John WICK, a good Physicist and sportsman. He is an Olympic level swimmer. If there were no lock-down, I would like to have more training with Ioannis. I will bluff with my friends I could have a chance to swim with an Olympic level guy. Joshya is a really nice lady. I was surprised to know she worked one-year Postdoc in Changchun, the place I came from. Yeah, a nice place with freezing coldness around -30°C in winter. That should be a quite unique experience for her. I hope Joshya keeps the positive life attitude like she always is. Hans came to our group in this summer. I can feel that this dude is really knowledgeable and humble. He knows many details of the setups I didn't even pay attention to. Hans also makes very delicious cakes, the best ones I have ever tried. Good luck for Hans on the experiments of TMD ML/Ferromagnet heterostructures.

I would also express my great gratitudes to our collaborators Mikhail M. GLAZOV, Marina M. SEMINA and Leonid E. GOLUB for developing theoretical models to explain our experimental results. They are all top-of-line theorist in this field. Also gratitude to Kenji WATANABE and Takashi TANAGUCHI for providing high quality hBN crystals which play a key role in our experiments. Many thanks to Clément FAUGERAS and Marek POTEMSKI for their collaboration on the measurements of the spin-forbidden dark excitons in large magnetic field.

My girlfriend, Yang ZHANG, is very supportive to “almost all” of my decisions. We have been through all the high and low. After these years, we know each other well and make ourselves better than who we used to be. Yeah, I will hold this woman's hands, marry her and spend my entire life with her.

Finally, I would thank the supports from China Scholarship Council for my PhD. During the final year of my PhD, Coronavirus (2019-Covid) broke out. When I am writing this now, people are still losing lives and their beloved ones. I do not know how it is going to evolve, but I have seen people showing enormous courage against this disaster. We can make it through.

List of publications and conferences

- C. Robert, **B. Han**, P. Kapuscinski, A. Delhomme, C. Faugeras, T. Amand, M.R. Molas, M. Bartos, K. Watanabe, T. Taniguchi, B. Urbaszek, M. Potemski and X. Marie. Measurement of the Spin-forbidden Dark Excitons in MoS₂ and MoSe₂ Monolayers. *Nature Communications*, 2020, 11:4037.
 - H. H. Fang, **B. Han**, C. Robert, M. A. Semina, D. Lagarde, E. Courtade, T. Taniguchi, K. Watanabe, T. Amand, B. Urbaszek, M. M. Glazov and X. Marie. Control of the Exciton Radiative Lifetime in van der Waals Heterostructures. *Physical Review Letters*, 2019, 123(6): 067401.
 - A. Francisco-López, **B. Han**, D. Lagarde, X. Marie, B. Urbaszek, C. Robert, A. Goñi. On the Impact of the Stress Situation on the Optical Properties of WSe₂ Monolayers Under High Pressure. *Papers in Physics*, 2019, 11: 110005.
 - **B. Han**, C. Robert, E. Courtade, M. Manca, S. Shree, T. Amand, P. Renucci, T. Taniguchi, K. Watanabe, X. Marie, L. E. Golub, M. M. Glazov and B. Urbaszek. Exciton States in Monolayer MoSe₂ and MoTe₂ Probed by Upconversion Spectroscopy. *Physical Review X*, 2018, 8(3): 031073.
 - E. Courtade, **B. Han**, S. Nakhaie, C. Robert, X. Marie, P. Renucci, T. Taniguchi, K. Watanabe, L. Geelhaar, J. M. J. Lopes, and B. Urbaszek. Spectrally Narrow Exciton Luminescence from Monolayer MoS₂ and MoSe₂ Exfoliated onto Epitaxially Grown Hexagonal BN. *Applied Physics Letters*, 2018, 113(3): 032106.
 - S. Shree, M. Semina, C. Robert, **B. Han**, T. Amand, A. Balocchi, M. Manca, E. Courtade, X. Marie, T. Taniguchi, K. Watanabe, M. M. Glazov, and B. Urbaszek. Observation of Exciton-Phonon Coupling in MoSe₂ Monolayers. *Physical Review B*, 2018, 98(3): 035302.
-
- Accepted oral presentation titled “Engineering the Exciton Spontaneous Emission Time in MoSe₂ Monolayer” . American Physical Society March Meeting, 2020, Denver, Colorado, US.
 - Oral presentation titled “Control of the Radiative Lifetimes in van der Waals Heterostructures” . Graphene and Co annual meeting, 2019, Bad Herrenalb, Germany.
 - Poster “Excitonic Properties of hBN/WSe₂/hBN van der Waals Heterostructures Under Hydrostatic Pressure” . 18th International Conference on High Pressure Semiconducting Physics and 2nd International Workshop on High Pressure Study of Superconductors, 2018, Barcelona, Spain.

Abstract

The spectacular progress in controlling the electronic properties of graphene has triggered research in alternative atomically thin two-dimensional (2D) crystals. Nowadays, 2D materials properties cover almost every phenomenon in condensed matter physics such as magnetism, superconductivity, optoelectronics, spintronics, topological insulation and many more.

2D semiconductors based on Transition Metal Dichalcogenides (TMD), such as MoS₂, are very promising nanostructures for optical and electronic applications. 2H-phase TMD materials have a layer thickness dependent band structure: indirect bandgap for a number of layers ≥ 2 , while the monolayer form has a direct bandgap located at the K points of the 2D hexagonal Brillouin zone. The optical properties of TMD thin layers are governed by Coulomb bound electron-hole pair, *i.e.* exciton, with giant binding energy of a few hundreds of meV. In monolayers (ML), the interplay between the absence of inversion symmetry and the spin-orbit interaction yields very unique optical selection rules: valley selective circular dichroism arises as a consequence of the coupling between spin and valley physics.

In this thesis, we use an all-dry viscoelastic stamping method to fabricate high-quality van der Waals heterostructures based on TMD materials. Thanks to the use of hexagonal boron nitride (hBN, large indirect gap semiconductor) as encapsulation layers, we show that the exciton linewidth of TMD monolayer is narrowed, approaching the homogeneous limit (1-4 meV). This improvement of optical properties allows us to explore the long-disputing exciton fine structure in Molybdenum-based TMD MLs. We performed magneto-photoluminescence experiments up to 30 T to brighten the dark exciton states. The bright excitons are measured 1.4 meV below the dark ones in MoSe₂ ML, whereas the ordering is opposite for MoS₂ ML with bright states 14 meV above the dark states. Thanks to the reduction of dielectric disorder in encapsulated MoSe₂ monolayers, we also demonstrate the control of exciton radiative lifetime and linewidth as a result of the Purcell effect by simply tuning the bottom hBN thickness. Finally we use various optical spectroscopy techniques to reveal the exciton excited states in MoTe₂ MLs for the first time. Exciton upconversion is observed in all TMD monolayers that we have investigated: MoS₂, MoSe₂, MoTe₂ and WSe₂. It is interpreted as a consequence of very efficient resonant interband Auger processes. These detailed studies help us better understand the physics of 2D TMD semiconductors and pave the way for future photonic and optoelectronic applications.

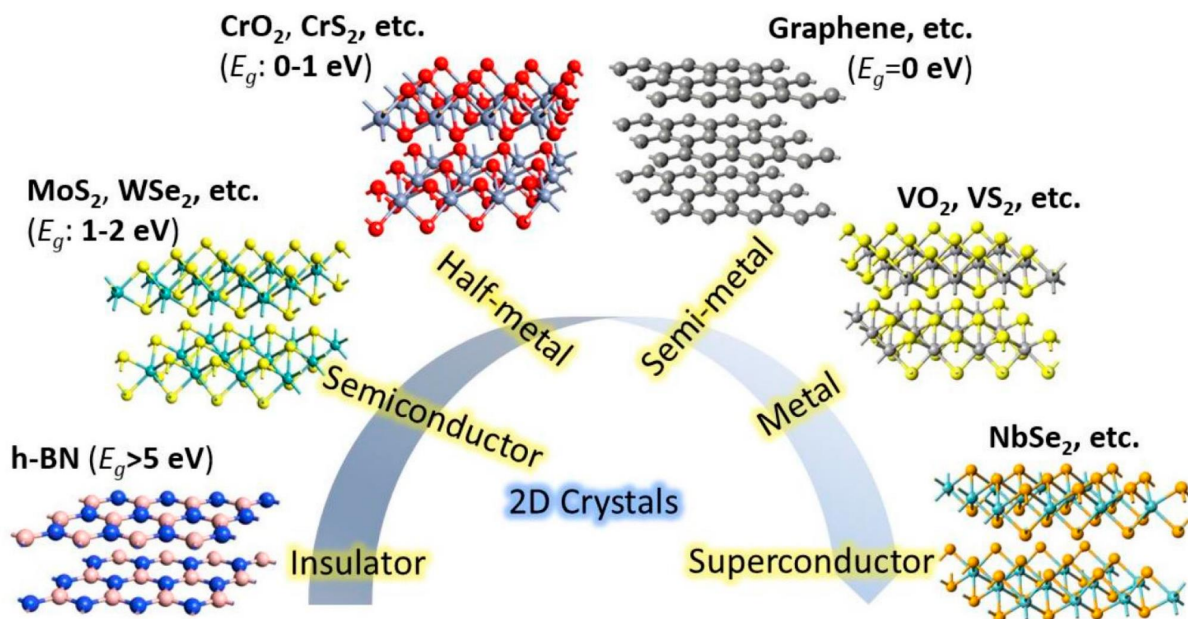
Résumé en Français

Les progrès spectaculaires réalisés sur le contrôle des propriétés électroniques du graphène ont stimulé la recherche de nouveaux cristaux bidimensionnels (2D). De nos jours, les propriétés des matériaux 2D couvrent presque tous les phénomènes de la physique de la matière condensée tels que le magnétisme, la supraconductivité, l'optoélectronique, la spintronique, l'isolation topologique et bien d'autres.

Les semiconducteurs 2D basés sur les dichalcogénures de métaux de transition (TMD), tels que MoS_2 , sont des nanostructures très prometteuses pour les applications optiques et électroniques. Les matériaux TMD en phase 2H ont une structure de bande dépendante de l'épaisseur : semiconducteur à bande interdite indirecte pour un nombre de couches ≥ 2 , tandis que la forme monocouche a une bande interdite directe située aux points K de la zone Brillouin hexagonale 2D. Les propriétés optiques de ces couches ultra-minces à base de TMD sont régies par des excitons, paires électron-trou en interaction coulombienne, avec des énergies de liaison géante pouvant atteindre quelques centaines de meV. Dans les monocouches (ML), l'effet combiné de l'absence de symétrie d'inversion et de l'interaction spin-orbite donne des règles de sélection optique uniques: un dichroïsme circulaire sélectif en vallée résulte du couplage entre la physique du spin et la physique de vallée.

Dans cette thèse, nous utilisons des méthodes d'exfoliation/transfert déterministe pour fabriquer des hétérostructures de van der Waals de grande qualité à base de matériaux TMD. Grâce à l'utilisation de nitrure de Bore hexagonal (hBN, semi-conducteur à grande bande interdite) comme couches d'encapsulation, nous montrons que la largeur de raie excitonique de la monocouche TMD est rétrécie, s'approchant de la limite homogène (1-4 meV). Cette amélioration des propriétés optiques nous permet d'explorer la structure fine fortement débattue des excitons dans les monocouches TMD à base de molybdène. Nous avons effectué des expériences de magnéto-photoluminescence jusqu'à 30 T pour mettre en évidence les excitons noirs. Les excitons brillants sont mesurés 1,4 meV en dessous des états noirs dans MoSe_2 , tandis que l'ordre est opposé pour les monocouches de MoS_2 avec des états brillants 14 meV au dessus des états sombres. Grâce à la réduction du désordre diélectrique dans les monocouches MoSe_2 encapsulées, nous démontrons également le contrôle du temps de vie radiatif de l'exciton et de sa largeur de raie par effet Purcell, en réglant simplement l'épaisseur de la couche hBN inférieure. Enfin, nous avons mis en œuvre plusieurs techniques de spectroscopie optique pour révéler les états excitoniques excités pour la première fois dans les monocouches MoTe_2 . La conversion d'exciton (« up-conversion ») est observée dans toutes les monocouches TMD que nous avons étudiées: MoS_2 , MoSe_2 , MoTe_2 , WSe_2 . Elle est interprétée comme la conséquence de processus Auger inter-bandes résonants très efficaces. Ces études détaillées nous aident à mieux comprendre la physique des semi-conducteurs 2D à base de TMD et ouvrent la voie à de futures applications photoniques et optoélectroniques.

Introduction



2D materials from insulator to superconductor. E_g denotes the band gap. (Ref. [1]).

Nowadays, silicon is still the dominating material in integrated electronic devices. In order to improve the computing power, transistors need to be highly integrated on a chip, which means the size of transistors need to shrink accordingly. The miniaturization of the transistors also helps to reduce power dissipation, increase the processor base frequency and industrial production yield. However, even though the miniaturization techniques are more and more advanced, the performance might not increase as expected due to the problems of gate leakage, carrier scattering and quantum tunneling when the drain and source come too close to each other. Currently, the hard physical scaling limit of Si-electronics is 5 nm (~ 14 silicon atoms) and this induces a deviation from the well known Moore's law, *i.e.* doubling the transistor density roughly every two years.

An alternative could be quantum computing. Quantum computer uses quantum bits (qubits) [2] in contrast to the classical binary bit of 0 and 1. Quantum computer could ideally process the entire superposition of the qubits in parallel, which means exponentially less computing time and energy consumption. Despite recent advances, large-scale quantum circuits are still far from applications because it is composed of a very limited number of qubits and fundamental problems related to quantum decoherence persist.

To improve the performance of digital electronics, a plausible plan could be replacing

silicon with other semiconductors. Industry has tried to use the III-V semiconductors that have larger bandgap and higher carrier mobility, but the application is limited by the cost of high quality wafers. The second choice could be the integration on chips of the two-dimensional (2D) materials made of single or multiple atomically thin layers.

The last decade has witnessed the thriving development of 2D physics, following the groundbreaking work of 2010 Nobel laureates Andre Geim and Konstantin Novoselov regarding graphene. Graphene is the first 2D material found to be thermodynamically stable in ambient condition. Experimentally, the “production” of graphene could be rather simple, using micromechanical exfoliation methods to break the interlayer van der Waals force. This extended single layer of carbon honeycomb has very amazing properties such as high carrier mobility up to the order of $10^5 \text{ cm}^2/V\cdot\text{s}$ at room temperature [3], record material intrinsic strength [4] and the best thermal conductivity among carbon materials [5]. However, graphene is a semi-metal with a gapless band structure of Dirac cone, yielding low on-off transistor ratio $\sim 10^2$ at RT, severely hampering its application. Besides, the massive production of high quality graphene layers is still a challenge.

Nevertheless, the discovery of graphene has boosted the search of other 2D materials such as insulators, semiconductors, metal, superconductors and ferromagnets with very rich electronic properties, see the above figure. These geometry-confined quantum system could provide us with a platform to design and fabricate new generation of electronic devices that exploit quantum effects. The fundamental researches on these materials could also yield applications in quantum communication, quantum sensing and optoelectronics.

In this thesis, we have investigated the electronic and optical properties of 2D materials based on the semiconducting Transition Metal Dichalcogenides. Their general properties will be introduced in Chapter 1: crystal symmetry, band structure, exciton states and spin/valley polarization. In Chapter 2, we will present the main experimental techniques we have performed for the sample fabrication (exfoliation, all-dry visco-elastic stamping technique) and for the measurement of the optoelectronic properties (micro-photoluminescence, differential reflectivity, photoluminescence excitation and time resolved photoluminescence). In Chapter 3, we investigated exciton fine structure in MoS_2 and MoSe_2 MLs on the basis of magneto-photoluminescence spectroscopy up to 30 T. After many years of debates, we find that the spin-forbidden dark excitons lie 14 meV below the bright excitons in MoS_2 ML, whereas it is 1.4 meV above the bright ones in MoSe_2 ML. In Chapter 4, thanks to the very high quality of hBN encapsulated MoSe_2 ML, we demonstrate the control of the exciton radiative lifetime, by simply tuning the hBN bottom layer thickness. A modulation of the lifetime by a factor 10 is evidenced through this Purcell type effect. In the final Chapter 5, we present a detailed investigation of the exciton excited state spectra in several TMD MLs. The key role played by strong exciton upconversion effects is discussed.

Chapter 1

Transition Metal Dichalcogenides

In this Chapter, we introduce the basic properties of Transition Metal Dichalcogenides (TMD). These properties are controlled by their unique band structure: bulk and multi-layer TMDs are indirect gap semiconductors, while monolayers have a direct gap in K valleys, *i.e.* at the edge of the 2D hexagonal Brillouin Zone. Due to the quantum confinement and reduced dielectric screening in 2D, the optical properties of TMD MLs are governed by Coulomb bound electron-hole pair, *i.e.* exciton with binding energy up to hundreds of meV. In addition, due to the broken crystal inversion symmetry and strong spin-orbit coupling, the excitons in TMD MLs have chiral optical selection rules. We review in this Chapter the crystal symmetry and the band structure of TMDs. The key characteristics of exciton states are introduced. Then we present the spin/valley polarization properties. Finally, the geometries of recently developed van der Waals heterostructures and devices are introduced.

The chapter is organized according to the following sections:

- 1.1. Crystal symmetry and band structure
- 1.2. Exciton states
- 1.3. Spin/Valley polarization
- 1.4. Van der Waals heterostructure

1.1 Crystal symmetry and band structure

Transition Metal Dichalcogenides (TMD) investigated in this thesis belong to the MX_2 family ($M = \text{W}, \text{Mo}$; $X = \text{S}, \text{Se}, \text{Te}$). Figure 1.1.1(b) shows several crystal structures of TMD materials: 1T, 2H and 3R. The transition metal atoms are sandwiched by two layers of chalcogen atoms to form a single layer of lattice. Here, we focus on the 2H-phase TMD materials of MoS_2 , MoSe_2 , WS_2 , WSe_2 and MoTe_2 . The bulk material belongs to D_{6h} point group symmetry. Ultrathin layers are easy to exfoliate due to the weak interlayer van der Waals coupling like in the graphite. Figure 1.1.1(a) shows an isolated 2H-phase monolayer and its view normal to the plane. It has armchair and zigzag type edges like graphene. 2H-phase TMD bulk has inversion symmetry that is broken in odd number layers such as monolayer, trilayer... 2H-phase TMD ML belongs to the D_{3h} point group with a honeycomb lattice. Figure 1.1.1(c) shows the hexagonal 1st Brillouin Zone (BZ) of the monolayer. The time-reversal K_{+1} and K_{-1} points are located at the edge of the hexagonal BZ.

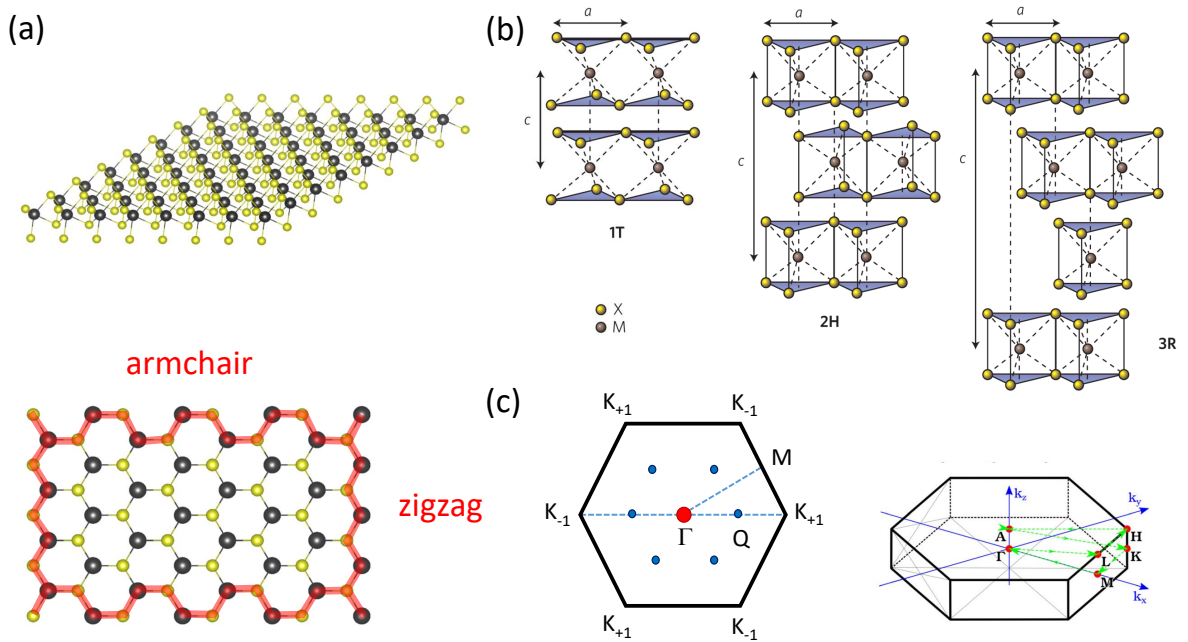


Figure 1.1.1: Crystal structures of Transition Metal Dichalcogenides. (a) A TMD ML, MX_2 ($M = \text{Mo}, \text{W}$, $X = \text{S}, \text{Se}, \text{Te}$). The black and yellow spheres represent transition metal and chalcogen atoms, respectively. The top view shows the hexagonal lattice with armchair and zigzag edges, similar to graphene. (b) Sketch of the structural polytypes: 1T (tetragonal symmetry, octahedral coordination), 2H (hexagonal symmetry, trigonal prismatic coordination) and 3R (rhombohedral symmetry, trigonal prismatic coordination). The interlayer spacing is $c \sim 6.5 \text{ \AA}$. (c) Sketch of the hexagonal 1st Brillouin Zone of the 2H structure. Figures (b,c) are extracted from Refs. [6, 7].

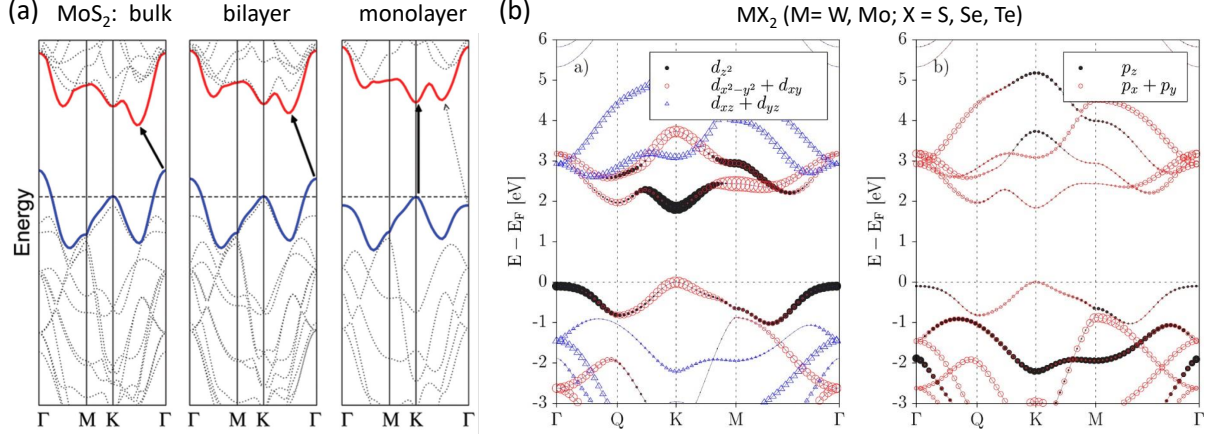


Figure 1.1.2: Density Functional Theory calculations (a) Band structure of MoS₂, extracted from Ref. [8]. (b) Contribution of individual atomic orbitals in MX₂ ML, extracted from Ref. [9]. Transition Metal: d_{z^2} , $d_{x^2-y^2} + d_{xy}$, $d_{xz} + d_{yz}$ and chalcogen atoms: p_z , $p_x + p_y$. Symbol size is proportional to the weight of atomic orbital. (a,b) neglect spin-orbit coupling.

Figure 1.1.2(a) shows the band structure of MoS₂ calculated by Density Functional Theory (DFT) [8]. For the multilayers and bulk, MoS₂ has an indirect band structure with valence band maximum (VBM) at Γ and conduction band minimum (CBM) at the Q symmetry point [roughly the middle between K and Γ , see Figure 1.1.1(c)]. As the thickness decreases, this indirect bandgap (CBM: Q - VBM: Γ) gradually increases and finally the monolayer form has a direct bandgap with CBM and VBM both located at K points (K valleys). In fact, the direct gap (CBM: K - VBM: K) is not very sensitive to the layer thickness.

These changes as a function of the number of layers can be explained by checking the band hybridization. Figure 1.1.2(b) shows the atomic orbital weight in TMD ML. More than one type of orbitals contribute to CB and VB. The weight of each contribution changes throughout the BZ. We notice that the CB wavefunction in K and Q, as well as the VB wavefunction in K and Γ are built mainly from the d-orbitals (d_{z^2} , $d_{x^2-y^2} + d_{xy}$, $d_{xz} + d_{yz}$) of the transition metal. The transition metal atoms are sandwiched between these Chalcogen atoms, so that the d-orbitals are not very sensitive to the altered layer coupling due to thickness reduction. The upshifts of indirect bandgap (CBM: Q - VBM: Γ) is mainly due to the Chalcogen p_z -orbital that is more influenced by the interlayer van der Waals interaction. This indirect to direct band structure crossover applies to the main five TMD materials of MoS₂, MoSe₂, WS₂, WSe₂ and MoTe₂.

Experimentally, Angle-Resolved Photoemission Spectroscopy (ARPES) measures directly the distribution of electrons in momentum-space, so that it can reveal the band structure below the Fermi level [10–14]. Figure 1.1.3 shows ARPES measurements of MBE-grown MoSe₂ thin layers, extracted from Ref. [10]. In both undoped and potassium-doped n-type MoSe₂ MLs, the VBM is measured at K point. The CBM at K can only be measured in potassium-doped MoSe₂ ML, confirming a direct bandgap (CBM: K - VBM: K) in MoSe₂ ML. We also notice that the VBM switches from K to Γ in thicker layers, qualitatively consistent with general DFT calculations.

The Scanning Tunneling Microscope (STM) technique also measures directly the bandgap by recording the current associate to the quantum tunneling between sample

and the probing tip. Thus, the sample has to be conductive, or a conducting substrate must be used. Figure 1.1.4 shows the measured direct bandgap $E_g = 2.18 \pm 0.04$ eV of MoSe₂ ML exfoliated on bilayer graphene (BLG) [15].

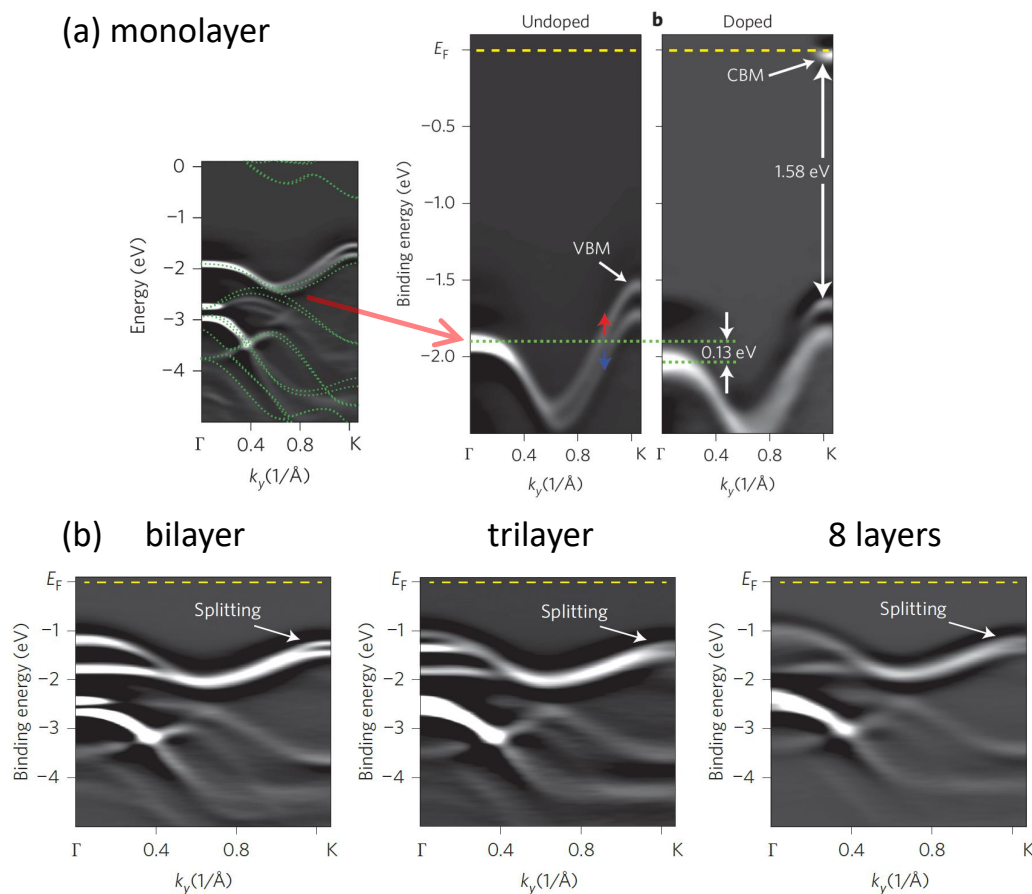


Figure 1.1.3: ARPES spectra of MoSe₂ thin layers grown by MBE on epitaxial graphene terminated SiC substrate, extracted from Ref [10] (a) data of undoped and potassium-doped MoSe₂ ML. (b) VBs in undoped bilayer, trilayer and 8 layers.

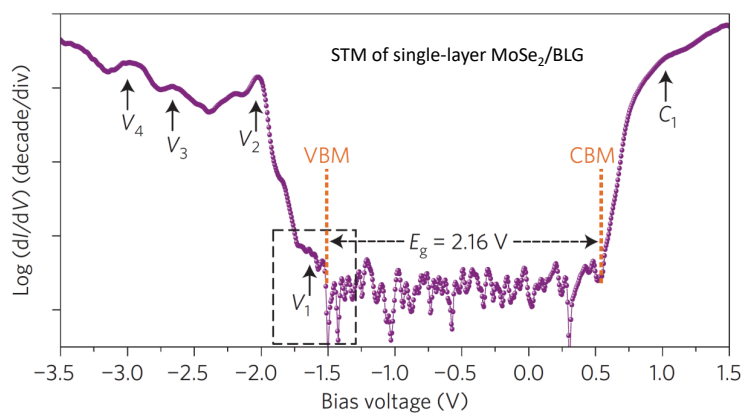


Figure 1.1.4: STM spectroscopy of a MoSe₂ ML on bilayer graphene (BLG), extracted from [15]. The measured voltage of 2.16 V corresponds to a calculated bandgap $E_g = 2.18 \pm 0.04$ eV.

1.2 Exciton states

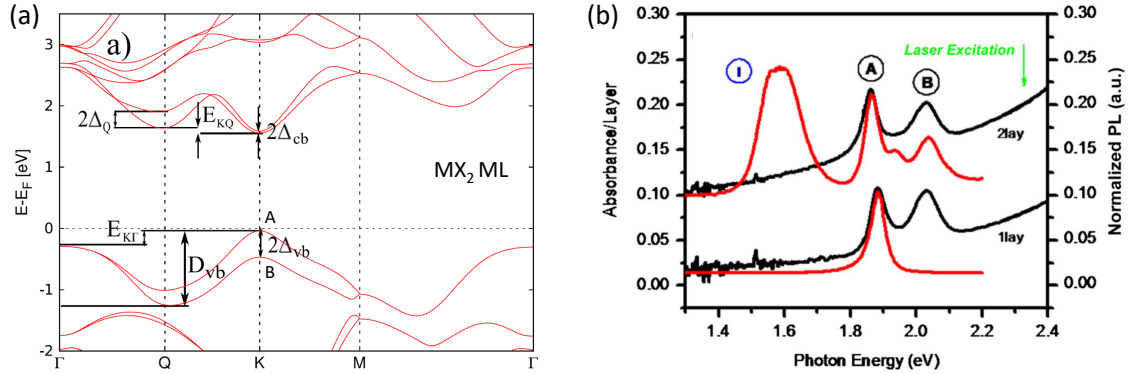


Figure 1.2.1: (a) DFT calculated band dispersion of MX_2 ML along the Γ -K-M- Γ line in the Brillouin zone, with SOC taken into account, extracted from [9]. The labels A and B marks the VB subbands split by SOC. (b) Absorbance and normalized PL of suspended MoS_2 ML and BL at room temperature (RT), extracted from [16].

As shown in the ARPES measurements, the actual band structure has to take into account the SOC. Figure 1.2.1(a) shows a DFT calculated band structure of TMD ML with spin-orbit coupling (SOC) [9]. Due to the broken inversion symmetry, all bands are split by intrinsic SOC, except the time-reversal invariant points M and Γ , qualitatively consistent with the ARPES measurements in Figure 1.1.3(a).

Optical measurements are also powerful means to reveal the band structure. As a direct bandgap semiconductor, TMD MLs are expected to exhibit larger photoluminescence (PL) intensity than its indirect counterparts (bilayers, trilayers...bulk). This was indeed firstly observed by Mak *et al.* for suspended MoS_2 [16]: the monolayer has absorption up to 20% and its PL quantum yield is two orders of magnitude larger than that of bilayer. Figure 1.2.1(b) compares the absorbance and normalized PL of suspended MoS_2 ML and BL [16]. The absorbance spectra show two peaks labeled A and B coming from the transitions between SOC subbands of CB and VB in K valleys. For this direct transition, the absorbance is almost insensitive to the layer number, confirming the almost invariant K valley transitions to the interlayer coupling. The PL spectrum matches well with the absorbance for the A transition. In addition, MoS_2 BL has an additional PL peak (labeled I) for the indirect bandgap.

In TMD MLs, the band edge A-transition is significantly smaller in energy than the measured single particle electronic bandgap [15, 17–19]. The optical properties of TMD MLs are actually governed by tightly bound electron-hole pair, *i.e.* exciton, with binding energy (E_B) on the order of $0.3 \sim 0.5$ eV. This huge binding energy is 1 or 2 orders of magnitude larger than traditional quasi-2D systems based on III-V or II-IV semiconductor quantum wells, so that we can observe PL due to exciton recombination even at RT (thermal energy ~ 26 meV at 300 K). Such robust excitonic effect is a mixed result of perfect 2D quantum confinement and reduced dielectric screening at 2D [20, 21]. As explained below, the dielectric environment (such as surface adsorbates, substrate, encapsulation layers...) plays a key role on the TMD exciton properties. These dielectric environment causes additional screening, which can change the exciton binding energy and free carrier bandgap up to hundreds of meV [15, 22–25].

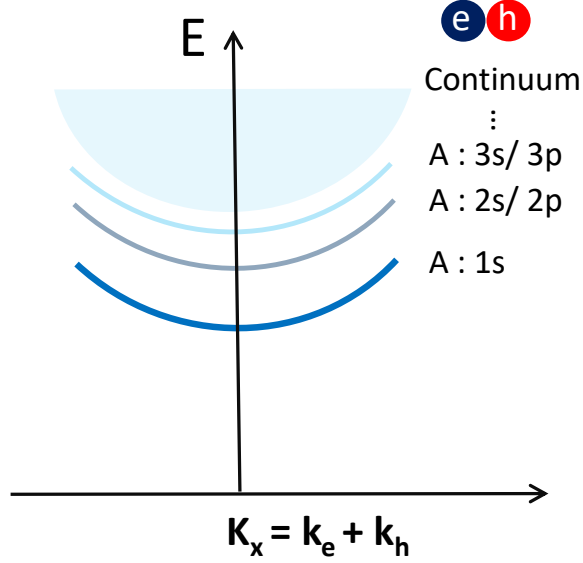


Figure 1.2.2: Sketch of the A-exciton series in the quasi-particle picture. Continuum stands for the onset of quasi-particle (free carrier) bandgap, *i.e.* unbound electron and hole state.

Let us recall that there are two basic types of excitons: Frenkel exciton and Wannier-Mott exciton. Frenkel exciton has a much smaller radius comparable to the unit cell [26]. While the exciton radius in TMD MLs is small ($a_B \simeq 1$ nm) in real space, one can still consider a Wannier-Mott regime, since the correlation of electron and hole extends across several lattices and the excitons are free to propagate in-plane [27]. Thus, we can model the excitons in TMD MLs as a hydrogen-like structure. The exciton wavefunction [28,29] in momentum-space is thus expressed as

$$\Psi^X = \sum_{e,h} C^X(k_e, k_h) |e; h\rangle \quad (1.1)$$

where $|e\rangle$ and $|h\rangle$ are electron and hole Bloch wavefunctions; and $C^X(k_e, k_h)$ represents the relative contribution of (k_e, k_h) electron-hole pairs in the exciton. Small exciton radius (a_B) means the exciton wavefunction spread in the reciprocal space is quite large in BZ and states far away from the K points need to be considered [9]. Calculations based on Density Functional Theory (DFT) coupled to Bethe Salpeter Equation (BSE) have been carried out to predict the exciton spectra taking into account the details of the TMD band structure [15, 30, 31].

In analogy to the hydrogen Rydberg series, the exciton states are named accordingly with principal quantum number ($n = 1, 2, 3\dots$) and orbital labels ($s, p, d\dots$). Figure 1.2.2 presents the schematic dispersion curves of the A-exciton series: A: ns , in which A:1s corresponds to the A-exciton ground state that can be evidenced in PL and absorbance as shown in Figure 1.2.1(b).

Experimentally, the excited exciton states ($n > 1$) can be probed by optical measurements such as (single or two-photon) absorption and photoluminescence-excitation microscopy (PLE) [31, 32], differential reflectivity [20] and second harmonic generation (SHG) [31, 33], etc. Figure 1.2.3 sketches a typical optical absorption spectrum. The absorption of excitonic resonances decreases with the increasing exciton principal quantum

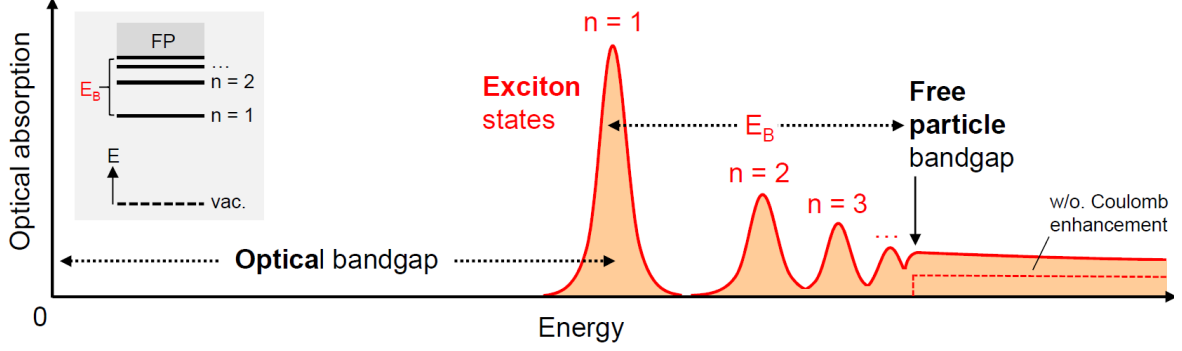


Figure 1.2.3: Schematic illustration of optical absorption of exciton resonances in an ideal 2D semiconductor. Free particle bandgap is shown. Figure extracted from [28]

number n , representing gradual weakening of the light-matter interaction. The oscillator strength of an exciton state for an ideal 2D system is expressed as $f_n = \frac{f_1}{(2n-1)^3}$, where f_1 is the oscillator strength of the ground state, A:1s. The oscillator strength ratio between exciton states and A:1s state is $\frac{1}{27} : \frac{1}{125} : \frac{1}{343}$ for $n = 2, 3$ and 4 , respectively.

Thus, the first challenge for the optical measurements is to detect exciton states with quite small f_n ($n > 1$). After taking the first derivative of the reflectance contrast measurements (differential reflectivity), Chernikov *et al.* reported exciton states up to $n = 5$ in a WS₂ ML [20]. In addition, Robert *et al.* have shown that the oscillators of exciton states can be made more visible by simply varying the bottom dielectric layer's thickness, as a consequence of a cavity-like effect [34], see details in Section 2.2.2. In the following Chapters, we will present different optical techniques including differential reflectivity, photoluminescence, photoluminescence excitation and upconversion to access the excitonic Rydberg series.

Another challenge is the optical measurement of the free carrier bandgap energy. However, the absorption continuum merges into the exciton series, see Figure 1.2.3. A detailed modelling is usually required to extract its value from the measurement of the energy of the exciton states [34]. Because of the inhomogeneous dielectric environment (substrates, hBN, graphene...), the Coulomb interaction deviates strongly from the conventional hydrogenic central potential $\sim 1/r$ [20, 34, 35]. Instead, the Rytova-Keldysh model has been proved to describe the non-hydrogenic potential and yields excellent quantitative results [20, 34, 36, 37]. The Rytova-Keldysh potential is expressed as:

$$V(r) = -\frac{e^2}{8\epsilon_0 r_0} \left[H_0 \left(\frac{\epsilon_{ext} r}{r_0} \right) - N_0 \left(\frac{\epsilon_{ext} r}{r_0} \right) \right] \quad (1.2)$$

where r is the in-plane electron-hole separation; $r_0 = 2\pi\chi_{2D}$ is the screening radius; χ_{2D} is the 2D polarizability; ϵ_{ext} is the effective dielectric constants of the environment; H_0 and N_0 are the Struve and Neumann functions, respectively. Note that in some references [23, 34, 38] $\rho_0 = \varkappa r_0$ is used to provide a direct link with the monolayer polarizability. Since most of the dielectric surroundings (air, SiO₂, hBN...) have usually smaller dielectric constant than the intrinsic bulk TMD materials, the effective environmental dielectric constant ϵ_{ext} for a TMD ML can be taken as an averaged value on top and bottom sides of the 2D-plane, *i.e.* $\epsilon_{ext} = \frac{1}{2}(\epsilon_{top} + \epsilon_{bottom})$.

1.3 Spin/Valley polarization

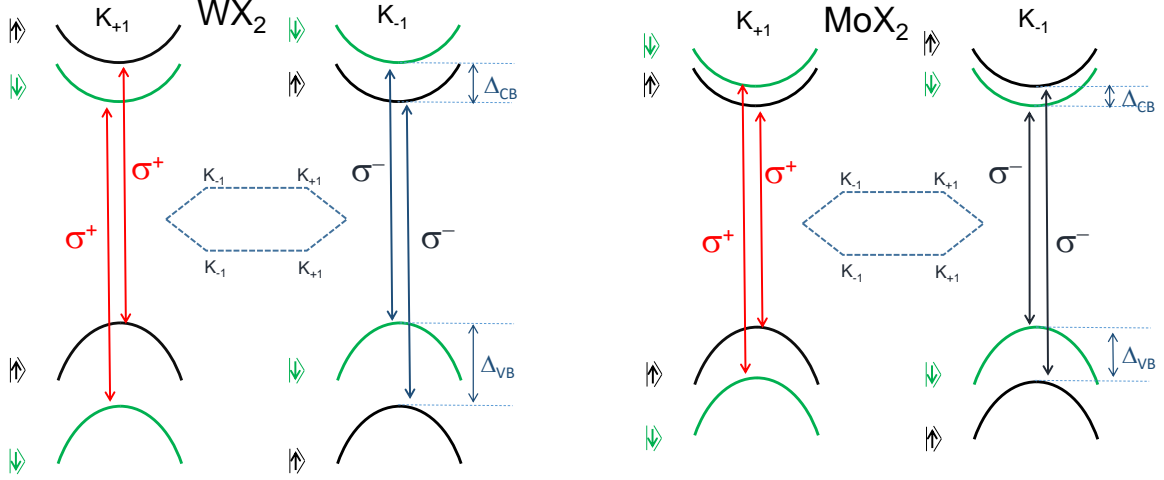


Figure 1.3.1: Schematics of the band structure of WX_2 and MoX_2 MLs around K point in BZ. Spin/valley dependent optical selection rules in K valleys; Δ_{CB} and Δ_{VB} are the spin-orbit splitting in the CB and VB, respectively.

Figure 1.3.1 presents the schematics of the band structure in K valleys of WX_2 and MoX_2 MLs. The spin-orbit splittings Δ_{CB} in CB and Δ_{VB} in the VB are typically of a few hundreds of meV and a few tens of meV, respectively [39–41]. More importantly, depending on the type of transition metal, Δ_{CB} has a different sign, resulting in the bright and dark exciton fine structures, as we will see in Chapter 3.

For a given TMD ML, the K_{+1} and K_{-1} valleys are degenerate in energy, but the sign of both Δ_{CB} and Δ_{VB} are opposite due to the time-reversal symmetry. The label +1 and -1 correspond to the valley index. This yields very unique optical selection rules [29, 40, 42]. By carefully choosing the laser energy and helicity (σ^+ or σ^-), we can selectively excite A and B excitons in K_{+1} or K_{-1} valley, see Figure 1.3.1. Following circularly polarized excitation, the measurement of the PL circular polarization can give information on the spin/valley depolarization mechanisms [42–45]. We will not detail these mechanisms here as we will not present many results on spin/valley polarization properties in this thesis.

1.4 Van der Waals heterostructure

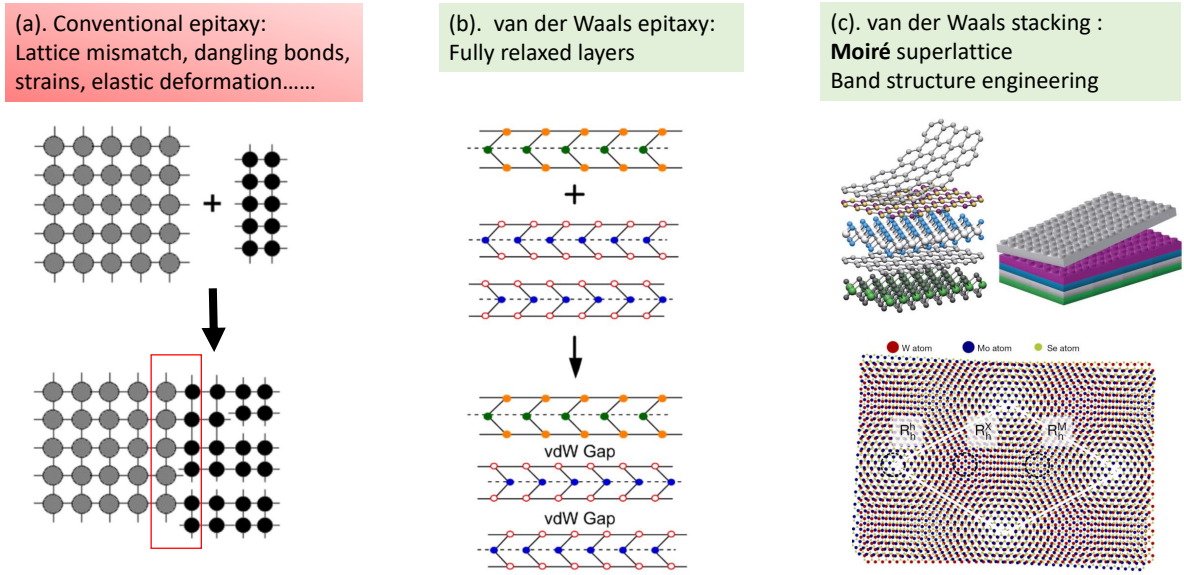


Figure 1.4.1: Heterostructures made in (a) Conventional epitaxy [46]. (b) van der Waals epitaxy [46]. (c) van der Waals stacking [47, 48].

One of the reasons of the interest for 2D materials is the possibility to stack layers of various materials to form van der Waals (vdW) heterostructures [47]. Indeed, while heterostructures made of conventional materials have been used for decades in electronic and optoelectronic devices, their engineering is often limited by the lattice-matching condition to avoid strain relaxation and formation of dislocations, see Figure 1.4.1(a). With vdW crystals, this constraint is relaxed as the layers are separated by the vdW gap. Van der Waals epitaxy [49] has been used recently to produce high-quality TMD structures [50, 51]. It takes advantage of the interlayer van der Waals force instead of the chemical bonds as in conventional molecular-beam epitaxy (MBE), see Figure 1.4.1(b). This technique deposits strain-free epitaxial layers, but is still limited to produce more complex structures for diverse functionalities.

Up to now, the majority of heterostructures are made by van der Waals stacking like building with lego bricks [47], the most developed fabrication technique in the last decade [52, 53]. This considerably extends the choice of materials combinations. Among the emerging vdW heterostructures, we can mention structures made of a semiconducting monolayer and new magnetic 2D layers like CrI_3 [54]. In addition, the twist angle between adjacent layers can be adjusted arbitrarily and offer a new degree of freedom to engineer the electronic band structure. In particular, the stacking of two atomically thin layers with a small lattice mismatch and a small twist angle results in nanoscale periodic variations of the atomic arrangement: the so-called Moiré pattern, see Figure 1.4.1(c). Many novel quantum effects have been observed in such structures such as superconducting and orbital ferromagnetic effects in twisted BLG [55, 56] or localized Moiré excitons in TMD heterobilayers [48, 57, 58]. VdW heterostructures thus offer a unique possibility to control electronic, optical and spin properties at the nanoscale. Nevertheless, a prerequisite to the study of complex vdW heterostructures is to understand the intrinsic properties of individual layers. We will show in the next chapters that it can be done by embedding TMD MLs into hexagonal boron nitride (hBN).

Chapter 2

Experimental Techniques

In this Chapter, we introduce the all-dry transfer and fabrication methods of the 2D van der Waals heterostructures. The effects of hBN encapsulation on TMD MLs are also discussed. Then, we present the general experimental techniques used extensively in the following chapters to measure the excitonic transitions in TMD MLs. The differential reflectivity (DR/R), photoluminescence (PL), photoluminescence excitation (PLE) and time-resolved photoluminescence (TRPL) experiments are described. These experiments are based on a confocal microscopy setup. Polarization measurements can also be achieved on this confocal setup to explore the spin/valley polarization and coherence.

The chapter is organized according to the following sections:

2.1. Sample fabrication

2.1.1. All-dry viscoelastic stamping method and fabrication setups

2.1.2. Identification of TMD monolayer and measurement of hBN thickness

2.2. Optical spectroscopy experiments

2.2.1. Confocal microscopy setups

2.2.2. Differential Reflectivity

2.2.2.1 Modeling of the absorption/reflectivity spectra

2.2.2.2 Fabry-Perot effect and transfer Matrix method

2.2.3. Photoluminescence

2.2.3.1 Continuous wave photoluminescence

2.2.3.2 Photoluminescence excitation

2.2.3.3 Time-resolved photoluminescence

2.3. Effects of hBN encapsulation on optical and exciton properties

2.4. Conclusion

2.1 Sample fabrication

2.1.1 All-dry viscoelastic stamping method and fabrication setups

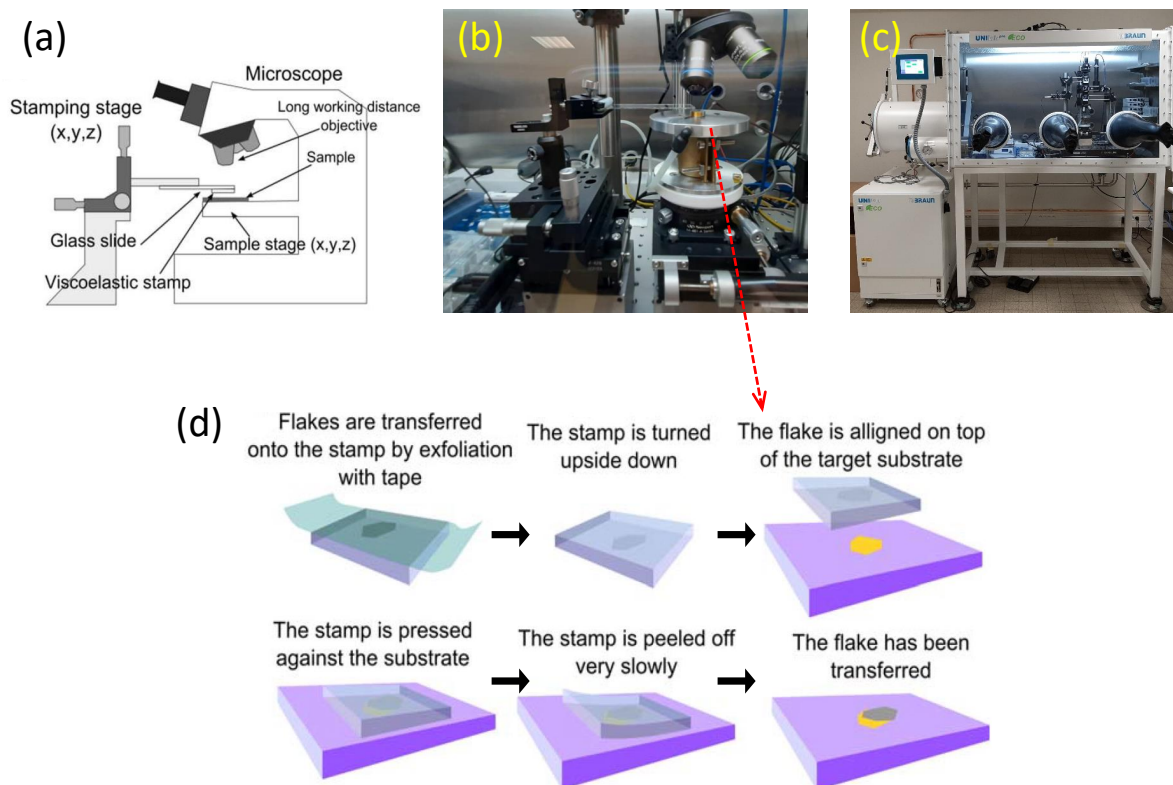


Figure 2.1.1: Fabrication setup and procedures. (a) Sketch of fabrication setup with two (x, y, z) stages extracted from Ref. [59]. The left stage controls the position of glass slide and the PDMS stamp, on which 2D materials are exfoliated. The right stage controls the position of the substrate. (b) Photo of the home-built setup. Each stage has 3 motorized actuators. (c) Glovebox with fabrication setup, hot plate and optical paths inside. (d) Fabrication procedures extracted from Ref. [59].

All-dry viscoelastic stamping method

The 2D van der Waals heterostructure are made by all-dry viscoelastic stamping method. The procedure is shown in Figure.2.1.1(d). We firstly use a piece of scotch tape to mechanically exfoliate 2D materials from the bulk and transfer it on a Polydimethylsiloxane (PDMS) thin film (GelPack[®]; retention level $\times 4$) that is already stucked on the glass slide. Commercial PDMS films are soft, thin and transparent. We can then mount the glass slide upside down and use a long-working distance objective to look for the desired flakes. We use this PDMS thin film to perform *in-situ* stamping on the substrate where other flakes might have already been transferred. Then, we gently bring the PDMS stamp that carries 2D layers into contact with the substrate. Once the flakes are on the target location, we disengage very slowly to remove the PDMS stamp but leave the flakes. By repeating these procedures, we are able to fabricate very complex van der Waals heterostructures.

After each transfer process, we anneal the sample on a hot plate at 200°C for at least

30 minutes. Annealing is of great importance for the interfacial cleanness of the 2D van der Waals heterostructures. At high temperature, the contamination and bubbles trapped between flakes tend to agglomerate due to the self-cleaning mechanism [60].

Fabrication setup

Figure 2.1.1(a) shows a sketch of the transferring setup consisted of mainly two stages. The left stage controls the position of the stamping, whereas the right stage holds a substrate (SiO_2/Si for instance) ready for the deposition processes. Each stage is controlled by 3 manual positioners whose precision is quite dependent on users. Figure 2.1.1(b,c) show our second updated two-stage setup in the glovebox filled with N_2 . The concentration of O_2 and H_2O is controlled under 0.1 ppm, permitting us to work with air-sensitive materials. The typical 6 manual positioners are replaced by 6 motorized actuators from Newport[®] (Models: TRB25CC and LTA-HL with 0.1 μm and 0.05 μm precision, respectively). Additional elements mounted on each stage allow subtle angle rotational manipulations. The substrate on the right stage is fixed by the vacuum created beneath through a tube connected with an outside pump. Additionally, the temperature of the right stage can be controlled from RT to 200°C [61]. The fabrication processes are monitored by an optical microscopy using an objective (Olympus Model. MPLFLN $\times 10$ with a working distance of 11 mm).

2.1.2 Identification of TMD monolayer and measurement of hBN thickness

We have various bulk material sources. TMD bulk grown by Chemical Vapor Transport (CVT) are purchased from companies 2D Semiconductors[®] and hq^+ graphene[®]. Hexagonal Boron Nitride (hBN) crystals are provided by our collaborators Kenji Watanabe and Takashi Taniguchi from NIMS in Japan [62]. We have also used recently hBN crystals grown by Catherine Journet-Gautier and Bérangère Toury-Pierre from Claude Bernard University of Lyon France, using a polymer route combined with a sintering process [63]. If not specified, we have used the “NIMS” hBN throughout this thesis.

The optical contrast of few-layer TMD exfoliated on SiO_2/Si substrate is subjected to interference effects induced by the SiO_2/Si interface [64]. As a result, the typical SiO_2/Si substrates used for TMD MLs always have a SiO_2 thickness around 90 nm or 290 nm to maximize the optical contrast. Our dry-stamping fabrication technique requires us to find TMD MLs on PDMS. Surprisingly, the optical contrast of a 6.5 Å thick TMD ML on PDMS is not low due to the strong light-matter interaction induced by robust excitons. Figures 2.1.2(a,b) present a MoSe_2 ML on PDMS stamp and then transferred on a large bottom hBN. The optical contrast of a TMD ML on PDMS looks like a cicada wing, while TMD bulk with smaller indirect bandgap has a gold color under white light.

hBN is a semiconductor with indirect bandgap ~ 6 eV [65]. Depending on the thickness, hBN layers’ white light reflection have different colors as a result of interference effect. Figures 2.1.2(c,d) show bright and dark field images of MoSe_2 ML and bulk deposited on a hBN flake with many terraces. The interlayer contamination and bubbles are clearly seen in dark field. Figure 2.1.2(e) is the zoom-in of the hBN encapsulated MoSe_2 ML in (c). The top hBN used in our experiments is typically below 10 nm. Thin hBN (< 5 nm) is basically transparent. The optical contrast of hBN monolayer on a SiO_2 (90 nm)/Si substrate is only $\sim 2.5\%$ in white light and $\sim 3\%$ with a green filter [66]. Figures 2.1.2(f,g) are AFM measurements of the hBN terraces labeled “A-F” in (e).

Figure 2.1.2(h) presents the simulated color code of hBN on 80 nm SiO₂ using a transfer matrix method. The results are consistent with the measured hBN colors, as well as the thickness measured by AFM, see Figure 2.1.2(e,f,g).

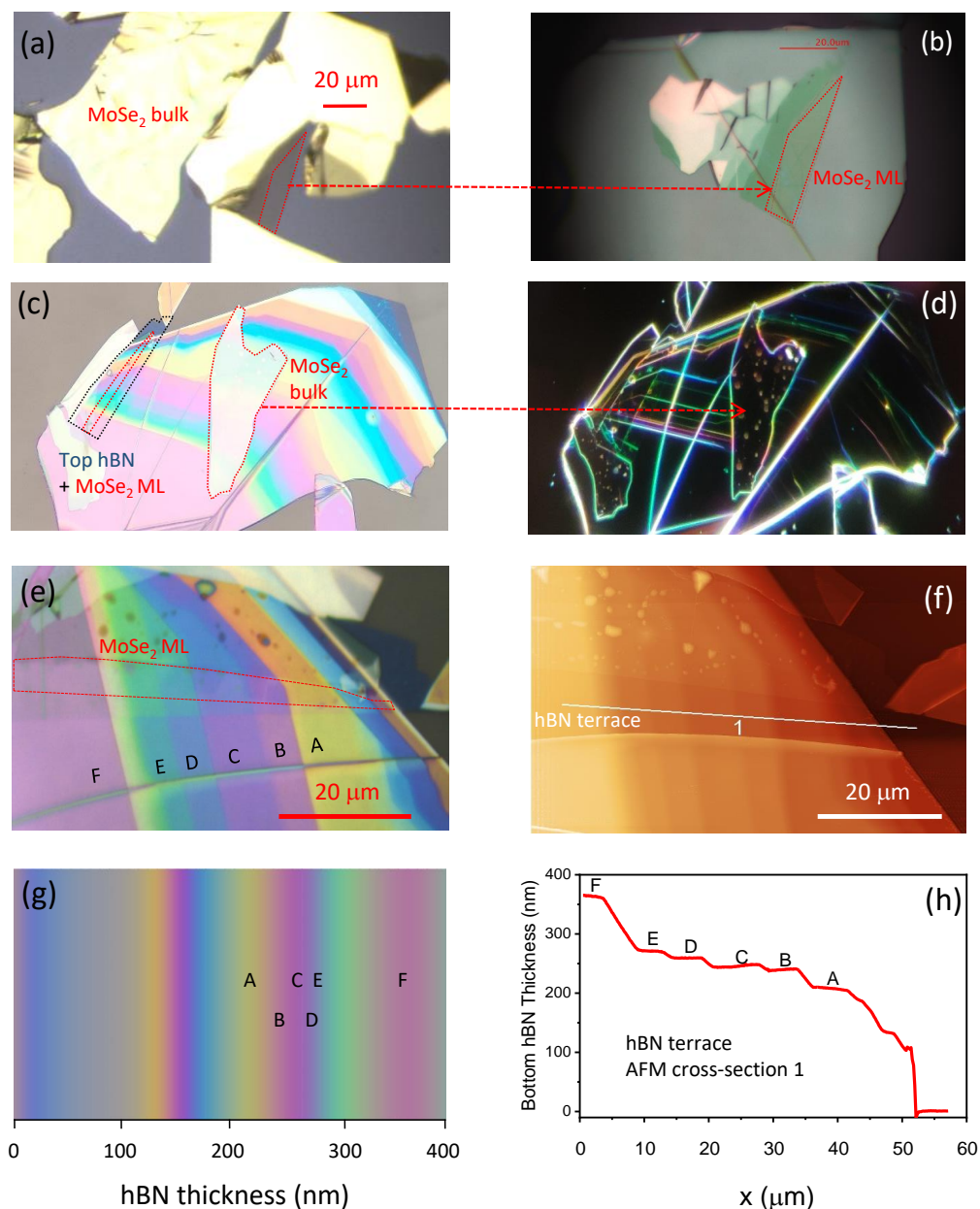


Figure 2.1.2: Optical contrast of MoSe₂ and hBN. (a) MoSe₂ ML and bulk exfoliated on PDMS and (b) transferred on a bottom hBN flake. (c) Bright field image of MoSe₂ ML and bulk transferred on a large hBN with terraces. Red and blue dashed lines represent MoSe₂ and the capping hBN, respectively. (d) Dark field image of (c). The bright features between flakes represent interlayer contamination and bubbles. (e) Zoom-in of (c) on the MoSe₂ ML and its 6 bottom hBN terraces labeled “A-F” . (f) Atomic Force Microscopy (AFM) of (e). Interlayer contamination and bubbles are seen clearly. (g) White light reflectivity: simulation of hBN color on SiO₂ (80 nm)/Si with the transfer matrix method, consistent with the measured terrace thicknesses by AFM in (h) and color in (e). (h) AFM cross-section of the linecut labeled “1” in (f). The terrace thicknesses are A: 206 nm, B: 237 nm, C: 247 nm, D: 262 nm, E: 274nm and F:358 nm.

2.2 Optical spectroscopy experiments

2.2.1 Confocal microscopy setups

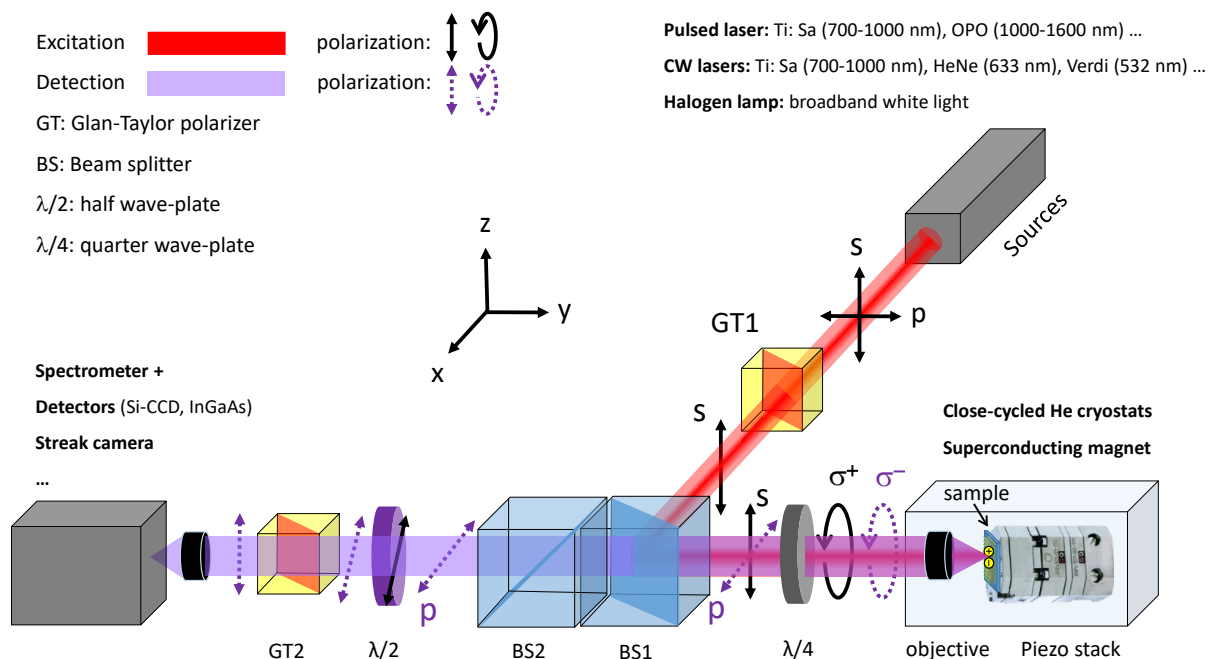


Figure 2.2.1: Confocal microscopy setup.

We have used the confocal optical microscopy setup sketched in Figure 2.2.1 for all the optical spectroscopy experiments. It is consisted mainly of four parts:

Excitation:

We have several commercial laser sources: pulsed and continuous wave (CW) Titanium: Sapphire (Ti: Sa) lasers in the wavelength range of 700 - 1000 nm from Spectra Physics[®] and M-squared[®] (Model: SolsTiS), respectively; 633 nm HeNe laser and 532 nm lasers. An optical parametric oscillator (OPO, Model Mira-OPO) from Coherent[®] and a frequency doubler together with Ti: Sa lasers generate laser light in the near-infrared and blue/UV range, respectively. A tungsten-halogen white-light source allows us to perform the differential reflectivity measurements. An achromatic objective with high numerical aperture (NA=0.82) from Partec[®] is used in the cryostat to achieve a typical focused spot size $\sim 1\mu\text{m}$ for the HeNe laser.

Closed-cycle Helium cryostats:

Low temperature down to 4 K is achieved by several closed-cycle Helium cryostats including attoDRY 700, 1000 and 2000 from Attocube[®] and OptiDry 150 and 250 from Mycryo[®]. The superconducting magnets in the form of single solenoids in attoDRY 1000 (9T) and Mycryo OptiDry 150 (2T) or vector magnets in attoDRY 2000 (5T, 2T, 2T) enable us to perform magneto-optic measurements in various magnetic field geometries. The separated design of the optical table and cold head in these cryostats ensures low mechanical vibrations of the elements (piezo, objective...) mounted on the optical table.

Inside the cryostat, we have used piezo-based cryogenic nanopositioners to control the sample's position. For example, the Attocube[®] ANP z101 z-nanopositioner has a step precision of 10 nm and a total 5 mm travel range in the z-direction. For a full nanopositioning of the three degrees of freedom (x, y, z), two x-nanopositioners can be combined with a z-nanopositioner. The samples are glued with silver paint on a (non-magnetic) metallic sample holder that is then fixed on the piezo stack. Temperature sensors and heaters can be embedded between the sample holder and piezo stack to measure and increase the temperature of the samples, respectively.

Optical paths:

Figure 2.2.1 shows the optical elements mounted on the optical paths for circular polarization measurements. GT1 and GT2 are Glan-Taylor prism polarizers. The laser beam is linearly polarized by GT1 in 's' direction and then reflected by the BS1 (beam splitter 1). The reflection of the BS is polarization dependent. The maximal reflection is $\sim 4\%$ for the polarized component parallel (*i.e.* 's' component) to the interface of BS1, while at least 96% of the light is transmitted. Finally, a quarter waveplate ($\lambda/4$) converts the 's' linearly polarized incidence into σ^+ circularly polarized light that is subsequently focused by the objective on the substrate or sample.

Considering a perfect reflection by the sample that only adds a phase retardation of π , the σ^+ circularly polarized laser is reflected, and converted by the quarter waveplate ($\lambda/4$), back into pure 'p' linearly polarized (perpendicular to the incident 's' component). If the σ^+ circular polarization is somehow depolarized into elliptical or totally unpolarized components, we should have both the 'p' and 's' linear components converted through the quarter waveplate, representing the co and counter circular polarization of the signal, respectively. On the detection side, we use the other BS2 lying 45° to the x-y plane to compensate the polarization loss of the signal by using only BS1. The analyzer, GT2, is fixed to ensure a constant detection efficiency of the diffraction gratings and the detector. Thus, we just need to rotate the half waveplate ($\lambda/2$) before GT2 to select either the co or counter circular component transmitted through the GT2. The angle difference of a half waveplate for the co and counter components is 45° . The half waveplate can be replaced by a Liquid Crystal Retarder (LCR) to minimize the errors caused by manual rotation and imperfections of the waveplate during the manufacture.

For the circular polarization resolved photoluminescence (PL) measurements, the polarization degree is calculated by

$$P = \frac{I_{co} - I_{counter}}{I_{co} + I_{counter}} \quad (2.1)$$

where I_{co} and $I_{counter}$ represent the PL intensity of the co and counter polarized signal.

Detection:

Spectrometers from Princeton Instruments[®] have been used for spectral dispersion. The spectrometers are consisted mainly of diffraction gratings and two concave mirrors in a long optical path geometry. In static optical measurements, silicon charge coupled devices (Si-CCD) and Indium Gallium Arsenide detectors (InGaAs, Model: PyLon-IR) from Princeton Instruments[®] are used to detect the light signal dispersed by the spectrometer. In order to minimize the signal-to-noise ratio, liquid nitrogen is used to cool the Si-CCD and InGaAs detectors. Their quantum efficiencies are wavelength-dependent. Si-CCD has a poor response beyond 1000 nm due to the decreasing absorption coefficient, while the InGaAs detectors have better response over the 1000 nm to 1600 nm wavelength range. We have also streak cameras from Hamamatsu Photonics[®], allowing us to perform time-resolved photoluminescence measurements, see details in Subsection 2.2.3.

As an example, Figure. 2.2.2 presents the intensity of σ^+ and σ^- luminescence components of a hBN encapsulated WSe₂ ML at 4 K detected by a Si-CCD camera, following a σ^+ polarized HeNe laser excitation. In the following sections, we will explain in detail several spectroscopy techniques including differential reflectivity, photoluminescence, photoluminescence excitation and time-resolved photoluminescence measurements that involve the setups we have introduced above.

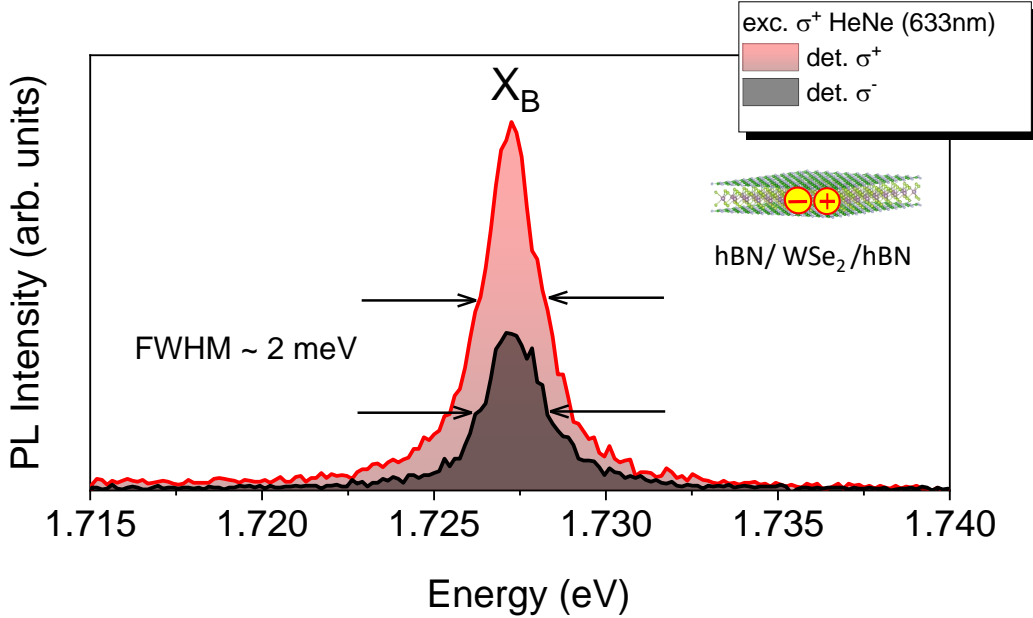


Figure 2.2.2: Exciton spin/valley PL polarization in a WSe₂ ML encapsulated by hBN. σ^+ HeNe laser (633 nm) excitation at a cryogenic temperature of ~ 4 K. The full width at half maximum (FWHM) is ~ 2 meV.

2.2.2 Differential Reflectivity

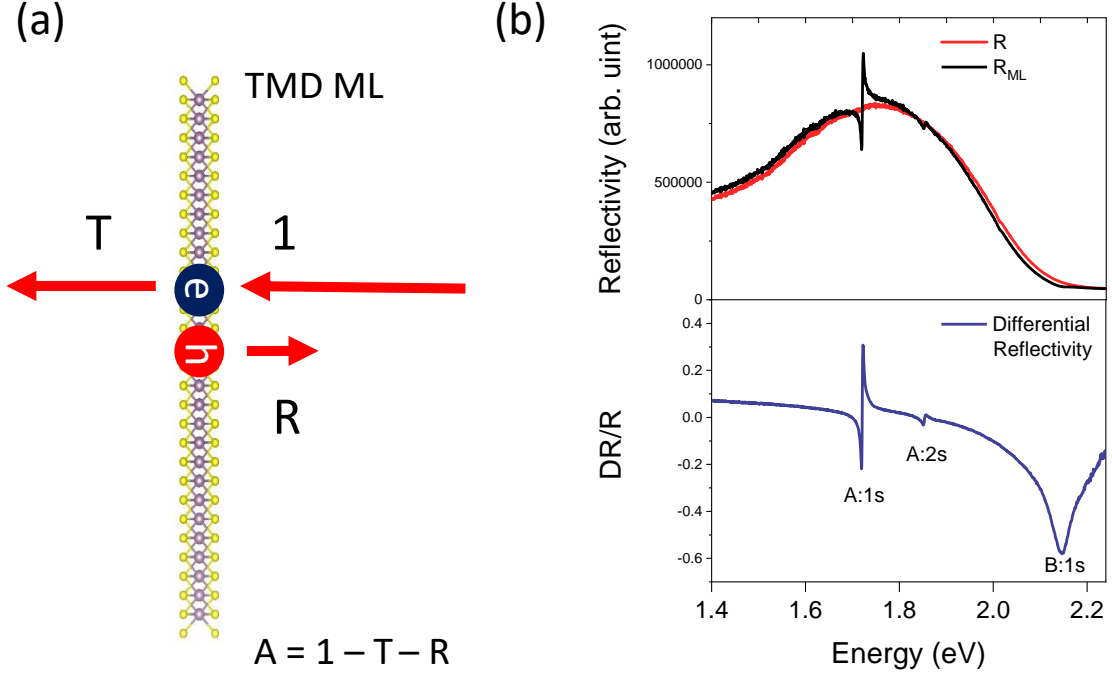


Figure 2.2.3: (a) Intrinsic optical response of a TMD ML in vacuum. Absorption (A), transmission (T) and reflection (R) add up to the incident white light (1). (b) Top panel: raw data of reflectivity of the hBN encapsulated WSe₂ ML (black curve) on a SiO₂(80 nm)/Si wafer and the white light reference on the capping hBN (red curve); down panel: differential reflectivity showing the different excitonic states of A:1s, A:2s and B:1s.

In this thesis, we have used differential reflectivity to probe the exciton states in TMD MLs. The differential reflectivity (DR/R) is defined as

$$\frac{DR}{R} = \frac{R_{ML} - R}{R} \quad (2.2)$$

where R_{ML} and R are reflection coefficients of the sample with and without the TMD ML, respectively. The differential reflectivity in down-panel of Figure 2.2.3(b) clearly evidences higher exciton states of A:2s and B:1s, in addition to the A:1s ground state. In contrast to the raw reflectivity, differential reflectivity has a basically flat background located around zero, making the estimation of the transitions' oscillator strength much easier.

2.2.2.1 Modeling of the absorption/reflectivity spectra

In a classical model, the optical response of a material can be modeled by Lorentz oscillators. We can use this simple oscillator model to describe the absorption of excitonic states in TMD MLs. A light beam impinging on the TMD ML will not only undergo absorption, but transmission and reflection processes have also to be considered, see Figure 2.2.3(a). These optical responses around the j_{th} excitonic resonance at frequency ω_0 is described by the complex refractive index $\tilde{n}(\omega) = n(\omega) + i\kappa(\omega) = \sqrt{\varepsilon(\omega)}$, where $\varepsilon(\omega) = \varepsilon_1(\omega) + i\varepsilon_2(\omega)$ is the material's complex dielectric constant. $\varepsilon(\omega)$ is expressed as [67]:

$$\varepsilon(\omega) = \varepsilon_b + \frac{f_j}{\omega_0^2 - \omega^2 - i\omega\Gamma_j} \quad (2.3a)$$

$$\varepsilon_1(\omega) = \varepsilon_b + \frac{f_j(\omega_0^2 - \omega^2)}{(\omega_0^2 - \omega^2)^2 + \omega^2\Gamma_j^2} \quad (2.3b)$$

$$\varepsilon_2(\omega) = \frac{\omega\Gamma_j f_j}{(\omega_0^2 - \omega^2)^2 + \omega^2\Gamma_j^2} \quad (2.3c)$$

where f_j is the oscillator strength, *i.e.* coupling strength between the external electromagnetic field and the forced oscillation of the j_{th} oscillator; Γ_j is the damping rate of the j_{th} resonance; and ε_b is the background dielectric constant from oscillators other than the j_{th} one. Thus, the absorption of light at the j_{th} excitonic resonance is proportional to f_j . From the 1st order quantum perturbation theory, we have the j_{th} oscillator strength

$$f_j \propto |H_{if}^{(1)}|^2 \quad (2.4)$$

where $|H_{if}^{(1)}|^2 = |\langle f|H^{(1)}|i\rangle|^2$ is transition probability (transition matrix elements squared) between the system initial state $|i\rangle$ and the excitonic state $|f\rangle$, $H^{(1)}$ being the dipole operator.

2.2.2.2 Fabry-Perot effect and transfer matrix method

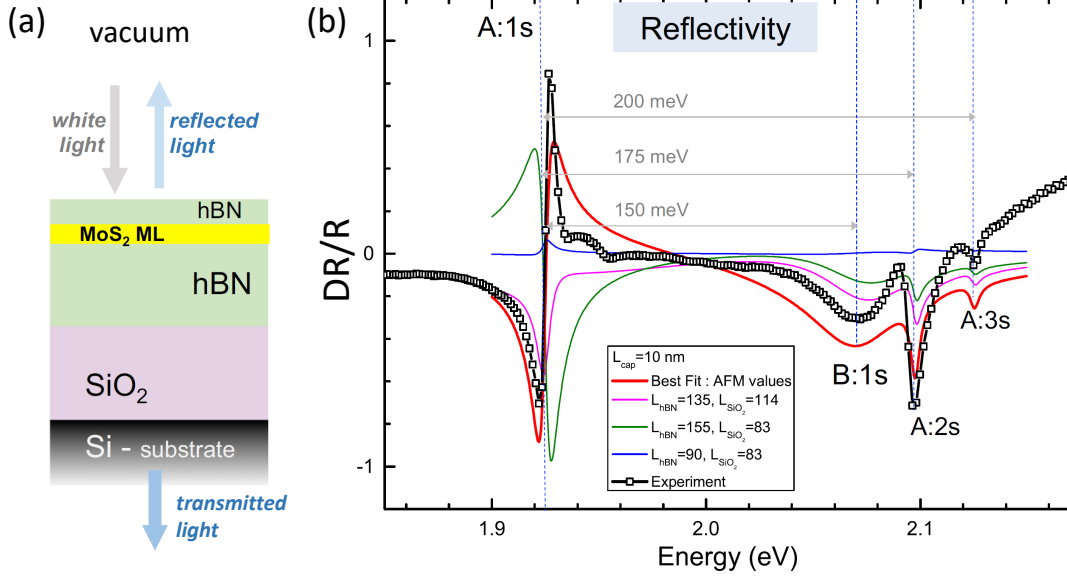


Figure 2.2.4: Fabry-Perot effect in hBN encapsulated MoS₂ ML. (a) Simplified structure used in our analytical model. (b) Differential reflectivity measurement. Red curve is the model simulations using the hBN thicknesses as determined by AFM (squared dots). Additional simulations (fine magenta, green, and blue) show the depth and shape of the exciton resonances depends on the individual layer thickness of hBN and SiO₂. Figures extracted from Ref. [34].

As we will see in next chapters, the properties of TMD MLs are strongly improved if they are encapsulated in hBN. Then, we need to take into account this dielectric environment to understand the excitonic and optical properties. Our collaborators Mikhail Glazov and Marina Semina from IOFFE Institute of Russia developed a transfer matrix method to model and calculate the elementary response functions (reflectivity, transmission and absorbance) of our structure “capping hBN layer/TMD ML/bottom hBN layer/SiO₂/Si” as sketched in Figure. 2.2.4(a). The transfer matrix of the total sample structure is expressed as:

$$\hat{T}_{tot} = \hat{T}_{SiO_2 \rightarrow Si} \hat{T}_{SiO_2} \hat{T}_{hBN \rightarrow SiO_2} \hat{T}'_{hBN} \hat{T}_{ML} \hat{T}_{hBN} \hat{T}_{air \rightarrow hBN}. \quad (2.5)$$

Here $\hat{T}_{i \rightarrow j}$ is the transfer matrix through the interface between the layers i to j , \hat{T}_i is the transfer matrix through the layer i , the prime denotes bottom hBN layer. For TMD ML transfer matrix we consider the situation of a monolayer embedded into infinite hBN:

$$\hat{T}_{ML} = \frac{1}{t} \begin{pmatrix} t^2 - r^2 & r \\ -r & 1 \end{pmatrix}, \quad (2.6)$$

$$r = \frac{i\Gamma_{rad}^{hBN}}{\omega_0 - \omega - i(\Gamma_{rad}^{hBN} + \Gamma_{rad}^{vac})}, \quad t = 1 + r. \quad (2.7)$$

Here r and t are the reflection and transmission coefficients of the TMD ML in the infinite homogeneous hBN, ω_0 is the exciton resonance frequency, Γ_{rad}^{hBN} is the TMD exciton radiative damping rate (radiative decay rate) into the hBN, $\Gamma_{rad}^{hBN} = \Gamma_{rad}^{vac}/n_{hBN}$, where n_{hBN} is the hBN refractive index and Γ_{rad}^{vac} is the radiative decay rate into free

space. Γ_{nrad} is the exciton non-radiative damping rate (non-radiative decay rate). Note that the general decay rates Γ_{rad} and Γ_{nrad} are linked to the radiative and non-radiative linewidths γ_{rad} and γ_{nrad} defined in Section 4.1 by $\gamma_{rad} = 2\hbar\Gamma_{rad}$ and $\gamma_{nrad} = 2\hbar\Gamma_{nrad}$. The Si layer is assumed to be thicker than the absorption length, hence, the reflection of light at the interface Si and air is disregarded. The transfer matrix provides the following relationship between r_{tot} and t_{tot} , the amplitude of reflection and transmission coefficients, through the total structure:

$$\hat{T}_{tot} \begin{pmatrix} 1 \\ r_{tot}(\omega) \end{pmatrix} = \begin{pmatrix} t_{tot}(\omega) \\ 0 \end{pmatrix}. \quad (2.8)$$

Eq. (2.8) allows us to obtain $r_{tot}(\omega)$ and $t_{tot}(\omega)$ from the transfer matrix. Figure 2.2.4(b) shows several optical transitions in the Differential Reflectivity of an hBN encapsulated MoS₂ ML. We ascribe them to A-exciton series (A:1s, 2s and 3s) and B:1s state. By using Eq. (2.8), the quantitative analysis (red curve) of the energies and oscillator strengths of the A-exciton Rydberg series and B:1s are in good consistency with the experimental observations. We also demonstrate that the shape and intensity of the exciton transitions (fine magenta, green, and blue curves) in the differential reflectivity spectrum strongly depend on the thicknesses of the dielectric layers (hBN and SiO₂). This is a result of the interferences in the dielectric layers, *i.e.* Fabry-Perot effect in the microcavity-like sample structure. Therefore, we can choose carefully the bottom hBN and SiO₂ thicknesses to gain more visibility of the excited exciton states.

Following the Transfer Matrix method, we can also have an estimate of the absorption coefficient and the radiative recombination rate. The absorbance of the monolayer can be expressed as

$$\mathcal{A}(\omega) = 1 - |r_{tot}(\omega)|^2 - |t_{tot}(\omega)|^2/n_{Si}, \quad (2.9)$$

where n_{Si} is the refraction index of Si.

According to the general theory [45, 68, 69], the poles of the response functions $r_{tot}(\omega)$, $t_{tot}(\omega)$ and, accordingly, the feature in $\mathcal{A}(\omega)$, correspond to the eigenmodes of the system. In the vicinity of an exciton resonance frequency ω_0^{eff} , the functions $r_{tot}(\omega)$ and $t_{tot}(\omega)$ can be recast in the form

$$r_{tot}(\omega) = \frac{Z_r}{\omega_0^{\text{eff}} - \omega - i(\Gamma_{rad}^{\text{eff}} + \Gamma_{nrad})} + \dots, \quad (2.10a)$$

$$t_{tot}(\omega) = \frac{Z_t}{\omega_0^{\text{eff}} - \omega - i(\Gamma_{rad}^{\text{eff}} + \Gamma_{nrad})} + \dots, \quad (2.10b)$$

where dots denote regular part, Z_r and Z_t are the complex constants, and the quantities ω_0^{eff} and $\Gamma_{rad}^{\text{eff}}$ represent the renormalized exciton frequency and its effective radiative decay rate. Accordingly, the absorbance in the vicinity of the resonance is approximated by

$$\mathcal{A}(\omega) \approx \frac{\mathcal{A}_0}{(\omega_0^{\text{eff}} - \omega)^2 + (\Gamma_{rad}^{\text{eff}} + \Gamma_{nrad})^2}. \quad (2.10c)$$

In summary, Figure 2.2.4 clearly demonstrates that the Fabry-Perot effect in hBN encapsulated TMD MLs has to be carefully modeled in order to understand the exciton spectra probed by differential reflectivity. In Chapter 4 we will show that this Fabry-Perot effect also induces quantum fluctuation around the TMD MLs, which yields a tuning of the exciton dynamics and the radiative linewidth γ_{rad} (Purcell effect).

2.2.3 Photoluminescence

2.2.3.1 Continuous wave photoluminescence

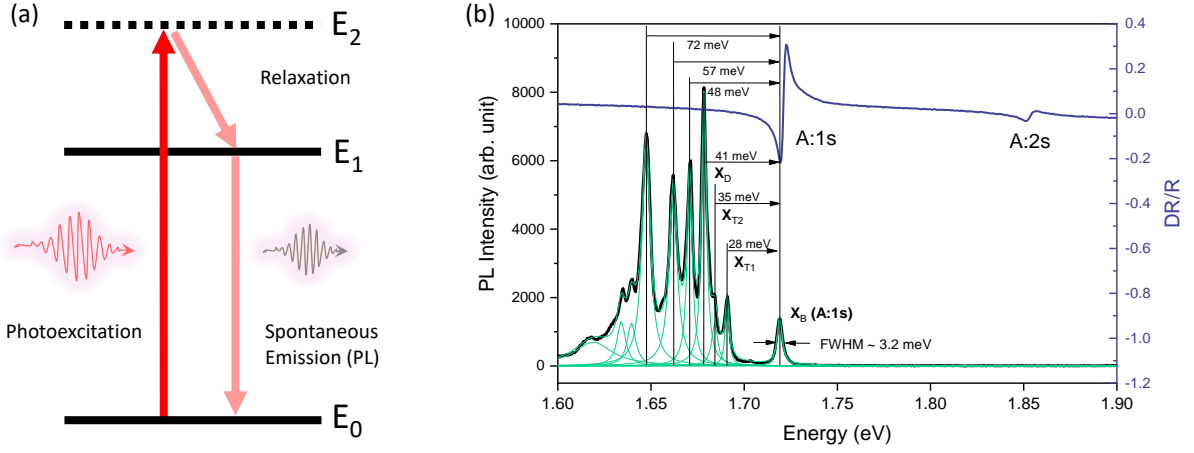


Figure 2.2.5: (a) Schematics of the Photoluminescence (PL) process: photoexcitation, relaxation and spontaneous emission. (b) PL and differential reflectivity spectra measured for the same WSe₂ ML as in Figure 2.2.3(b) at 4 K. The PL of A:1s exciton (X_B , the subscript “B” denotes bright neutral exciton) has a full width at half maximum (FWHM) ~ 3.2 meV. X_{T1} (X_{T2}) and X_D denote PL emissions from trions and dark neutral exciton, respectively.

Figure. 2.2.5(a) shows a simplified schematics of the photoluminescence (PL) process: photogeneration of carriers by laser excitation, relaxation by phonon emission and spontaneous emission. In contrast to absorption and reflectivity that measure directly the excitonic resonances, the PL signal depends on the absorption efficiency at the laser wavelength, efficiency of relaxation channels down to the emitting states and competition between radiative and non-radiative channels.

Figure. 2.2.5(b) shows both the Differential Reflectivity and PL signals of the same hBN encapsulated WSe₂ ML as in Figure 2.2.3(b). The PL is excited with HeNe laser (633 nm; 1.96 eV). The differential reflectivity evidences only two resonances corresponding to A:1s and A:2s exciton states, while the PL shows multiple strong peaks below the A:1s state. These states with much lower oscillator strengths have been identified recently and correspond to recombinations of dark neutral exciton (X_D), trions (X_T , charged excitation), biexcitons, etc [70–73].

2.2.3.2 Photoluminescence excitation

Photoluminescence excitation (PLE) spectroscopy is also a powerful tool to get information on the exciton properties. The excitation wavelength is varied continuously with constant laser excitation power, while the PL intensity at a typical emission is recorded. Peaks in the PLE spectrum represent absorption resonances of the material and their intensity depend on both the effective absorption at the excitation wavelength and also the efficiency of relaxation to the monitored state. Since the absorption is strong when laser wavelengths are tuned exactly at resonances, exciton resonances associated to excited states ($n > 1$) can be easily detected in PLE measurements [31]. Figure 2.2.6 shows a PLE spectrum of MoS₂ ML encapsulated in hBN (same sample as used in Figure 2.2.4). The A:2s and A:3s exciton states are unambiguously measured, in perfect agreement with the differential reflectivity shown in Figure 2.2.4.

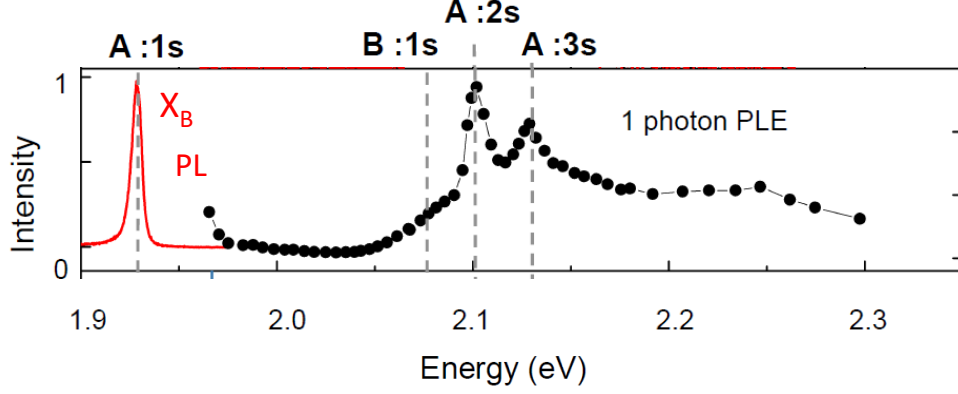


Figure 2.2.6: PLE spectrum of MoS₂ ML encapsulated in hBN (same sample as used in Figure 2.2.4). PL intensity of X_B (A:1s) exciton is recorded while changing the excitation laser energy with constant power. PL spectrum by nm laser excitation is also shown (red curve). Figure is extracted from Ref. [34].

2.2.3.3 Time-resolved photoluminescence

Time-resolved photoluminescence (TRPL) corresponds to the PL measurement in temporal domain by using a pulsed laser and a fast detector. We use a continuous wave 532 nm laser to pump a mode-locked Ti:Sa laser that then generates picosecond (*ps*) pulses in the wavelength range from 700 to 1000 nm, see Figure 2.2.7(a). The pulses are equally spaced in time with a repetition rate of 80 MHz and a pulse width of ~ 1.5 ps.

To detect the PL in temporal domain, we have used a synchro-scan streak camera, which is one of the highest sensitive and fastest detectors that can capture the signal in both spectral and temporal domain, see Figure 2.2.7(b). The principle of a streak camera is shown in Figure 2.2.7(d). The pulse signals being measured are guided through a slit and focused by the optical lens onto the photocathode of the streak tube. The incident light impinging on the photocathode is converted into a number of electrons proportional to the intensity of the light. These electrons are accelerated by the accelerating mesh (electrodes) and pass through a pair of sweep electrodes that is applied with high voltage at a timing synchronized to the Ti:Sa laser pulse, see Figure 2.2.7(e). By high speed sweep, the electrons experience a vertical deflection proportional to the arrival time of the photons on photocathode. Then, the deflected electrons enter the micro-channel plate (MCP) where the signal is multiplied by thousands of times and impact against the phosphor screen where they are converted back into light and finally recorded by a CCD camera.

As a result, an obtained brightness distribution image is arranged as follow: the horizontal direction corresponds to the emission wavelength; the vertical direction serves as the time axis: earlier signal is spatially located at the top of the image, while the photons arriving later yield signal at the bottom of the image. Figure 2.2.7(c) shows a typical streak camera image. For a given emission, it is consisted of a rise part corresponding to the population establishing on this state and a longer decay part corresponding to the population decay by both radiative recombination and non-radiative channels.

The TRPL setup based on the *ps* Ti:Sa laser and the streak camera (with an overall time-resolution of ~ 2.5 ps) is the key tool we have used in Chapter 4 to demonstrate the control of the exciton radiative lifetime τ_{rad} in hBN encapsulated MoSe₂ MLs.

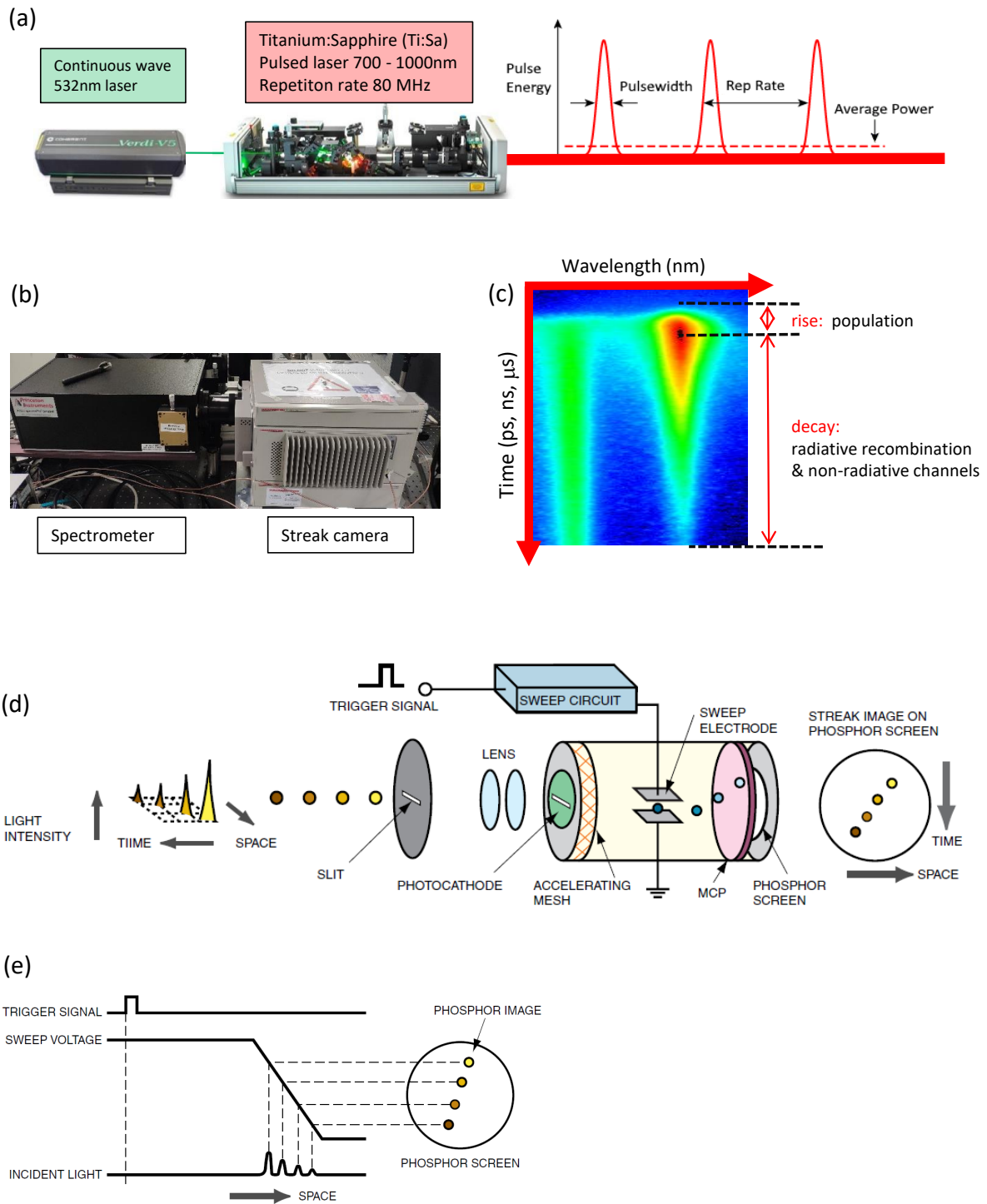


Figure 2.2.7: Setups and mechanisms for time-resolved photoluminescence measurements. (a) Pulsed laser chain: pump (Coherent® Verdi series: Model V5; diode-pumped solid-state continuous wave laser at 532 nm up to 10 W) and mode-locked Ti:Sapphire laser (Spectra Physics® Tsunami series: Model 3960-L3B, 700-1000 nm). (b) Streak camera (Hamamatsu Photonics®: Model S20, 350-800 nm) mounted on a spectrometer (Princeton Instruments Acton SpectraPro®: Model SP-2500) in our laboratory. (c) Typical streak camera image: PL intensity *vs.* time and wavelength. (d) Operating principle of streak camera. (e) Operation timing of streak camera. (d,e) are extracted from Ref. [74].

2.3 Effects of hBN encapsulation on the optical and exciton properties

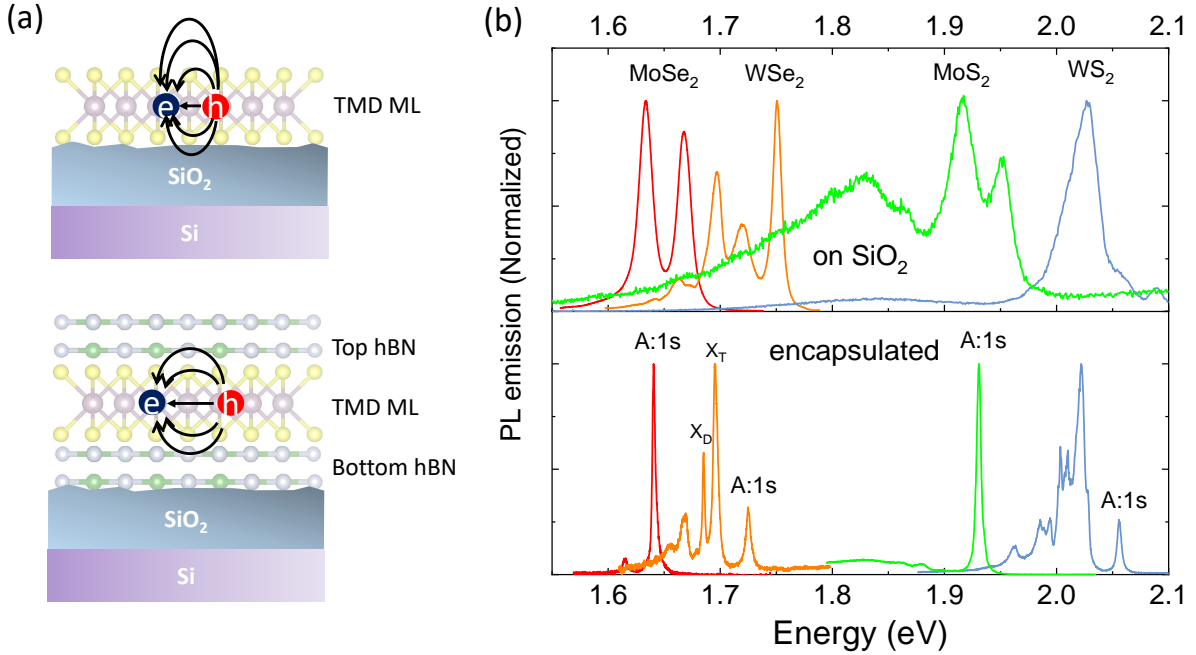


Figure 2.3.1: Improved optical properties of TMD MLs with hBN encapsulation. (a) Schematics of the sample structures of a TMD ML exfoliated directly on the SiO_2 and one encapsulated by hBN. hBN provides atomically flat interface and symmetrical dielectric screening which yields a larger exciton radius. (b) PL linewidth is narrowed in hBN encapsulated TMD MLs, approaching the homogeneous limit (extracted from Ref. [75]).

It is now well established that the encapsulation of TMD MLs with high quality hBN layers yields a drastic improvement of the optical properties [75, 76]. We recall here the main modifications of these properties induced by the hBN encapsulation. Figure 2.3.1(a) shows the sample structure contrast between TMD MLs exfoliated directly on SiO_2/Si substrate and encapsulated with hBN. Figure 2.3.1(b) shows the PL spectra at 4K of these two types of samples. The linewidths of the A:1s exciton states in four types of TMD MLs are much narrowed by hBN encapsulation, typically $1 \sim 4$ meV [75]. The narrow linewidth is a direct consequence of the reduction of the dielectric disorder due to atomically flatness of hBN and ultraclean interfaces. These values are now close to the homogeneous limit.

We also notice that hBN encapsulated Tungsten-based MLs have several emission peaks of excitonic complexes below A:1s, which can not be resolved for the monolayers on SiO_2 . The main difference of the two WSe_2 samples in Figure 2.2.5(b) and Figure 2.3.1(b) is the bulk hBN source. In Figure 2.2.5(b), we used hBN provided by our collaborators Catherine Journet-Gautier and Bérangère Toury-Pierre from Claude Bernard University of Lyon, France, whereas for WSe_2 sample in Figure 2.3.1(b), the bulk hBN is provided by our collaborators Kenji Watanabe and Takashi Taniguchi from NIMS in Japan. The exciton spectra of two WSe_2 MLs in Figure 2.2.5(b) and Figure 2.3.1(b) are very similar (in particular the narrow linewidths). This demonstrates that the “Lyon” hBN has

similar qualities for encapsulation compared to the worldwide used “NIMS” hBN.

The hBN encapsulation of TMD MLs does not only induce a reduction of the inhomogeneous broadening of the exciton lines, it also leads to a change of the exciton energies as a result of the change of the exciton binding energy and band gap renormalization due to the modification of the dielectric environment in the vicinity of the TMD MLs [22]. Finally, let us recall that the hBN encapsulation also greatly reduces photo-doping effects in TMD MLs [75, 77].

2.4 Conclusion

In this chapter, we have introduced confocal microscopy and several optical techniques including Differential Reflectivity, PL, PLE and TRPL. Through these measurements, we can get a comprehensive understanding of the absorption, emission and dynamics of the exciton states in TMD MLs. We have an upgraded home-built transferring setup in our glovebox for the all-dry viscoelastic stamping method of fabricating 2D van der Waals heterostructures. The hBN encapsulation has several effects on TMD MLs : (i) Renormalization of the bandgap (E_g) and the reduction of exciton binding energy (E_B); (ii) Protect TMD MLs from photodoping; (iii) Remove inhomogeneity and dielectric disorder, leading to narrowed exciton linewidth approaching homogeneous limit and (iv) tune the visibility of exciton states due to Fabry-Perot effect.

Chapter 3

Spin-Forbidden Dark Excitons in MoSe₂ and MoS₂ Monolayers

Knowledge of the exciton fine structure is essential to understand the optoelectronic properties in Transition Metal Dichalcogenide monolayers (TMD MLs). Here we measure the exciton fine structure of MoS₂ and MoSe₂ MLs encapsulated in hBN by magnetophotoluminescence (PL) spectroscopy in magnetic fields up to 30 T. The experiments performed in transverse magnetic field reveal a brightening of the spin-forbidden dark excitons: we find that the dark excitons appear 14 meV below the bright ones in MoS₂ ML and are 1.4 meV above the bright ones in MoSe₂ ML. Measurements performed in tilted magnetic field provide a conceivable description of the neutral exciton fine structure. The tilted magnetic field mixes the four exciton states, which allows us to measure the dark exciton g-factors of - 6.5 in MoS₂ ML and - 8.6 in MoSe₂ ML. These experimental results are in good agreement with a model taking into account the effect of the exchange interaction on both the bright and dark exciton states as well as the interaction with the magnetic field.

The chapter is organized according to the following sections:

- 3.1. Exciton fine structures in TMD monolayers
 - 3.1.1. Symmetry analysis of exciton states
 - 3.1.2. Exciton states coupling and interaction with magnetic field
- 3.2. Spin-forbidden dark excitons in MoSe₂ monolayer
- 3.3. Spin-forbidden dark excitons in MoS₂ monolayer
- 3.4. Conclusion

3.1 Exciton fine structures in TMD Monolayers

As for other semiconductor nanostructures, the exciton fine structure in TMDs dictates the efficiency of optical coupling. One can expect that the optoelectronic properties will change drastically whether the spin-forbidden dark excitons lie below or above the bright excitons [39, 78–80]. Exciton spin relaxation is also expected to be affected by the bright - dark exciton ordering [81, 82]. The main difficulty to experimentally determine the energy of spin-forbidden dark excitons is their extremely small oscillator strength compared to the bright excitons. The exciton fine structure splitting were accurately determined for WS_2 and WSe_2 MLs using various experimental techniques [71, 72, 83, 84]. These measurements were successful only in WSe_2 and WS_2 materials as the dark excitons lie several tens of meV below the bright ones so that the small oscillator strength is compensated by a very large population of dark excitons relaxed from the A:1s bright exciton, making them observable in PL experiments. Figure 3.1.1 shows the already determined dark excitons in WSe_2 MLs, extracted from Refs. [71, 72, 85].

In contrast the respective alignment of bright and dark excitons in MoS_2 ML remains controversial though this material is the most studied among the 2D semiconductors and was the first member of the TMD family to be established as a direct gap in the monolayer form. Numerous ab-initio calculations have been proposed to predict the exciton bright - dark splitting but the results are highly dispersed with values in the range 10 - 40 meV and more importantly with different signs: depending on the methods applied, dark excitons lie above or below the bright ones [86–89]. It is therefore crucial to have a clear experimental determination. Unfortunately, all attempts to measure the bright - dark splitting in MoS_2 ML were not conclusive so far. The main reasons were related to (i) low optical quality of samples (without hBN encapsulation) [90], (ii) the small value of the expected splitting compared to the luminescence/absorption linewidth or (iii) low thermal population of dark states if they lie above the bright ones [71].

In Subsection 3.1.1, we firstly perform the symmetry analysis on the exciton fine structures in the TMD MLs. In the Subsection 3.1.2, we further demonstrate the coupling between exciton states and their interaction with the magnetic fields. These analyses have been performed by Thierry Amand in our group on the basis of group theory.

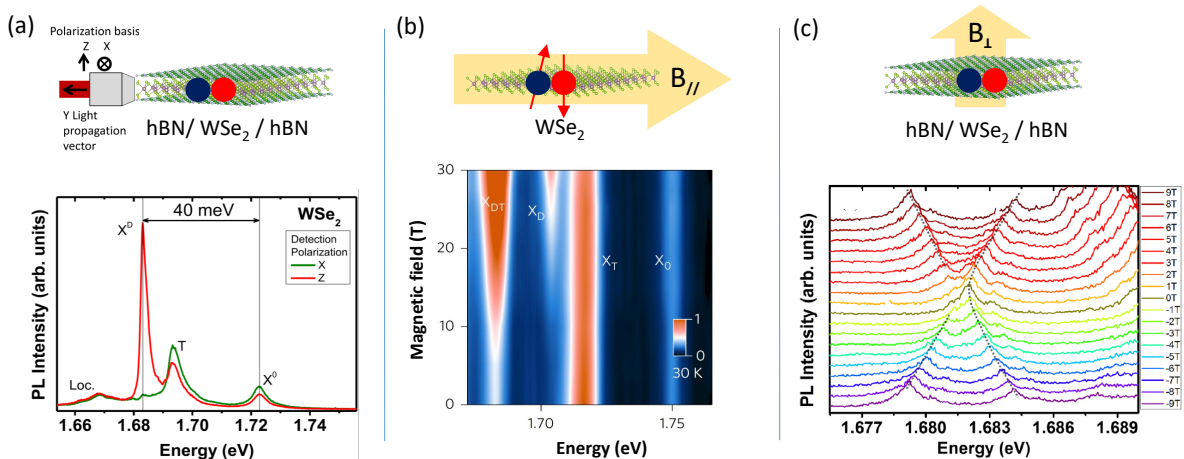


Figure 3.1.1: Dark excitons in WSe_2 MLs. (a) Dark exciton state X_D : spin-forbidden but dipole-allowed in z-direction; emission in-plane, LPCNO Toulouse [71]. (b) Dark excitons X_D brightened by transverse magnetic field. [72]. (c) A longitudinal magnetic field couples the two dark exciton states, LPCNO Toulouse [85].

3.1.1 Symmetry analysis of exciton states

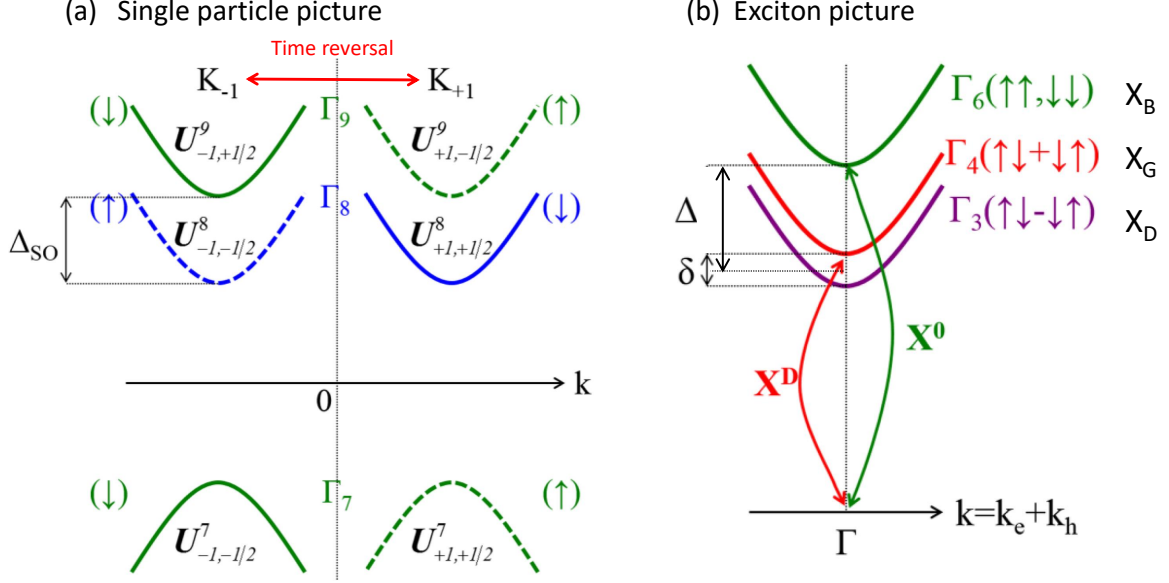


Figure 3.1.2: Tungsten-based TMD MLs. (a) **Sketch of free particle band structure:** a complete set of electron eigen-states in the irreducible representations of D_{3h} . $U_{\pm 1, m}^\gamma$ represents the Bloch amplitude of electron or hole that has representation index γ and effective spin index m in non-equivalent $K_{\pm 1}$ valleys. (b) **Sketch of exciton fine structure for A:1s excitons** ($K \approx 0$): The arrows \uparrow and \downarrow represent the main spin contribution of conduction and valence electrons [same as (a)] involved in the exciton states. Two bright exciton states X_B ($\uparrow\uparrow$ and $\downarrow\downarrow$, Γ_6 symmetry) and two dark exciton: grey state X_G ($\uparrow\downarrow + \downarrow\uparrow$, Γ_4 symmetry) and dark state X_D ($\uparrow\downarrow - \downarrow\uparrow$, Γ_3 symmetry). Δ and δ represent the bright - dark splitting and the two dark exciton splitting, respectively. Figures are extracted from Ref. [85]

The TMD materials crystallize in hexagonal structure which is invariant under the symmetry operations of the D_{3h} group [43]. The direct band gap is located at the edges of hexagonal Brillouin zone, at the non-equivalent valleys $K_{\pm 1}$. Because of the large spin-orbit splitting in the top valence band (VB), we restrict here our description to A:1s excitons composed of an electron from one of the two conduction bands (CB) split by the spin-orbit interaction Δ_{so} and a hole from the upper VB. We also consider only direct excitons (with a center of mass wave-vector $K=0$). Figure. 3.1.2 show the sketches of the single particle picture and exciton fine structure in a Tungsten-based TMD ML [85]. The exciton fine structure depends on several parameters, but nevertheless the symmetry analysis of the exciton states is supposed to be identical for all TMD MLs. Note that for a Molybdenum-based TMD ML, according to calculations, we need to change the sign of the electron spin-orbit splitting in the bottom CB, *i.e.* reverse the Γ_8 and Γ_9 subbands in Figure. 3.1.2(a).

Neglecting the valley indices of ± 1 for simplicity, the CB Bloch amplitudes U_m^γ in non-equivalent $K_{\pm 1}$ valleys belong to the D_{3h} representations: Γ_8 , Γ_9 being split by spin-orbit interaction, while the topmost VB ones belong to Γ_7 representation [91]. The electron-hole Bloch-amplitude pair functions built with these states belong thus to the representation product $\Gamma_9 \otimes \Gamma_7^* \otimes \Gamma_{env}$ and $\Gamma_8 \otimes \Gamma_7^* \otimes \Gamma_{env}$ in notations of [92]. Restricting ourselves to A:1s exciton ground states, we have $\Gamma_{env} = \Gamma_1$, so that, all the single particle representations are two-dimensional. We then obtain four exciton states in the A series

with symmetry $\Gamma_9 \otimes \Gamma_7^* = \Gamma_5 + \Gamma_6$ and four others with symmetry $\Gamma_8 \otimes \Gamma_7^* = \Gamma_3 + \Gamma_4 + \Gamma_6$. However, using coupling tables, it can be seen that only the Γ_6 - excitons of $\Gamma_9 \otimes \Gamma_7^*$ and Γ_3 - and Γ_4 - excitons of $\Gamma_8 \otimes \Gamma_7^*$ are direct excitons, the Γ_6 doublet and Γ_4 singlet excitons being only coupled to light (dipole allowed).

Defining the hole Bloch amplitude by $U_{\mp 1/2}^{h,7} = \pm \hat{K}(U_{\pm 1/2}^7)$, \hat{K} being the time-reversal operator, Bloch amplitudes for two degenerate bright exciton X_B with parallel spin $\uparrow\uparrow$ and $\downarrow\downarrow$ (Γ_6 symmetry) are denoted by:

$$\Psi_{\pm 1}^6 = U_{\mp 1/2}^9 \otimes U_{\mp 1/2}^{h,7} \quad (3.1)$$

These two bright exciton states can couple to σ^\pm photons, respectively. And also the Bloch amplitudes for the two non-degenerate spin-forbidden dark exciton are denoted by:

$$\Psi^4 = \frac{i}{\sqrt{2}}(U_{+1/2}^8 \otimes U_{-1/2}^{h,7} + U_{-1/2}^8 \otimes U_{+1/2}^{h,7}), \quad (3.2a)$$

$$\Psi^3 = \frac{1}{\sqrt{2}}(U_{+1/2}^8 \otimes U_{-1/2}^{h,7} - U_{-1/2}^8 \otimes U_{+1/2}^{h,7}). \quad (3.2b)$$

Ψ^4 is called grey state X_G ($\uparrow\downarrow + \downarrow\uparrow$, Γ_4 symmetry) because it is the only one coupled to π^z photons (the Z-exciton mode [91]), whereas Ψ^3 is a totally dark state X_D ($\uparrow\downarrow - \downarrow\uparrow$, Γ_3 symmetry) that does not couple to light, see Figure 3.1.2(b). The dark states splitting δ is caused by short-range exchange interaction between X_G ($\uparrow\downarrow + \downarrow\uparrow$) and X_D ($\uparrow\downarrow - \downarrow\uparrow$). Note that the bright - dark splitting Δ is defined as the energy gap from two degenerate X_B to the middle point between X_G and X_D .

3.1.2 Exciton states coupling and interaction with magnetic field

The bright -dark exciton splitting Δ is expressed as $\Delta = \Delta_{so} + \Delta_{bind} + \Delta_{exch}$, where Δ_{so} is the CB spin-orbit splitting, Δ_{bind} is the difference between the binding energies of bright and dark excitons due to the slightly different masses of spin \uparrow and spin \downarrow conduction bands and Δ_{exch} is the short range exciton exchange energy, see Figure 3.1.2(b) and Refs. [87-89]. In the direct exciton manifold with basis $B = \{\Psi_{+1}^6, \Psi_{-1}^6, \Psi^3, \Psi^4\}$, the effective exciton Hamiltonian, taking into account exchange and spin-orbit interaction [93], can be written as:

$$H_{exch} = \frac{1}{2} \begin{pmatrix} \Delta & 0 & 0 & 0 \\ 0 & \Delta & 0 & 0 \\ 0 & 0 & -\Delta - \delta & 0 \\ 0 & 0 & 0 & -\Delta + \delta \end{pmatrix} \quad (3.3)$$

We turn now to the action of an external magnetic field $\hat{\mathbf{B}}$ applied to the sample in any direction, and derive the corresponding Zeeman effective Hamiltonian. We write its components in spherical coordinates as:

$$\hat{\mathbf{B}} = (B \sin \theta \cos \varphi, B \sin \theta \sin \varphi, B \cos \theta)^T \quad (3.4)$$

For the longitudinal part of the magnetic field $\hat{\mathbf{B}}_z = B_z \hat{\mathbf{e}}_z = B \cos \theta \hat{\mathbf{e}}_z$ (z is the direction perpendicular to the plane), this component belongs to Γ_2 representation of D_{3h} point group. Thus, a pure longitudinal magnetic field splits the states Ψ_{+1}^6 and Ψ_{-1}^6 and

couples the states Ψ^3 and Ψ^4 . Using the coupling tables of [93], we have shown that this Hamiltonian can be presented in the form:

$$H_{B_z} = \frac{1}{2}\mu_B B \cos(\theta) \begin{pmatrix} g_z^B & 0 & 0 & 0 \\ 0 & -g_z^B & 0 & 0 \\ 0 & 0 & 0 & ig_z^D \\ 0 & 0 & -ig_z^D & 0 \end{pmatrix} \quad (3.5)$$

For the transverse part of the magnetic field $\hat{\mathbf{B}}_{//} = B_x \hat{\mathbf{e}}_x + B_y \hat{\mathbf{e}}_y = B \sin \theta \cos \varphi \hat{\mathbf{e}}_x + B \sin \theta \sin \varphi \hat{\mathbf{e}}_y$, we have $B_x \pm iB_y = B \sin \theta e^{\pm i\varphi}$ which transforms like the spin operators $\hat{S}_x \pm i\hat{S}_y$. These components and operators belong to Γ_5 two-dimensional representation of D_{3h} . The product of exciton states representations: $\Gamma_6^* \otimes \Gamma_6 = \Gamma_6 \otimes \Gamma_6 = \Gamma_1 + \Gamma_2 + \Gamma_6$, $\Gamma_3^* \otimes \Gamma_3 = \Gamma_3 \otimes \Gamma_3 = \Gamma_1 = \Gamma_4^* \otimes \Gamma_4$, $\Gamma_3^* \otimes \Gamma_4 = \Gamma_3 \otimes \Gamma_4 = \Gamma_2$ do not contain Γ_5 representation, but $\Gamma_6^* \otimes (\Gamma_3 + \Gamma_4) = 2\Gamma_5$. So it can be deduced that the transverse field only couples the Ψ^3 and $\Psi_{\pm 1}^6$ excitons, and the Ψ^4 and $\Psi_{\pm 1}^6$ excitons, with a *priori* two different coupling constants. The Zeeman Hamiltonian contribution of the transverse field can thus be presented under the form:

$$H_{B_{//}} = \frac{1}{2\sqrt{2}}\mu_B B \sin(\theta) \begin{pmatrix} 0 & 0 & g_{//}e^{-i\varphi} & ig_{//}e^{-i\varphi} \\ 0 & 0 & -g_{//}e^{+i\varphi} & ig_{//}e^{+i\varphi} \\ g_{//}e^{+i\varphi} & -g_{//}e^{-i\varphi} & 0 & 0 \\ -g_{//}e^{+i\varphi} & -ig_{//}e^{-i\varphi} & 0 & 0 \end{pmatrix} \quad (3.6)$$

where we have assumed for simplicity that the two coupling constants are opposite. This can be justified by the fact that only the conduction electrons contribute significantly to the coupling, because of the very large spin-orbit splitting in the valence band. The total Hamiltonian is thus, in the general case:

$$H^X = H_{exch}^X + H_{B_z}^X + H_{B_{//}}^X \quad (3.7)$$

We have checked that this Hamiltonian is strictly equivalent to the one written in [39] expressed in a different basis fabricated with states in each valley. Indeed, the secular equation of the Eigen-equation of the system is independent of the basis choice and is given by: $[(\Delta - 2\lambda)^2 - (g_z^B \mu_B B \sin \theta)^2][(\Delta + 2\lambda)^2 - (g_z^D \mu_B B \cos \theta)^2 - \delta^2] + 2(g_{//} \mu_B B \sin \theta)^2(\Delta^2 - 4\lambda^2 + g_z^B g_z^D \cos^2 \theta) + (g_{//} \mu_B B \cos \theta)^4 = 0$. As expected, one can easily check that the four Eigen-energies λ do not depend on the azimuthal angle φ of the magnetic field.

Note that this equation is also invariant when changing $g_{//}$ by $-g_{//}$, and by changing both signs of g_z^B and g_z^D , which shows that the sign of these two g-factors are linked. In the Hamiltonian 3.5, the bright exciton g-factor g_z^B is defined with the usual convention $g_z^B \mu_B B_z = E(\Psi_{+1}^6) - E(\Psi_{-1}^6)$ so that with $g_z^B < 0$ the energy of the bright exciton with the electron in K+ ($|\Psi_{+1}^6\rangle$ state) decreases when B_z increases. The definition of the dark exciton g-factor g_z^D is not so obvious in the Hamiltonian 3.5. To explain our convention we can write the two dark states in each valley:

$$|K_+^D\rangle = U_{+1/2}^8 \otimes U_{-1/2}^{h,7} = \frac{|\Psi^3\rangle - i|\Psi^4\rangle}{\sqrt{2}}, \quad (3.8a)$$

$$|K_-^D\rangle = U_{-1/2}^8 \otimes U_{+1/2}^{h,7} = -\frac{|\Psi^3\rangle + i|\Psi^4\rangle}{\sqrt{2}}, \quad (3.8b)$$

In the Hamiltonian 3.5, g_z^D is defined so that with $g_z^D < 0$ the energy of the dark exciton with the electron in K+ ($|K_+^D\rangle$ state) decreases when B_z increases.

3.2 Spin-forbidden dark excitons in MoSe₂ monolayer

As shown in the previous section, an in-plane magnetic field $\hat{\mathbf{B}}_{//}$ (Voigt geometry) mixes the spin components of the 2D exciton states [94, 95]. For a TMD ML, this field interacts with the CB electron within the exciton and we can neglect its interaction with the hole because of the very large spin-orbit splitting in the VB [72, 90]. As a consequence the in-plane magnetic field brightens both dark exciton states X_G and X_D ; the mixed bright - dark exciton states couple to in-plane polarized light allowing a straightforward determination of the energy of the dark states [72, 90]. On the other hand, an out-of-plane magnetic field $\hat{\mathbf{B}}_z$ (Faraday geometry) leads to the Zeeman splitting of the bright excitons of X_B and the mixing between dark states of X_G and X_D [85]. Thus, in tilted magnetic field, the four excitons are mixed and split, so that it becomes possible to extract the g-factor of the dark excitons. The (4x4) Hamiltonian describing the mixing between the four states under a given field with an angle θ with respect to the normal of the ML plane ($\theta = 90^\circ$ for Voigt and $\theta = 0^\circ$ for Faraday geometries) has been given in Eq. 3.7.

We will firstly evidence the energy of the spin-forbidden dark excitons in hBN encapsulated MoSe₂ MLs by Magneto-PL in the Voigt configuration at 4.2 K. The high-quality hBN encapsulated MoSe₂ MLs are fabricated in our laboratory by applying the all-dry viscoelastic stamping method described in Chapter 2. In collaboration with Clément Faugeras and Marek Potemski from LNCMI-Grenoble, the experiments are carried out by using an optical-fiber-based insert placed in a high static magnetic field up to 30T produced by resistive magnet, see the optical setup in Figure 3.2.1(a).

Figure 3.2.1(b) presents the 2D PL map of the hBN encapsulated MoSe₂ ML in Voigt configuration. One peak starts to be visible above the bright exciton (X_B) at a magnetic field ~ 8 T. We tentatively ascribe it to the brightened dark excitons (labeled X_D). The energy of the two lines (X_B and X_D) vary significantly with $\hat{\mathbf{B}}_{//}$, as a simple two-level model predicts. In that case, the energies of the bright and dark states simply write:

$$\text{bright : } E_{X_B} = E_{mid} - \frac{1}{2}\sqrt{\Delta^2 + (g_{//}\mu_B B_{//})^2} \quad (3.9a)$$

$$\text{dark : } E_{X_D} = E_{mid} + \frac{1}{2}\sqrt{\Delta^2 + (g_{//}\mu_B B_{//})^2} \quad (3.9b)$$

where E_{mid} is the energy of the middle point between bright and dark exciton states at zero external magnetic field.

Using the more general Hamiltonian presented in the Eq. 3.6, including the effect of the exciton exchange interaction and the external magnetic field, we can easily calculate the $\hat{\mathbf{B}}_{//}$ field dependence of the X_B , X_G and X_D exciton energies. Taking $\theta = 90^\circ$ (Voigt geometry) and $\delta = 0.6$ meV, we can fit our data [black solid lines in Figure 3.2.1(d)] with $\Delta = -1.4 \pm 0.1$ meV and $g_{//} = 2.0 \pm 0.2$. These values are in good agreement with very similar measurements published very recently [96]. Note that the fit is very weakly sensitive to the value of δ (we can only infer that $\delta < 1$ meV), since the linewidths of the transitions (1.4 meV for X_B and 2.4 meV for X_D) do not allow us to resolve the splitting between X_G and X_D excitons, see Figure 3.2.1(c).

In order to have a full description of the exciton fine structure, we have measured the Magneto-PL spectra of MoSe₂ ML in a tilted magnetic field configuration (the field is oriented 45° with respect to the 2D layer plane). These experiments allow the determination of several key parameters, such as the dark exciton g-factors. In an oversimplified

description, one can consider separately the effect of the two field components on the exciton spectra. The in-plane component of the field yields the mixing of the bright and dark exciton as already observed in the Voigt configuration and the out-of plane component leads to a Zeeman splitting of the states. While the energy splitting between the two spin/valley states for the bright exciton depends linearly with this z-component field (the slope given by effective g-factor), the field dependence of the dark states is more complicated since the two dark states at zero field are split by the exchange energy δ of the order of a few hundreds of μeV [83, 85], see also Figure 3.1.2(b).

We present the dependence of the PL spectra of MoSe_2 ML in tilted magnetic field. At high magnetic field (above ~ 12 T), the color map of the PL intensity in Figure 3.2.2(a) and the PL spectra in 3.2.2(b) clearly evidence 4 lines corresponding to the 4 exciton states whose energy vary almost linearly with the field in the range 15 - 30 T (i.e. the out-of plane component varying from ~ 10 to 21 T). For lower magnetic field values,

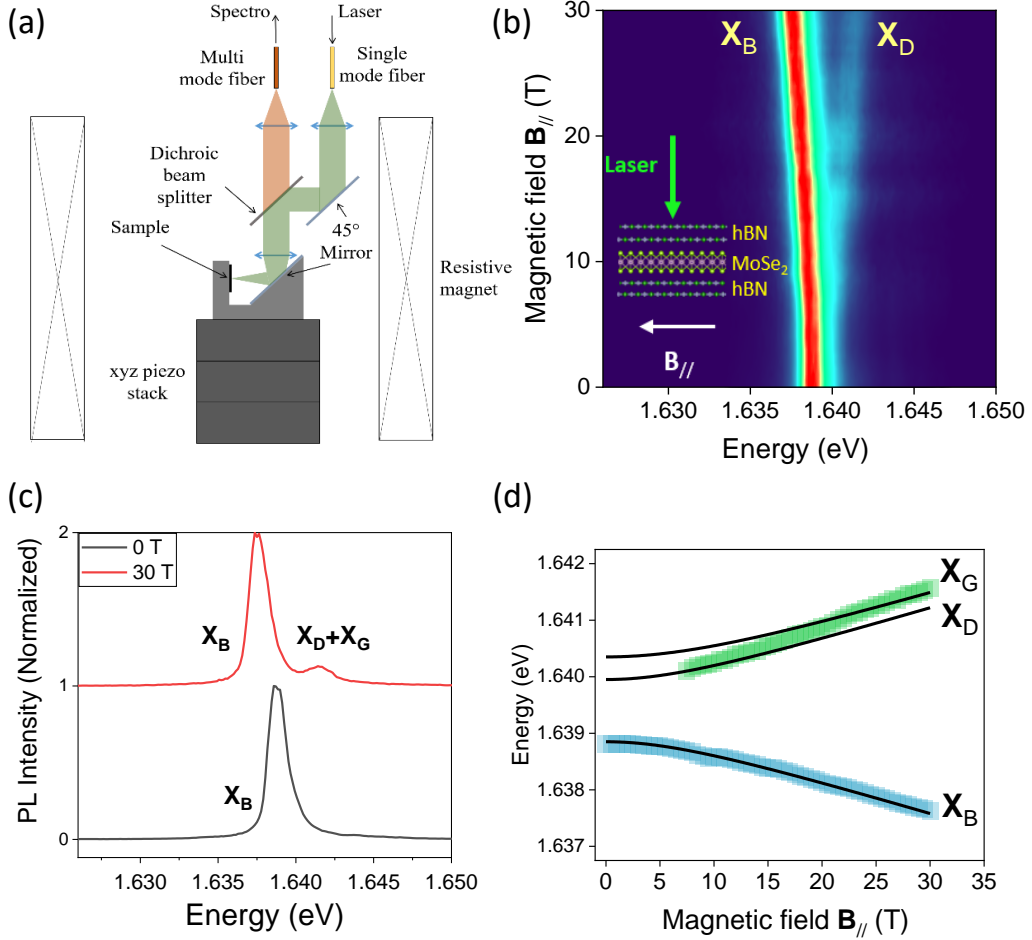


Figure 3.2.1: Spin-forbidden dark excitons in hBN encapsulated MoSe_2 ML revealed by Magneto-PL (Voigt geometry). (a) Sketch of the optical setup in Voigt geometry in LNCMI-Grenoble. For tilted field experiments, the sample is directly glued on the bottom 45° mirror. (b) Color map of the variation of the PL intensity as a function of $\mathbf{B}_{//}$. The PL intensity of the bright exciton has been normalized at each field. (c) Selected cross-sections of the PL color map in (b) at 0 and 30 T. X_D and X_G can not be resolved. (d) Energy of bright and dark excitons as a function of $\mathbf{B}_{//}$. The solid lines correspond to the fit by using Hamiltonian 3.6.

the energy splitting between the states is comparable to the PL linewidth preventing an accurate determination of the energy of the 4 states. However, we observe a clear non-linear dependence of the energy of the main PL line (which corresponds to the bright exciton at $B = 0$), see Figure 3.2.2(c). This is a consequence of both the effects of the zero-field bright - dark splitting Δ and zero-field splitting between two dark states δ .

Thus, the rigorous description requires to consider both the exciton interaction with the tilted magnetic field $\hat{\mathbf{B}} = \hat{\mathbf{B}}_z + \hat{\mathbf{B}}_{//}$ and the exciton exchange interaction; $B_{//} = B \sin\theta$ and $B_z = B \cos\theta$ are the magnetic field intensities of the components parallel and perpendicular to the monolayer plane ($\theta = 45^\circ$ in the experiments). The interaction with the magnetic field is driven by g_z^B and g_z^D , which are respectively the exciton g-factor of bright and dark excitons and $g_{//}$, which is the in-plane electron g-factor.

The eigenstates for each magnetic field value have been obtained numerically by solving the eigenfunction of Hamiltonian 3.7. On the basis of this model and using the values $\Delta = -1.4$ meV and $g_{//}$ obtained from the Voigt experiments (Figure 3.2.1), one can fit simultaneously the field dependence of the energy of the 4 lines presented in Figure 3.2.2(c) (see the solid line for the calculated curves of eigenvalues). The model agrees very well with the experiments. Interestingly, a clear anti-crossing is evidenced in the low field region as a consequence of the interplay of the transverse and longitudinal field components. This fitting procedure yields the g-factors of both the bright and dark states: we find $g_z^B = -4.0$ and $g_z^D = -8.6$. The value of the dark exciton g-factor around -9 is very similar to the values in WSe₂ ML [83, 85]; it is an additional proof of the highlighting of the spin-forbidden dark states. As we cannot extract the energy of the 4 lines at weak magnetic field due to their linewidths, the fit is not very sensitive to the zero field splitting δ between X_G and X_D (the curves have been calculated for $\delta = 0.6$ meV, the value measured in WSe₂ ML [83, 85]). Note that the 4 lines in the tilted magnetic field are actually mixed states between bright and dark excitons. The labeling of the 4 lines 1, 2, 3 and 4 in Figure 3.2.2 only correspond to X_{B+} , X_{B-} , X_D , X_G at zero field. In Figure 3.2.2(d), we show the mixing of each state as a function of tilted magnetic field intensity. By calculating the eigenvectors we can determine the weight of each component (Ψ_{+1}^6 , Ψ_{-1}^6 , Ψ^3 , Ψ^4) in the exciton states at 30 T. The results presented in Table 3.2.1 below for MoSe₂ ML show that the states are indeed strongly mixed.

weight basis vectors (exciton states)	Calculated eigenvalues	Calculated eigenvalues			
		1.6342 eV	1.6371 eV	1.6409 eV	1.6458 eV
$\Psi_{+1}^6 (X_{B+})$		0.2479	0.7521	0	0
$\Psi_{-1}^6 (X_{B-})$		0	0	0.9325	0.0675
$\Psi^3 (X_D)$		0.3964	0.1331	0.0302	0.4402
$\Psi^4 (X_G)$		0.3557	0.1148	0.0373	0.4923

Table 3.2.1: Weight in module of the 4 components (Ψ_{+1}^6 , Ψ_{-1}^6 , Ψ^3 , Ψ^4) in the 4 eigenvalues of MoSe₂ ML calculated at 30 T for $\theta = 45^\circ$ tilted field. The main components are shown in red.

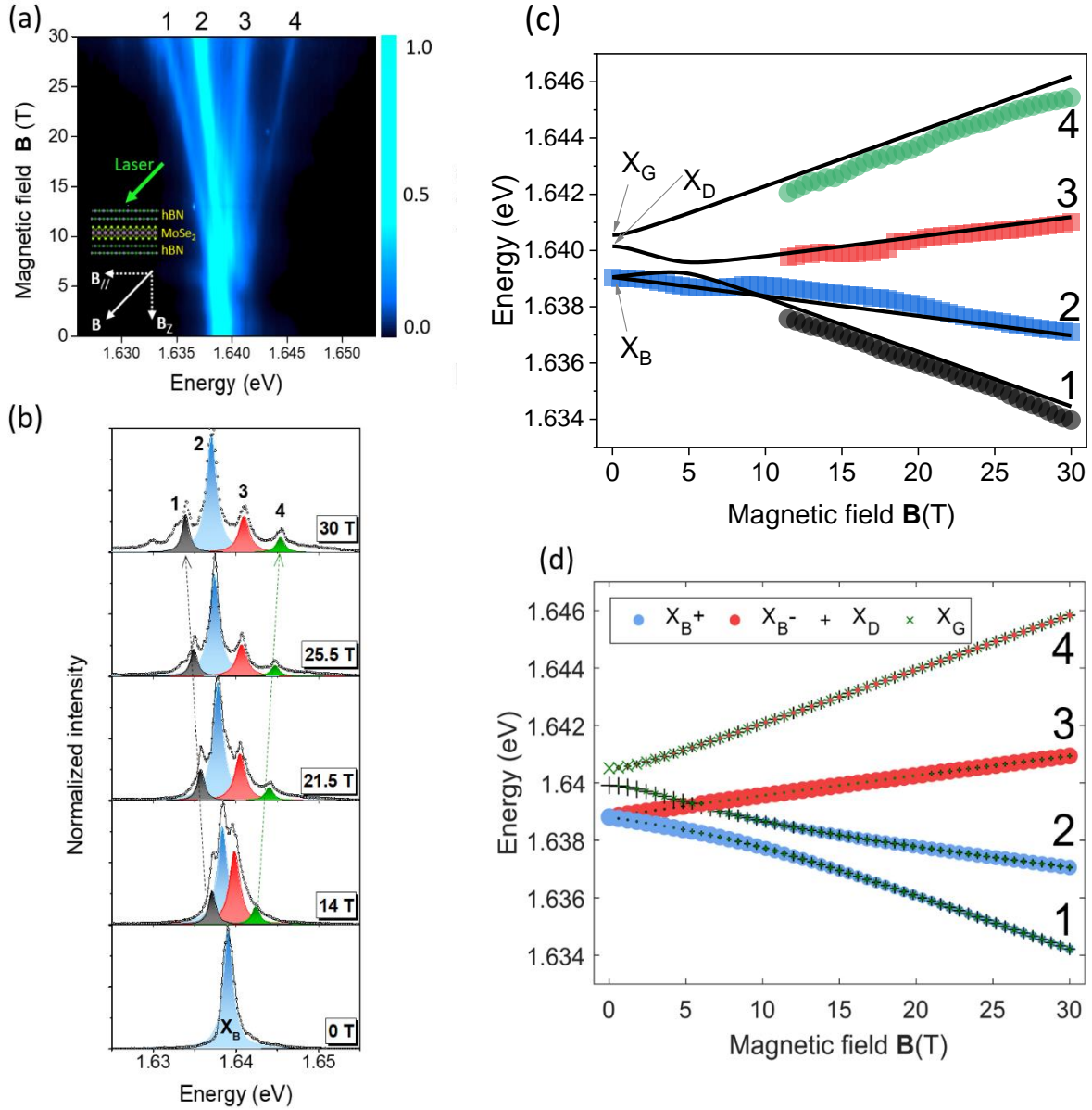


Figure 3.2.2: Tilted magnetic field ($\theta = 45^\circ$) –The four mixed exciton states (labeled 1, 2, 3 and 4) in MoSe₂ ML revealed by Magneto-PL. (a) Color map of the variation of the PL intensity as a function of magnetic field. (b) PL spectra for magnetic fields from 0 to 30 T showing the emergence of the four mixed exciton states (the intensity is normalized to the strongest exciton line labeled 2). (c) Magnetic field dependence of the energy of the four mixed exciton states. The full lines are fits to the model described in Section 3.1.2. The notations dark exciton (X_D), grey exciton (X_G) and bright excitons (X_B) are only strictly valid at 0 T. (d) Same fitting results than in (c). The size of each symbol is proportional to the weight of each component (the two bright component X_{B+} and X_{B-} and the two dark components X_G and X_D).

3.3 Spin-forbidden dark excitons in MoS₂ monolayer

We have also evidenced the energy of the spin-forbidden dark excitons in hBN encapsulated MoS₂ MLs using the same experimental approach as for the MoSe₂ ML. First we have investigated the effect of an in-plane magnetic field $\hat{\mathbf{B}}_{//}$ (Voigt configuration) on the low temperature PL spectra in MoS₂ ML. The 2D color map of PL intensity as a function of magnetic field from 0 T to 30 T is plotted in Figure 3.3.1(a). Figure 3.3.1(b) shows several cross-sections of the PL contour map in (a) at selected field intensity. In zero-field, the emission is composed of a unique line corresponding to the radiative recombination of the bright exciton X_B at 1.931 eV in agreement with previous reports [34]. Remarkably we observe at low energy, typically 14 meV below X_B , an additional peak which shows up above ~ 12 T. This feature, interpreted as the brightened spin-forbidden dark exciton, has been reproduced on several samples and spot positions (not shown here, see [97]). In principle, this line should correspond to both brightened X_G and X_D excitons, but the inhomogeneous linewidth in our samples is too broad (the FWHM of X_D is 5 meV) to enable us to distinguish the expected small splitting δ between the X_G and X_D states.

In a simple two-level system where the in-plane magnetic field couples the X_G and X_D states, one expects that the PL intensity ratio between the bright and the dark PL lines follows a simple quadratic law : $I_D/I_B \sim (B_{//})^2$, where $B_{//}$ is the in-plane magnetic field [72]. In Figure 3.3.1(c), we present the magnetic field dependence of the ratio between the PL intensity of the low energy and the high energy lines (corresponding to exciton states dominated by dark and bright components respectively). The measured quadratic behavior is a strong indication that the low energy line corresponds to the recombination of the dark excitons brightened by the transverse magnetic field.

An additional evidence for assigning the low-energy line observed for large in-plane magnetic field to spin forbidden dark excitons is the measurement of its g-factor in an external field perpendicular to the ML.

We have measured the excitons spectra of MoS₂ ML in tilted magnetic field ($\theta = 45^\circ$). Due to the larger PL linewidth compared to the one of MoSe₂ ML, it is more difficult to evidence the 4 excitons states as in Figure 3.2.2. However the energy of the two Zeeman split dark states (labeled as 1 and 2) can be extracted above 15 T as shown in Figure 3.3.2(a, b). Figure 3.3.2(c) displays the measured magnetic field dependence of the energies of the four states together with the fit based on the same model as MoSe₂. Using $\Delta = + 14.0$ meV and $g_{//} = 2$ (determined previously in the Voigt geometry), the best fit is obtained for $g_z^B = - 1.8$ and $g_z^D = - 6.5$. The bright exciton g-factor of about $g_z^B \sim -2$ was already measured in high quality MoS₂ ML [75]. The large value of g_z^D is in good agreement with the predicted one in a simple model [98] and the measured one in WSe₂ MLs [85]. Figure 3.3.2(d) shows the mixing of 4 exciton states as a function of tilted magnetic field intensity. And also the calculated weight of the 4 components at 30T is shown in Table. 3.3.1.

To the best of our knowledge this is the first direct experimental evidence of the spin-forbidden dark exciton in MoS₂ ML. Interestingly, we note that the g-factors of both bright and dark excitons are significantly smaller in MoS₂ than in other TMD materials. We can speculate that this is due to the very small conduction band spin-orbit splitting. Similar to the MoSe₂ ML, the fit is not sensitive to the value of the $X_D - X_G$ splitting δ due to the lack of experimental data at low field (the calculation has been done for

$\delta = 0.6$ meV). Table. 3.3.2 summarizes the parameters of the exciton fine structure of MoS₂ and MoSe₂ MLs measured here, together with the ones of WS₂ and WSe₂ MLs from previous works.

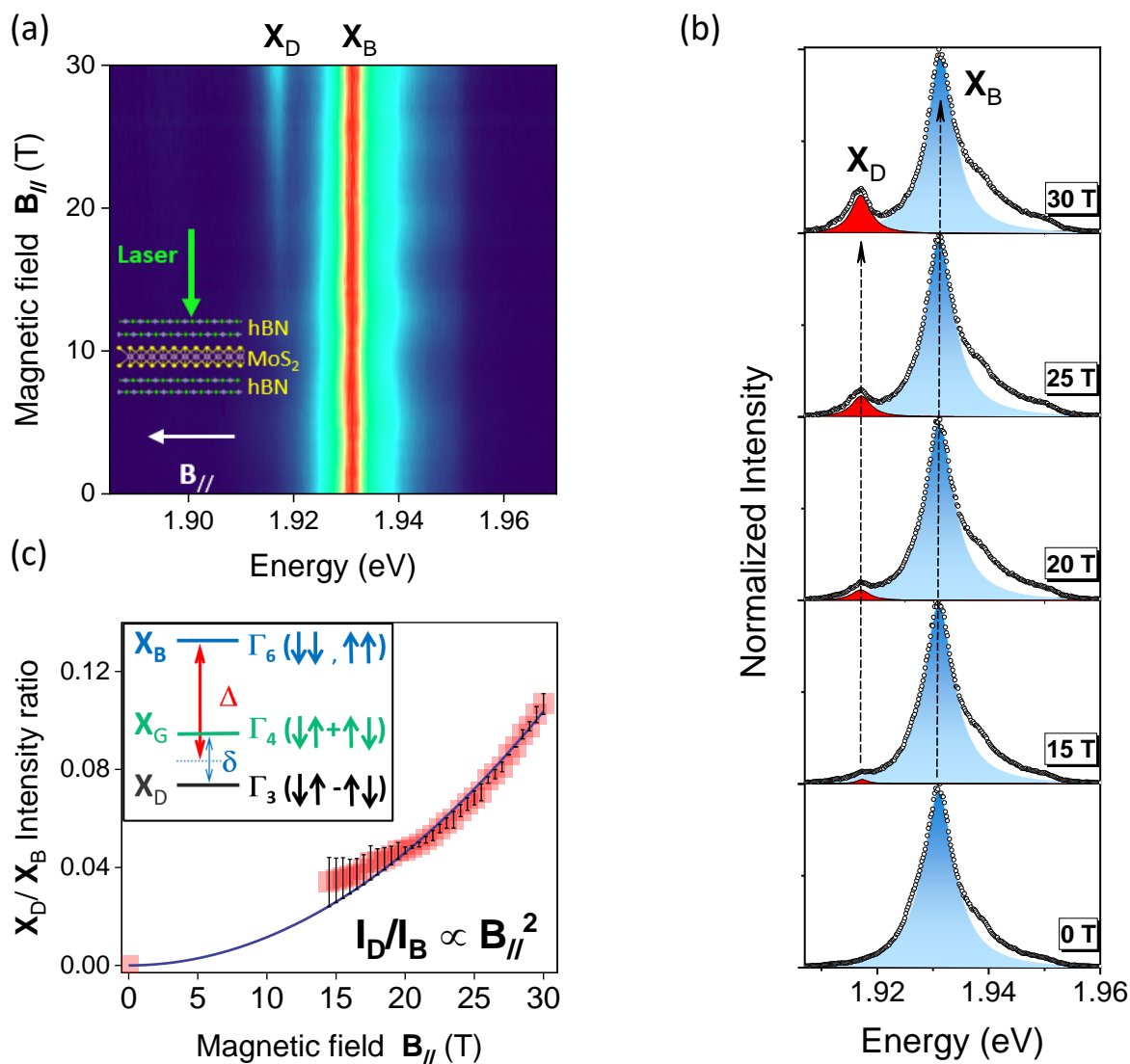


Figure 3.3.1: Spin-forbidden dark excitons in hBN encapsulated MoS₂ ML revealed by Magneto-PL (Voigt geometry). (a) Color map of the variation of the PL intensity as a function of $B_{//}$ (the PL intensity of the bright exciton X_B has been normalized at each field). (b) PL spectra for magnetic fields from 0 T to 30 T showing the emergence of the brightened dark excitons line (X_G and X_D can not be resolved) ~ 14 meV lower in energy than X_B . (c) Ratio of the PL intensity of dark excitons line ($X_G + X_D$) and bright (X_B) excitons as a function of magnetic field. Inset: sketch of the excitonic fine structure in MoS₂ ML [same as the sketch for Tungsten-based ML in Figure 3.1.2(b)].

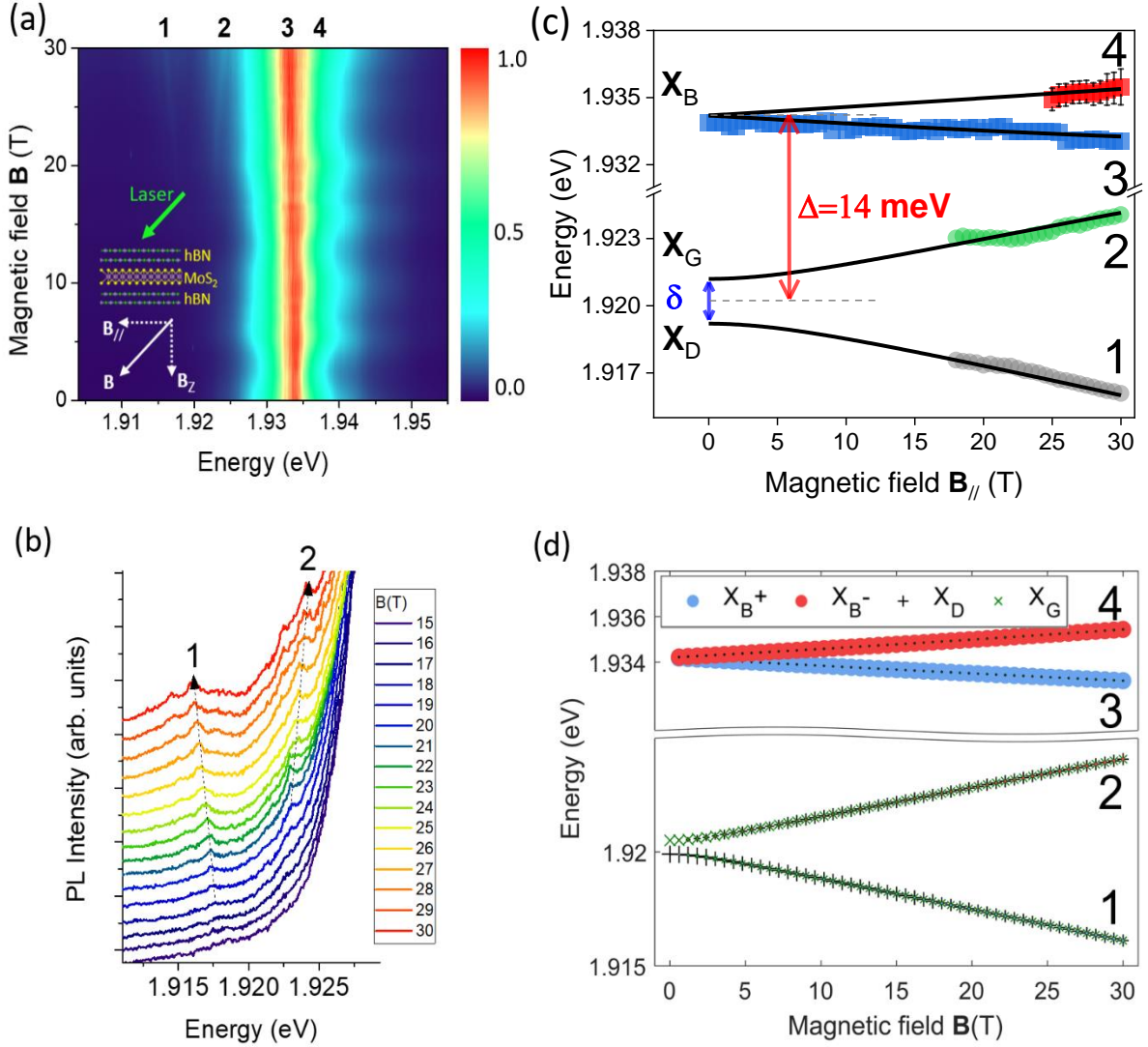


Figure 3.3.2: Tilted magnetic field ($\theta = 45^\circ$) –The four mixed exciton states (labeled 1, 2, 3 and 4) in MoS₂ ML revealed by Magneto-PL. (a) Color map of the variation of the PL intensity as a function of magnetic field. (b) PL spectra for magnetic fields from 15 T to 30 T showing the emergence of the two lowest energy states 1 and 2 (mainly with X_G and X_D components). (c) Magnetic field dependence of the energy of the four mixed exciton states. The full lines are fits to the model described in Section 3.1.2. The notations of dark exciton (X_D), grey exciton (X_G) and bright excitons (X_B) are only strictly valid at 0 T. (d) Same fitting results than in (c). The size of each symbol is proportional to the weight of each component (the two bright components X_{B^+} and X_{B^-} and the two dark components X_G and X_D), See Table 3.3.1 for the calculated weight of the four mixed exciton states at 30 T.

weight basis vectors (exciton states)	Calculated eigenvalues	1.9161 eV	1.9241 eV	1.9332 eV	1.9354 eV
	$\Psi_{+1}^6 (X_{B+})$	0.0052	0	0.9948	0
$\Psi_{-1}^6 (X_{B-})$	0	0.0118	0	0.9882	
$\Psi^3 (X_D)$	0.5346	0.4572	0.0024	0.0057	
$\Psi^4 (X_G)$	0.4602	0.5310	0.0028	0.0061	

Table 3.3.1: Weight in module of the 4 components (Ψ_{+1}^6 , Ψ_{-1}^6 , Ψ^3 , Ψ^4) in the 4 eigenvalues of MoS₂ ML calculated at 30 T for $\theta = 45^\circ$ tilted field. The main components are shown in red.

parameters	TMD MLs			
	MoS ₂	MoSe ₂	WSe ₂	WS ₂
Bright and dark excitons splitting: Δ (meV)	+ 14	- 1.4	+ 40 ^[142,158]	+ 55 ^[142,158]
grey and dark excitons splitting: δ (meV)	< 2	< 1	0.6 ^[81,101]	-
Bright exciton g-factor: g_z^B	- 1.8	- 4	- 4.25 ^[125]	- 4.0 ^[40]
Dark exciton g-factor: g_z^D	- 6.5	- 8.6	- 9.4 ^[81,101]	-
Transverse electron g-factor: $g_{//}$	2	2	2	-

Table 3.3.2: Measured exciton fine structure parameters for hBN encapsulated MoSe₂ and MoS₂ MLs measured in this Chapter. The parameters from WSe₂ and WS₂ MLs are extracted from previous works ^[37, 71, 83–85, 99].

The measured bright - dark splitting of $\Delta = + 14$ meV in MoS₂ ML generates several remarks and interrogations.

(i). First it demonstrates the key role played by the exciton exchange energy contribution to the bright - dark energy splitting that is expressed as $\Delta = \Delta_{so} + \Delta_{bind} + \Delta_{exch}$. Although the actual value of the spin-orbit splitting Δ_{so} is not yet known, the most widely used calculated value in the literature is $\Delta_{so} = - 3$ meV. In a first approximation, the binding energy is proportional to the reduced mass of the exciton. Taking the calculated effective masses from [9] and the experimental value of the bright exciton binding energy from [99], we infer $\Delta_{bind} = + 8$ meV. As a consequence our measurement of $\Delta = + 14$ meV demonstrates that the exciton exchange energy Δ_{exch} is crucial to determine the amplitude and the sign of the bright - dark energy splitting Δ . Thus we deduce $\Delta_{exch} \approx +9$ meV (if indeed $\Delta_{so} = - 3$ meV and $\Delta_{bind} = + 8$ meV). Note that the CB spin-orbit splitting in MoS₂ ML has been recently estimated from transport measurements [100]; a splitting of about 15 meV was measured for an electron density of a few 10^{12} cm^{-2} . This value is 5 times larger than the calculated one, because of the significant band renormalization induced by many body effects.

(ii). Importantly our measurements show that the splitting between bright and spin-forbidden dark excitons in MoS₂ ML has an opposite sign compared to the calculated spin-orbit splitting in the conduction band. This could have important consequences for the trion fine structure [101].

(iii). Our measurements raise the question of the simple interpretation of MoS₂ as a “bright” material. Indeed the TMD MLs are usually divided into two categories: the so-called dark materials such as WS₂ and WSe₂ MLs where the spin-forbidden dark excitons lie at lower energy compared to the bright ones. As a consequence these monolayers are characterized by a rather weak luminescence yield at low temperature while the intensity increases with temperature due to thermal activation of bright states [39, 78–80]. In contrast MoX₂ MLs (X = S, Se or Te) are often considered as “bright” materials as they exhibit stronger PL intensity at low temperature than their W-based counterparts but their intensity drops with temperature. This difference was assumed to vouch for dark excitons lying above the bright ones in MoX₂. This bright-dark ordering has indeed been observed very recently for MoSe₂ ML [96] and confirmed by our measurements in Section 3.2. The measurements displayed in Figure 3.3.1 show that the ordering is surprisingly opposite in MoS₂ ML although the temperature dependence of the PL intensity in MoS₂ ML is very similar to MoSe₂ ML (decrease with increasing temperature). Thus we cannot use this simple argument to distinguish between a “bright” and a dark material as our results prove that the dependence of PL intensity with temperature in MoS₂ may be the result of a complex relaxation scheme between bright and dark states as well as its interplay with non-radiative channels.

In addition, we know that the grey exciton is coupled to π^z photons *i.e.* the z-exciton mode. One can wonder why the grey exciton cannot be detected at zero magnetic field using high numerical aperture objective (NA = 0.82, collection angle of 55°) like in WS₂ and WSe₂ [71]. Remarkably we note in Figure 3.3.1 that the PL intensity of the mixed dark-bright state in transverse magnetic field is very weak (compared to similar experiments performed in WS₂ or WSe₂ MLs [71, 102] and that very high field are required to sizably observe it (larger than 14 T). We can speculate that either the oscillator strength of grey exciton is much smaller than in WX₂ and/or that their population

remains weak despite lying at lower energy than the bright state. We can tentatively explain the small oscillator strength by noticing that the smaller spin-orbit interaction in MoS₂ compared to WS₂ or WSe₂ may yield a weaker oscillator strength of the grey exciton since it is related to the spin-orbit mixing with higher energy bands [71, 89]. For the population issue, we can notice that contrary to WX₂, the bright - dark exciton splitting in MoS₂ ML is smaller than the optical phonon energies which can lead to inefficient relaxation between bright and dark excitons (the Γ_5 phonon that allows relaxation from bright to dark exciton is 36 meV) [103, 104].

Another striking difference between TMD materials is the amplitude of spin/valley polarization for excitons. While strong valley polarization and valley coherence have been measured in WSe₂, WS₂ and MoS₂ MLs, the polarization in MoSe₂ and MoTe₂ MLs is very weak [105, 106] except under quasi-resonant excitation where significant polarization has been measured for the trion in MoSe₂ [107]. Recently, it was proposed that a crossing of bright and dark exciton dispersion curves combined with a Rashba effect associated with local fluctuations of electric field can lead to very fast spin relaxation [82]. Our measurements of bright dark splitting in MoS₂ and MoSe₂ are perfectly consistent with this scenario: the small negative splitting $\delta = - 1.4$ meV in MoSe₂ combined with a larger effective mass for dark excitons should lead to a crossing between bright and dark dispersions while the positive splitting $\Delta = + 14$ meV in MoS₂ guarantees no crossing and as a consequence significant spin/valley exciton polarization measured in MoS₂ MLs under CW optical orientation experiments [42, 108, 109].

3.4 Conclusion

We have performed Magneto-PL experiments in transverse and tilted magnetic fields (45°) up to 30 T in high quality hBN encapsulated MoS₂ and MoSe₂ MLs. These investigations yield the unambiguous determination of the bright - dark exciton splitting: $\Delta = + 14$ meV for MoS₂ and - 1.4 meV for MoSe₂; and the dark excitons g-factor: $g_z^D = - 6.5$ for MoS₂ and - 8.6 for MoSe₂. Such fundamental parameters are key elements to understand the optoelectronic and spin/valley properties of these 2D semiconductors as well as their associated van der Waals heterostructures.

Chapter 4

Control of the Exciton Radiative Lifetime and Linewidth

We have introduced in Chapter 2 the effects of hBN encapsulation on the optical spectra of TMD MLs: (1) strong reduction of inhomogeneity which leads to narrow optical transitions approaching the homogenous exciton linewidth; (2) reduction of exciton binding energy and renormalization of free carrier band gap as a result of increased dielectric constant; (3) tunable visibility and shape of the optical transitions in reflectivity depending on the hBN thickness due to Fabry-Perot effect. However its impact on homogeneous linewidth and the exciton radiative recombination dynamics due to possible modification of photon modes in these atomically layers has not been evidenced so far. This chapter demonstrates that the exciton radiative rate in these van der Waals heterostructures can be tailored by a simple change of the hBN encapsulation layer thickness as a consequence of the Purcell effect. Time-resolved photoluminescence (TRPL) measurements show that neutral exciton spontaneous emission time can be tuned by one order of magnitude depending on the thickness of the surrounding hBN layers. The inhibition of radiative recombination yields spontaneous emission time up to 10 ps. The analysis shows that we can also observe sizeable enhancement of exciton radiative decay rate. These results are in very good agreement with the recombination rate calculated in the weak exciton-photon coupling regime using the Transfer Matrix method developed in Chapter 2. Finally, understanding these electrodynamic effects allows us to elucidate the complex relaxation and recombination dynamics for both neutral and charged excitons (trion).

The chapter is organized according to the following sections:

- 4.1. Homogeneous linewidth
- 4.2. Purcell effect
- 4.3. Simulation of the optical field intensity
- 4.4. Sample fabrication and experimental methods
 - 4.4.1. Sample fabrication
 - 4.4.2. Experiment methods
- 4.5. Tuning of the spontaneous emission rate
 - 4.5.1. Purcell effect on neutral exciton dynamics and linewidth
 - 4.5.2. Complex dynamics of relaxation and recombination of exciton and trion
- 4.6. Conclusion

4.1 Homogeneous linewidth

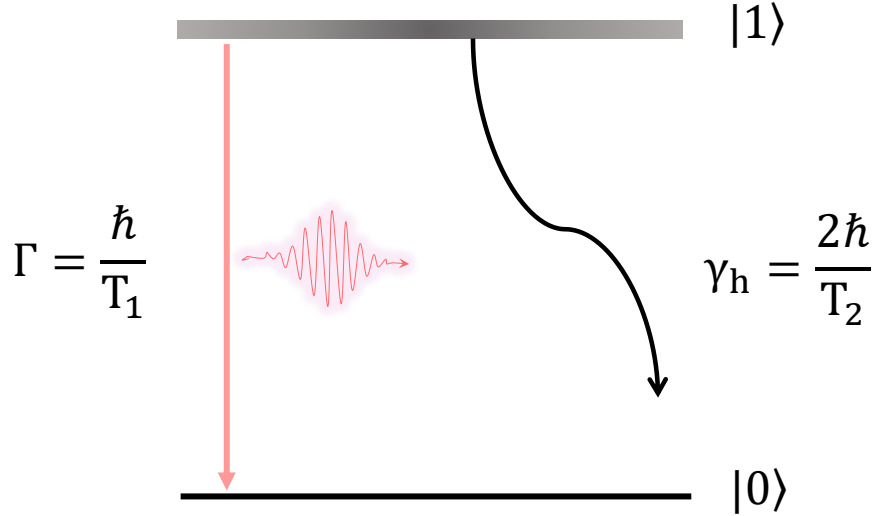


Figure 4.1.1: Simplified picture of the quantum dynamics of an exciton state $|1\rangle$. The homogeneous broadening (dephasing rate) is expressed as $\gamma_h = \frac{2\hbar}{T_2}$ that is related to population decay rate $\Gamma = \frac{\hbar}{T_1}$ and pure dephasing rate γ^* , through $\gamma_h = \Gamma + \gamma^*$.

In this section we briefly recall the mechanisms responsible for the homogeneous linewidth. We neglect any inhomogeneous broadening due to dielectric disorder, imperfections, etc.

Figure 4.1.1 shows in a two-level system such as the one formed by the exciton state $|1\rangle$ and the crystal ground state $|0\rangle$, the homogeneous linewidth γ_h which can be expressed as:

$$\gamma_h = \frac{2\hbar}{T_2} \quad (4.1)$$

where T_2 is the coherence time during which the exciton state $|1\rangle$ keep a fixed phase with respect to the crystal ground state $|0\rangle$. The homogeneous linewidth “ γ_h ” includes two contributions: the linewidth due to the population decay “ γ_1 ” (the coherence is lost when there are no more excitons) and the linewidth due to the pure dephasing processes “ γ^* ”:

$$\gamma_h = \gamma_1 + \gamma^* \quad (4.2)$$

The exciton population decay can be separated into two recombination channels: either radiative ($\gamma_{rad} = \frac{\hbar}{\tau_{rad}}$) or non-radiative ($\gamma_{nrad} = \frac{\hbar}{\tau_{nrad}}$) corresponding to trapping by defects, relaxation to other exciton states, Auger effects..., where τ_{rad} and τ_{nrad} are respectively the radiative and the non-radiative lifetimes of the exciton.

$$\gamma_1 = \frac{\hbar}{T_1} = \frac{\hbar}{\tau_{rad}} + \frac{\hbar}{\tau_{nrad}} \quad (4.3)$$

The pure dephasing term γ^* corresponds to any mechanism that elastically (*i.e.* without energy losses) breaks the coherence between states $|1\rangle$ and $|0\rangle$. It generally includes elastic exciton-exciton scattering (different from Auger effects) and exciton-electron (exciton-hole) scattering in a doped sample.

Determining these parameters first requires to discriminate between homogeneous and inhomogeneous linewidths. This can be done by non-linear optical techniques such as four-wave mixing (FWM). Moody *et al.* measured a residual homogeneous linewidth (residual means extrapolated at zero temperature and zero exciton density to avoid exciton-phonon and exciton-exciton scattering *i.e.* $\gamma^* \sim 0$) of 1.6 meV in a WSe₂ ML grown on a sapphire substrate by CVD [110]. Jakubczyk *et al.* measured a homogeneous linewidth of 0.78 meV at zero temperature in MoSe₂ ML on SiO₂ [111] and 2.1 meV in WS₂ ML on SiO₂ [112]. For hBN encapsulated samples, Boule *et al.* measured an homogeneous linewidth of 2.07 meV for MoSe₂ ML and 2.96 meV for WSe₂ ML [113]. Finally, Jakubczyk *et al.* reported values spanning from 1.8 meV to 4.3 meV for hBN encapsulated MoS₂ MLs [114], while Martin *et al.* claimed an homogeneous linewidth as low as 0.2 meV in hBN encapsulated MoSe₂ ML [115]. Despite the significant variance in the FWM measurements, we remark that these values are very close to the PL linewidth we get in our best encapsulated samples at low temperature and low exciton density, see Figure 2.3.1. We can thus conclude that the PL linewidth in our samples is very close to the homogeneous limit.

Going a step further, we remark that the PL linewidth of the bright exciton in MoSe₂ ML (~ 1 meV) is systematically smaller than the one in WS₂ or WSe₂ MLs (~ 3 meV), see also Figures 2.2.2 and 2.2.5. This is perfectly reasonable if we look at Eq. 4.3. In WS₂ or WSe₂ MLs, the bright exciton linewidth is broadened by non-radiative decay to lower lying dark excitons. On the opposite, we have shown in Chapter 3 that in MoSe₂ ML, the bright exciton state lies at lower energy than the dark ones. Consequently, we can assume that in undoped sample there is no relaxation channel toward lower excitonic states, so that MoSe₂ ML is an ideal material to reach a linewidth dominated by the radiative limit γ_{rad} . In 2018, Back *et al.* and Scuri *et al.* demonstrated that a MoSe₂ ML encapsulated into hBN could reflect up to 85% when it is resonant with the bright exciton transition [92, 116]. The MoSe₂ ML thus acts as a nearly perfect atomically thin mirror [117]. This is in fact a direct consequence of the radiatively limited linewidth. Indeed, in absence of non-radiative decay and pure dephasing processes, the backward (forward) re-emitted light constructively (destructively) interfere with the resonant incident light so that reflectivity (transmission) reaches 100% (0%). In the following, we will explore another consequence of this remarkable property in MoSe₂ ML: because the linewidth is dominated by the radiative decay, we can use the Purcell effect to simply tune the exciton lifetime or the linewidth.

4.2 Purcell effect

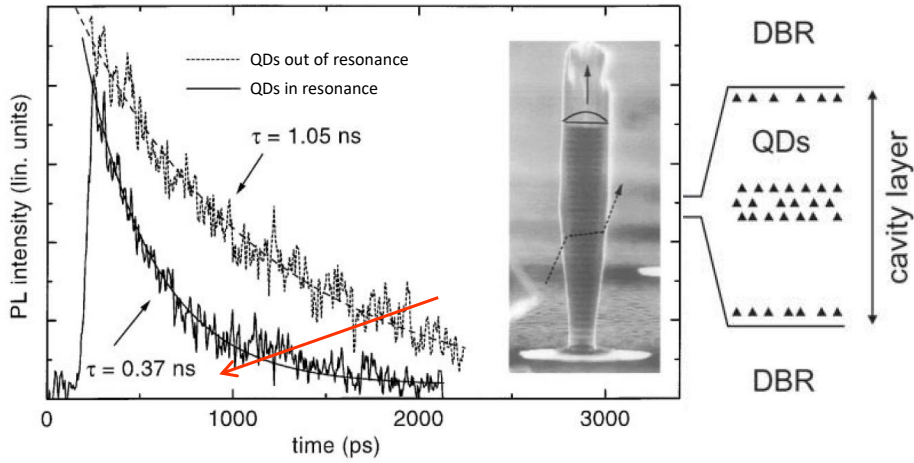


Figure 4.2.1: Quantum dots (QDs) confined in DBR mirrors. The QDs at the antinode of the cavity (QDs in resonance) have enhanced spontaneous emission rate, *i.e.* shorter lifetime.

The Purcell effect describes the modification of the spontaneous emission rate of a dipole by the control of the density of electromagnetic modes. When a dipole is weakly coupled to a cavity mode, its emission rate is enhanced (reduced) if the transition is resonant (non-resonant) with the cavity modes. It was first predicted by Edward M. Purcell in a short letter in 1946, where he described the change of spontaneous emission rate for a nuclear spin system coupled to a resonant electrical circuit [118]. It was then observed in many atomic systems where the spontaneous emission of atoms can be enhanced or inhibited depending on whether the transition is resonant or not with the photonic cavity [119, 120]. In solid state system, the strongest manifestations of the Purcell effect were demonstrated with 0D emitters (quantum dots) embedded in 3D microphotonic cavities such as microdisks, photonic crystals or DBR mirrors etched in a micropillar geometry [121–123], see Figure 4.2.1. In these systems, cavities with high quality factors (Q factor) of several thousands are required to observe significant variations of the radiative lifetimes. In the following, we will show that we can observe the Purcell effect in MoSe₂ MLs in a cavity-like system formed by the hBN, SiO₂ and Si layers.

4.3 Simulation of the optical field intensity

We consider our classical structure presented in Figure 2.2.4(a) composed of a SiO₂ (80 nm)/Si substrate and a MoSe₂ ML sandwiched between a bottom hBN layer and a thin top hBN layer. Using the Transfer Matrix method presented in Subsection 2.2.2, we first simulate the optical field (square of the electric field) in the structure top hBN/bottom hBN/SiO₂/Si. We assume that the TMD ML does not change the cavity modes due to its very small thickness ~ 6 Å. In Figure 4.3.1, we plot the intensity of the optical field at the location of the monolayer (between the top and bottom hBN layers) as a function of both bottom hBN thickness and wavelength. The Fabry-Perot interference effects and its dependence on the bottom hBN thickness are clearly seen. Knowing the emission wavelength of bright exciton in MoSe₂ ML (~ 756 nm), we can thus choose

the proper hBN thickness to tune the optical field in the monolayer. The two extreme cases corresponding to the monolayer located at the node or the antinode of the field are sketched in Figure 4.3.2. Due to the Purcell effect, we expect the radiative lifetime of the exciton to be longer (shorter) when the monolayer is located at the node (antinode).

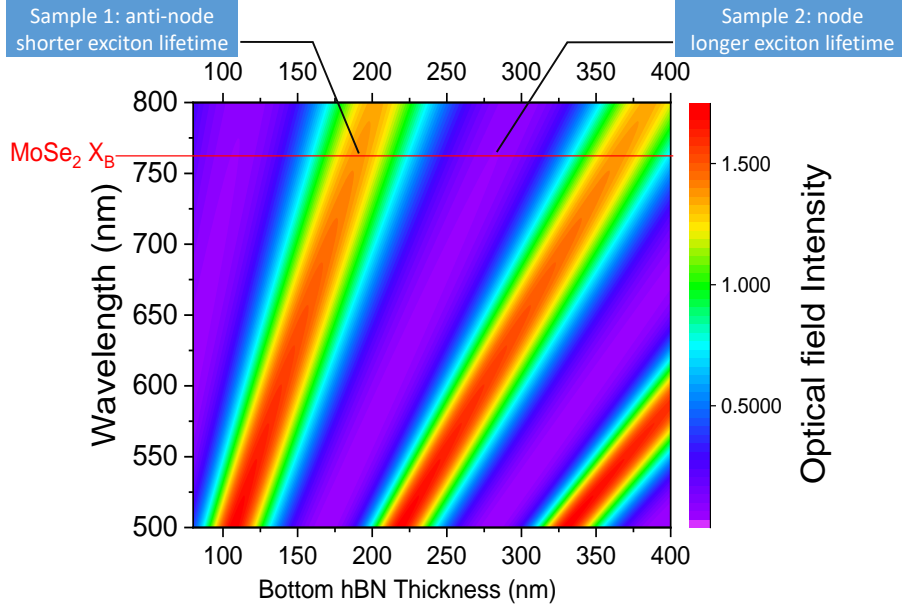


Figure 4.3.1: Optical intensity map calculated at the monolayer’s location as a function of both the emission wavelength and total hBN layer thickness. The horizontal red line corresponds to the A:1s (X_B) emission wavelength (~ 756 nm) in a MoSe₂ ML.

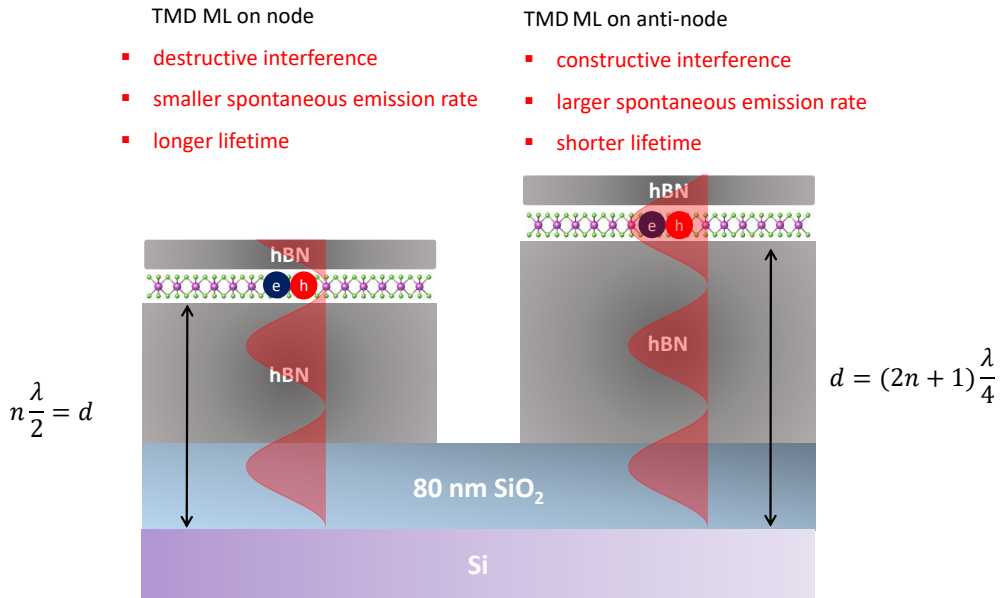


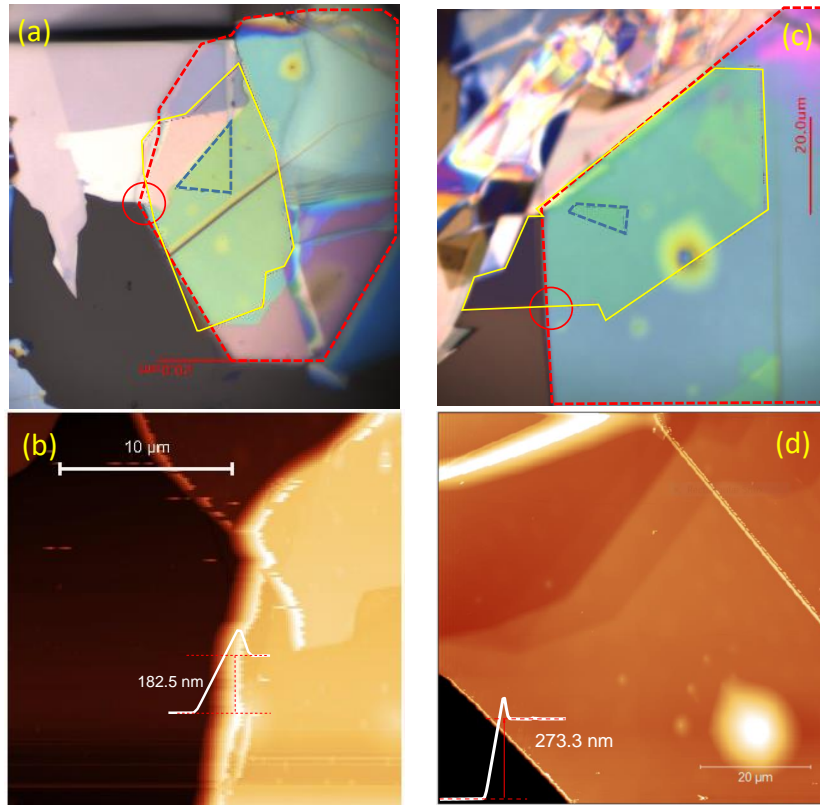
Figure 4.3.2: Sketch of MoSe₂ MLs sitting on the node and anti-node of the cavity consisted of dielectric layers of hBN and SiO₂ (80 nm). The total thickness of all the dielectric layers $d = n \frac{\lambda}{2}$ and $d = (2n+1) \frac{\lambda}{4}$ correspond to the node and anti-node, respectively. The red shades are simplified illustrations of optical field intensity. Real refractive index: $n_{SiO_2} = 1.46$, $n_{hBN} = 2.2$, Dielectric constant $\kappa_{hBN} = 4.5$. Note that λ is the wavelength in dielectric layers, $\lambda = \lambda_0/n$ where λ_0 is wavelength in vacuum and n is the refractive index of dielectric layers.

4.4 Sample fabrication and experimental methods

4.4.1 Sample Fabrication

We fabricated 5 different samples with different bottom hBN thicknesses which exhibit similar behaviour. We will present the results on four of them in Section 4.5.1. In Samples I and II, the bottom hBN thicknesses are firstly determined by the optical contrast in microscope images, see Figure 4.4.1(a,c). The accurate bottom hBN thicknesses are then determined by Atomic Force Microscopy (AFM) as 182.5 and 273.3 nm for Sample I and II, respectively, see Figure 4.4.1(b). These two thicknesses correspond to the MoSe₂ ML located at the anti-node (185 nm) or the node (275 nm) of the standing wave according to the simulated electric field distribution in Figure 4.3.1.

For the Sample III, the same MoSe₂ ML is deposited on a hBN flake exhibiting different terraces and steps with hBN thicknesses $d_{hBN} = 205, 240$ and 255 nm for zone A, B and C respectively, see Figure 2.1.2(e). Sample IV is similar to Sample III with two terraces $d_{hBN} = 125$ and 149 nm, see Figure 4.5.3(a,b). This allows us to investigate the exciton dynamics of the same MoSe₂ ML and different bottom hBN layer thicknesses. The top hBN thickness which does not play a key role here considering its small value is 9 nm, 7 nm, 8 nm and 8.5 nm in Sample I, II, III and IV, respectively.



Sample I: MoSe₂ on anti-node Sample II: MoSe₂ on node

Figure 4.4.1: Microscope image of (a) Sample I and (c) Sample II: yellow solid, blue dashed and red dashed contours are top hBN, MoSe₂ ML and bottom hBN. AFM measurements of bottom hBN thicknesses (b) Sample I, $d_{hBN} = 182.5$ nm and (d) Sample II, $d_{hBN} = 273.3$ nm measured on the red circled area in (a) and (c).

4.4.2 Experimental methods

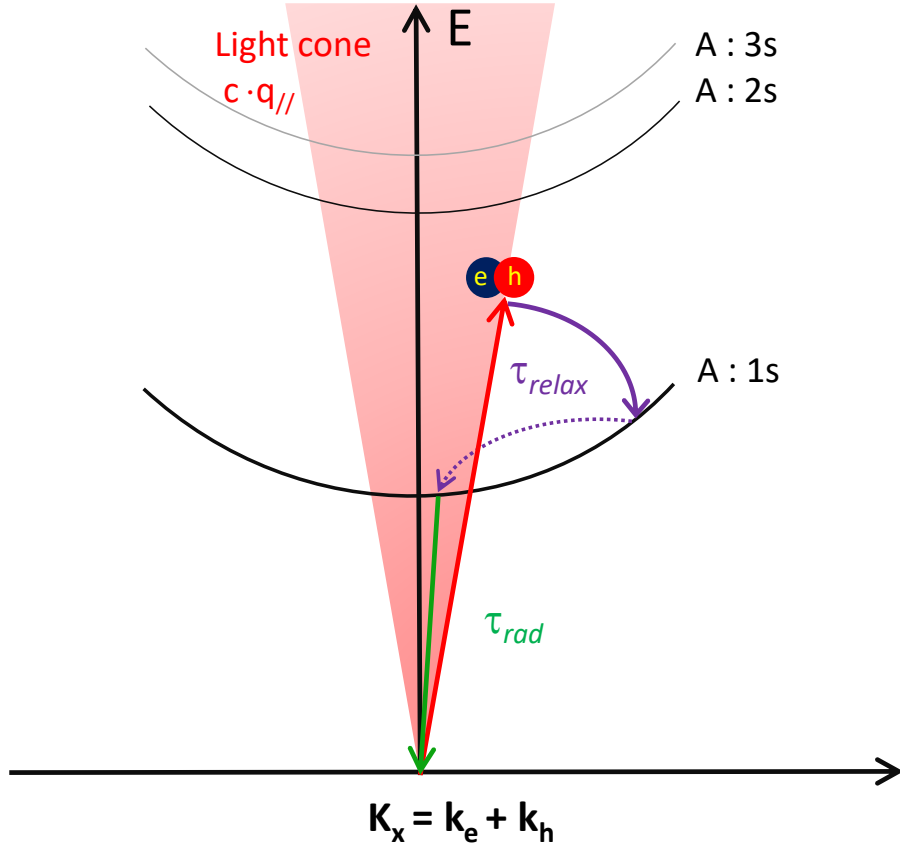


Figure 4.4.2: Sketch of non-resonant excitation, relaxation and radiative recombination in a MoSe₂ ML. A-exciton series and light cone (dispersion of light, $c \cdot q_{||}$) are shown for better illustration. Only the excitons that have small center-of-mass vectors within the lightcone are optically bright. The energy gap between A:1s and A:2s states is ~ 150 meV as will be determined in Section 5.1.1. Using a 712 nm pulsed laser for dynamics measurements, we excite hot excitons with a kinetic energy ~ 100 meV, between the A:1s and A:2s states. The excess kinetic energy of the hot excitons is relaxed by emitting phonons down to the light cone during a time of τ_{relax} . The cold excitons in the light cone then recombine radiatively during a time of τ_{rad} .

We investigated the exciton dynamics in different samples using the TRPL setup described in Subsection 2.2.3. In TRPL, we probe the dynamics of the population of excitons that recombine radiatively. This correspond to the cold excitons within the light cone. Ideally, to have access directly to the lifetime of excitons in the light cone, we need to excite resonantly. Unfortunately, this is technically challenging, since it is then difficult to filter out the laser back scattering from the PL that is at the same wavelength.

In a first approximation, we summarize our experiment in Figure 4.4.2. We non-resonantly excite the samples by using a pulsed laser of 712 nm, which means that we create hot excitons with kinetic energy ~ 100 meV above the A:1s exciton state (X_B emission ~ 756 nm). These hot excitons first need to relax down through phonon scattering to the light cone, where the relaxed cold excitons will then emit light (radiative recombination). The dynamics measured in TRPL thus depends on the lifetime of excitons (τ_{rad}) in the light cone and the relaxation time (τ_{relax}) between hot and cold excitons.

4.5 Tuning of the spontaneous emission rate

4.5.1 Purcell effect on neutral exciton dynamics and linewidth

4.5.1.1 Experimental results: neutral exciton dynamics

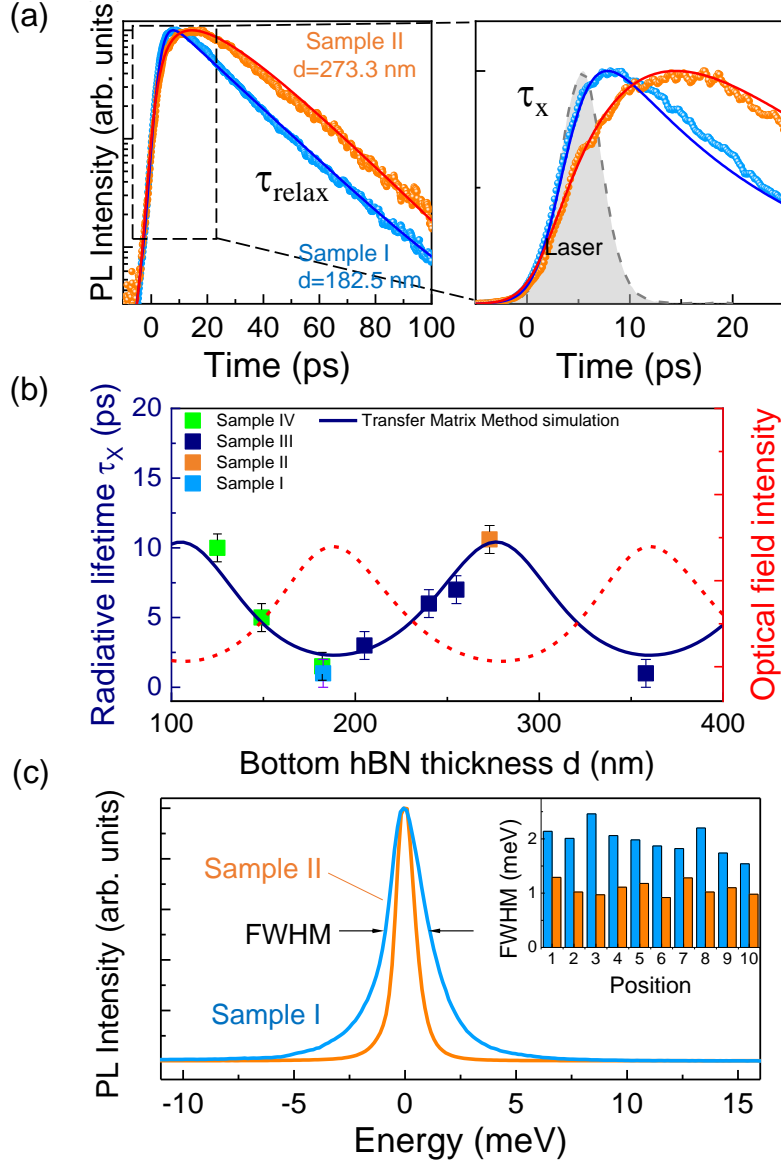


Figure 4.5.1: (a) Left: normalized photoluminescence intensity (log scale) of the neutral exciton X_B in time domain for Sample I ($d_{hBN} = 182.5$ nm) and Sample II ($d_{hBN} = 273.3$ nm); the full lines correspond to the bi-exponential fits. The instrument response is obtained by detecting the backscattered laser pulse (wavelength 712 nm) on the sample surface, see the dashed line labeled ‘Laser’; Right: zoom of the rise-time. (b) Calculated (full line) and measured (symbols) neutral exciton radiative lifetime as a function of the hBN bottom layer thickness. The red dashed curve is the calculated intensity of electromagnetic field in our structure (same calculation as in Figure 4.3.1). (c) Normalized CW PL intensity of the neutral exciton in Sample I and Sample II clearly shows the different linewidths. Because the energy of the PL peak slightly depends on the sample and sample’s position by a few meV, the origin of the energy axis is taken at the PL peak. Inset: PL linewidth (FWHM) for 10 different positions in Sample I and II.

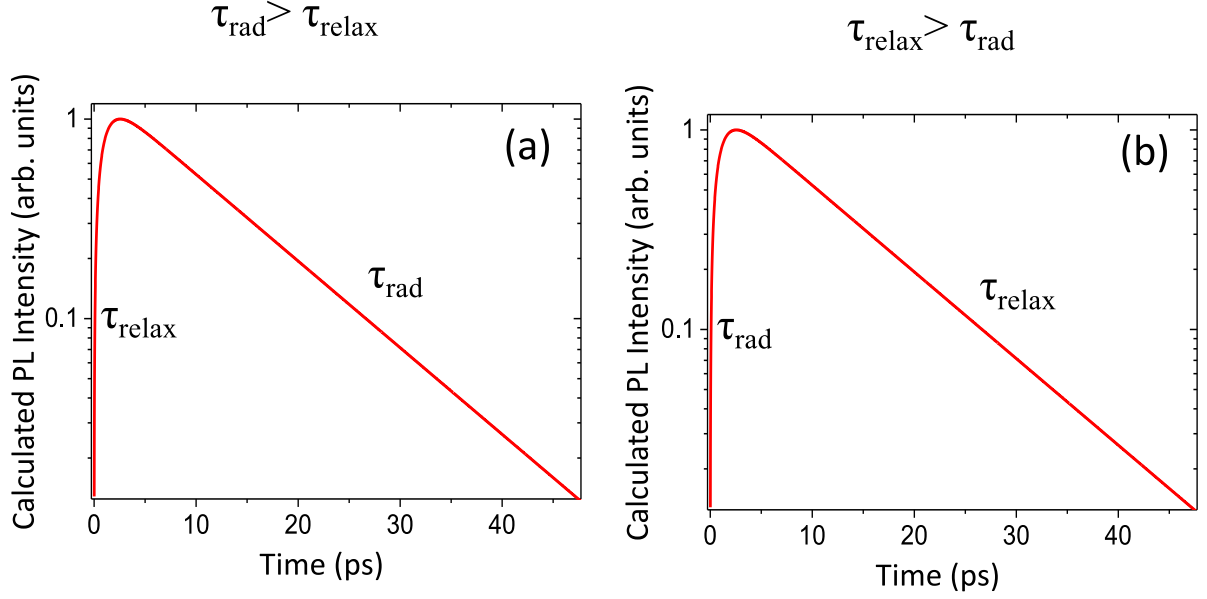


Figure 4.5.2: Calculated normalized TRPL intensity with (a) $\tau_{rad} > \tau_{relax}$ ($\tau_{rad} = 10$ ps, $\tau_{relax} = 1$ ps) and (b) $\tau_{relax} > \tau_{rad}$ ($\tau_{rad} = 1$ ps, $\tau_{relax} = 10$ ps). Two cases have identical PL intensity as a function of time.

Figure 4.5.1 presents the key results of this investigation. In Figure 4.5.1 (a), the normalized luminescence intensity dynamics of the neutral exciton (X_B) is plotted for Sample I and II (differing only by the bottom hBN thickness $d_{hBN} = 182.5$ nm and 273.3 nm respectively). While the decay time is similar in both samples with a typical value of ~ 18 ps, the PL rise time is clearly different: it is much shorter in Sample I (limited by the time-resolution of the set-up), compared to a value of ~ 10 ps in Sample II.

In general, the rise and decay rates of PL signal are determined by the interplay between the feeding rate of the radiative state and the recombination rate. In our case, the rise time of luminescence corresponds to the exciton radiative recombination time whereas the PL decay reflects the relaxation time of photogenerated excitons at higher energies towards the radiative states ($K \approx 0$). This counter-intuitive result is in part because the relaxation time, τ_{relax} , is longer than recombination time, τ_{rad} , and can be easily modeled with a basic two-level model as shown in the inset of Figure 4.5.6(b). We assume that the system can be described by the population of the ‘reservoir’ of photogenerated hot carriers n_{hot} and of the cold excitons n_X through Eqs. (4.4). Then the experimental results of exciton kinetics in Fig. 4.5.1 (a) are fitted with simple bi-exponential fits based on this simple two-level model.

$$\frac{dn_{hot}}{dt} = -\frac{n_{hot}}{\tau_{relax}}, \quad (4.4a)$$

$$\frac{dn_X}{dt} = -\frac{n_X}{\tau_{rad}} + \frac{n_{hot}}{\tau_{relax}}, \quad (4.4b)$$

where τ_{relax} is the relaxation rate of the hot excitons into the emitting states and τ_{rad} is the radiative decay rate of excitons. In Eqs. (4.4) we disregarded non-radiative recombination processes. Then the calculated exciton PL intensity simply writes:

$$I(t) \propto \frac{n_{hot}^{(0)}}{\tau_{relax} - \tau_{rad}} \left[\exp\left(-\frac{t}{\tau_{relax}}\right) - \exp\left(-\frac{t}{\tau_{rad}}\right) \right]. \quad (4.5)$$

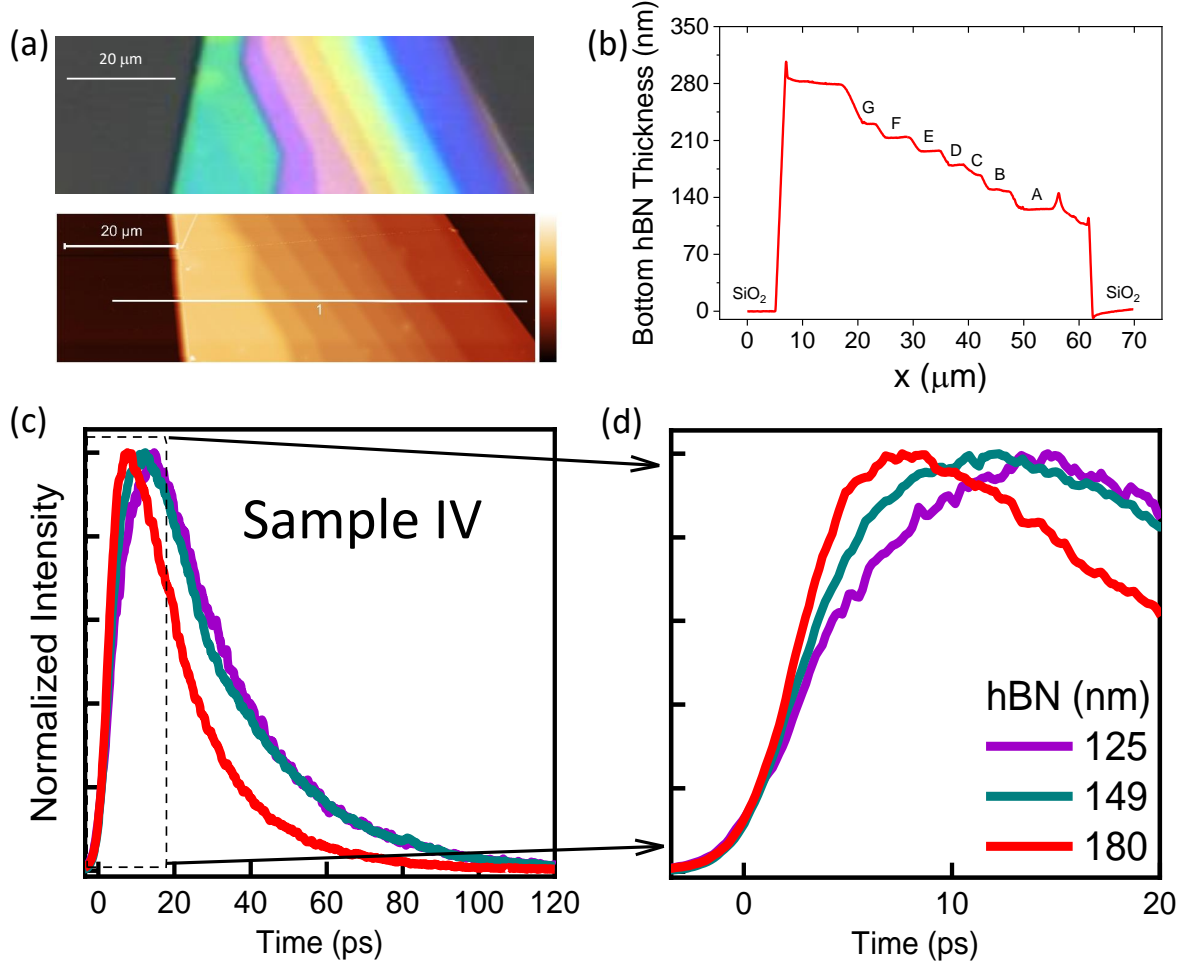


Figure 4.5.3: (a) Microscope image and AFM measurements of Sample IV bottom hBN terrace. (b) AFM cross section in (a) white line. $d_{hBN} =$ A: 125 nm, B: 149 nm, C: 167 nm, D: 180 nm, E: 197 nm, F: 214 nm, G: 230 nm, H: 279 nm and I: 274 nm. (c) Neutral exciton TRPL of MoSe₂ ML on 125 nm, 149 nm and 182 nm bottom hBN. (d) zoom-in of rise time of (c). Biexponential fittings give exciton radiative lifetimes of 1.5 ps, 5 ps and 10 ps.

Here $n_{hot}^{(0)}$ is the initial photogenerated population of the hot carriers. Note that depending on the relation between the relaxation and radiative times, the rise and decay time of the PL are controlled by different parameters. Figure 4.5.2 displays the corresponding calculated intensity for two cases: (a) $\tau_{rad} > \tau_{relax}$ and (b) $\tau_{relax} > \tau_{rad}$. Therefore, the rise-time does correspond to the radiative recombination time if $\tau_{relax} > \tau_{rad}$.

As a consequence, the PL decay time is not controlled by the radiative recombination time but it corresponds to the feeding time of the radiative states, see Figure 4.5.6 (b) for the fit on sample II. Taking into account the instrument response time, we find $\tau_{relax} = 18$ ps in both samples whereas $\tau_{rad} = 11 \pm 1$ ps is typically 10 times larger in Sample II compared to Sample I with $\tau_X < 1.5$ ps. This is exactly the expected behaviour due to the inhibition of the spontaneous lifetime in Sample II as the ML is located at the node of the electric field in the cavity-like structure, see Figure 4.3.1. Note that in previous measurements of the exciton dynamics in bare TMD MLs the radiative recombination time was assigned to the decay of the emission signal [124–126].

This control of the radiative lifetime by the cavity effect is further confirmed by the measurement of the excitonic dynamics in Samples III and IV where MoSe₂ MLs are deposited on two hBN flakes with several terraces. Figure 4.5.3 (c-d) show Sample IV has several different rise times, whereas the decay times are still ~ 18 ps. Sample III has similar behaviors, not shown here.

Figure 4.5.1(b) summarizes the exciton radiative lifetime as a function of the hBN thickness for all samples (obtained with the same fitting procedure as above). We clearly see that the period of oscillations of the radiative lifetime with bottom hBN thickness is perfectly consistent with the simulation as in Figure 4.3.1: the lifetime is shorter (longer) when the MoSe₂ ML is located at antinode (node) of the optical field.

Using the transfer matrix method developed by Mikhail Glazov and Marina Semina from Ioffe Institute that is introduced in Subsection 2.2.2, we can calculate the radiative lifetime as a function of the hBN thickness. In opposite to the result of Figure 4.3.1, we now simulate the whole structure including the MoSe₂ ML. Thus, in order to calculate the radiative lifetime τ_{rad} in our structure, we found numerically the absorbance, $\mathcal{A}(\omega)$ at $\Gamma_{nrad} \rightarrow 0$, and fitted it by Eq. (2.10c) and extracted Γ_{rad}^{eff} as a function of the bottom hBN thickness d_{hBN} . Then we obtain τ_{rad} simply by:

$$\tau_{rad} = \frac{1}{2\Gamma_{rad}^{eff}}. \quad (4.6)$$

The only free parameter in this simulation is the exciton radiative decay rate in the vacuum Γ_{rad}^{vac} . Assuming a free space radiative lifetime of MoSe₂ ML of $\frac{1}{2\Gamma_{rad}^{vac}} = 2.7$ ps, we find in Figure 4.5.1(b) that the measured radiative lifetime is in very good agreement with the calculated one (blue solid line).

Figure 4.5.1(b) demonstrates that the exciton spontaneous lifetime can be tuned by more than one order of magnitude depending on the hBN thickness. This is much larger than the small variations (10-30 % typically) reported previously with Bragg reflector microcavities using III-V semiconductor quantum wells as emitters [127, 128] where the linewidth was far from being dominated by radiative processes. In contrast, much larger modulations of the radiative lifetimes due to Purcell effect were evidenced in open cavities using metallic mirrors [129] or with 0D emitters embedded into 3D cavity with additional lateral mode confinement: a typical factor 10 was for instance reported for quantum dots embedded in micro-pillars [121, 122]. It is worth noting that contrary to quantum dots emitters, excitons in TMD MLs are 2D dipoles. The 2D exciton wavefunction of these delocalized emitters determines their emission to have a planar wave front, whereas the emission of quantum dots is more spherical. This means that a perfect confinement in 3 directions is needed to establish stable photonic modes and interact back with quantum dots to have maximum tuning of exciton dynamics. In contrast, the 2D nature of dipoles in TMD MLs only need confinement normal to the layer surface. It is therefore not surprising to observe a large tuning of the exciton radiative dynamics even using a cavity-like structure with rather low reflective coefficients.

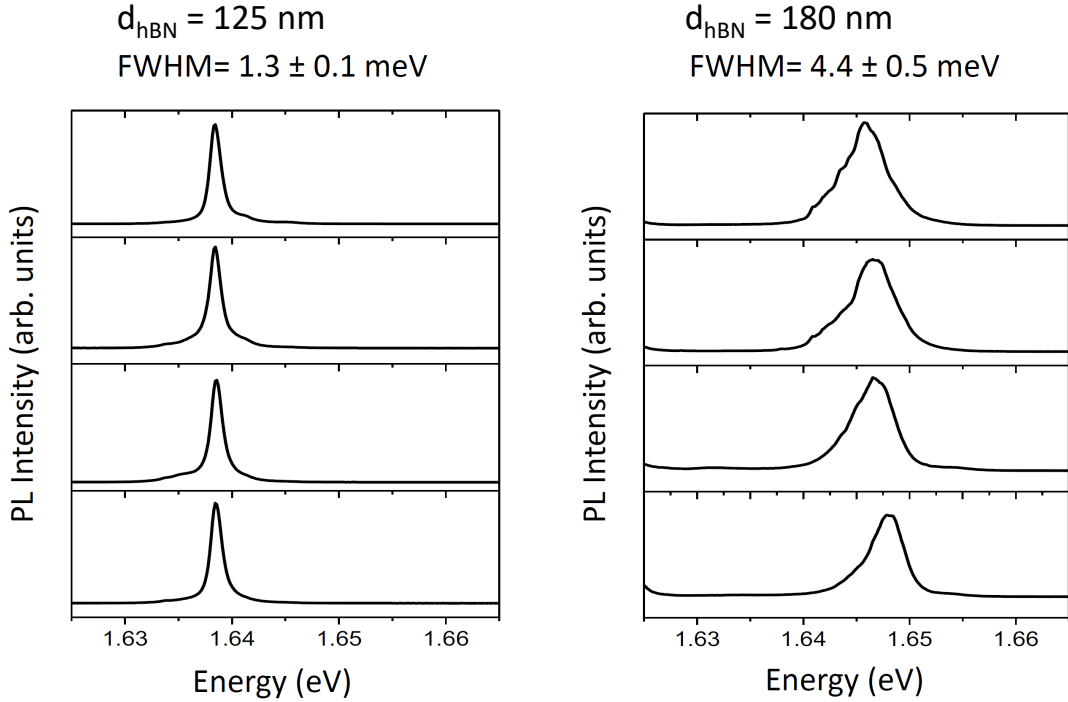


Figure 4.5.4: PL spectra at $T = 7$ K on two terraces of Sample IV corresponding to inhibition ($d_{hBN} = 125$ nm) and enhancement ($d_{hBN} = 180$ nm) of radiative decay rate. The linewidth measured on four different spots confirmed the trend of Figure 4.5.1, showing narrower (larger) linewidth for MoSe_2 MLs located at node (anti-node) of the optical field.

4.5.1.2 Experimental results: neutral exciton linewidth

A striking feature is that the cavity effect related to the hBN encapsulation has also a strong influence on the excitonic linewidth measured in CW PL spectroscopy. As shown in Figure 4.5.1(c), the CW PL linewidth is about twice smaller in Sample II (~ 1.1 meV FWHM) compared to the one in Sample I (~ 2.2 meV), a trend fully consistent with the expected variation of the radiative linewidth in Eq. (4.6), due to the cavity effect. It is clear that the linewidth usually includes both a homogeneous and a residual inhomogeneous contribution and the latter can fluctuate in different points of a given monolayer as a result of the local dielectric disorder. Nevertheless, the average of the measurements recorded for different points on the Sample II (with longer exciton τ_{rad}) is significantly lower than that on Sample I. From the measurements on 10 different points on each sample, inset of Figure 4.5.1(c), we find a linewidth (FWHM) of 1.1 ± 0.13 meV and 2.0 ± 0.25 meV on Sample II and I, respectively. As expected a larger linewidth is measured in Sample I characterized by a much shorter radiative lifetime, see Figure 4.5.1(a). This result is also confirmed for Sample IV for different cavity lengths, see Figure 4.5.4.

In principle, we could extract the radiative lifetimes directly from the measured linewidths if it was purely radiative. Nevertheless, the quantitative analysis of the linewidths we measure in CW PL have to be done with caution due to the residual inhomogeneous broadening and dephasing processes. We can tentatively estimate the radiative lifetime and radiative linewidth by combining the CW and time-resolved PL results. The TRPL measurements show that the radiative lifetime in Sample I is limited by the temporal resolution (we infer $\tau_{rad} < 1.5$ ps) while we measure ≈ 10 ps in Sample

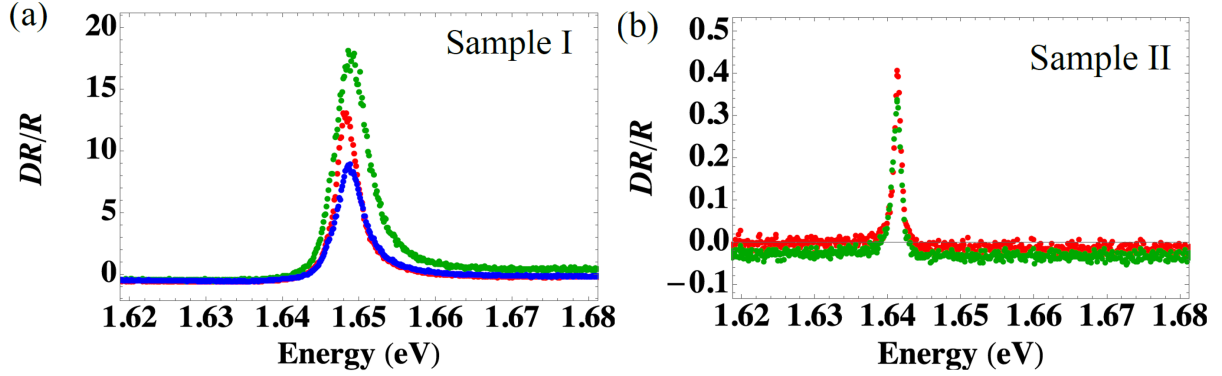


Figure 4.5.5: Reflection contrast, DR/R , measured in (a) Sample I and (b) Sample II in the vicinity of the exciton resonance. Different data points correspond to different sample spots.

II. The radiative linewidth is thus very small in Sample II: $\gamma_{rad} = \hbar/(\tau_{rad}) \approx 0.06$ meV. Thus the measured linewidth of 1.1 meV mainly correspond to dephasing processes and residual inhomogeneous broadening. Assuming that dephasing processes and inhomogeneous broadening are identical in both samples, we can deduce a radiative linewidth $\gamma_{rad} \approx 0.9$ meV in Sample I, corresponding to a radiative lifetime of $\tau_{rad} \approx 740$ fs. This value is close to previous estimations where the cavity effect was not considered [92, 111, 115, 116]. By comparing the measured radiative lifetime and the measured linewidth in CW PL, we find that the latter is not fully controlled by spontaneous emission time and inhomogeneity must still be considered. This is fully consistent with recent FWM experiments performed on similar MoSe₂ MLs embedded in hBN [115].

In order to provide an additional evidence for the variation of exciton radiative lifetime due to Purcell effect, we present Differential Reflectivity of Sample I and II in Figure 4.5.5. Panel (a) shows the data on the Sample I where the exciton radiative recombination is enhanced and panel (b) shows the data on the Sample II where the exciton radiative recombination is inhibited. Despite certain spread of the DR/R values on different points on the sample, one can see that the reflection contrast in the Sample I is systematically much larger than in the Sample II; the exciton linewidth in Sample I is also substantially larger than the one in Sample II. We stress that these reflectivity data are fully in line with the PL and TRPL measurements in Figure 4.5.1.

Note that recently three similar papers also demonstrated the changes of exciton linewidth of MoSe₂ MLs in reflectance measurements by tuning the effective cavity length using actuated mirrors or membrane [130–132]. Nevertheless, they rely on complex fitting of the reflectance spectra taking into account both homogeneous and inhomogeneous broadenings (without time-resolved measurements performed). Here, we abstain from detailed multi-parameter fit of our Differential Reflectivity data which requires also careful analysis of the light scattering and inhomogeneous broadening as well as possible effects of finite NA of the optical setup.

4.5.2 Relaxation and recombination dynamics of exciton and trion

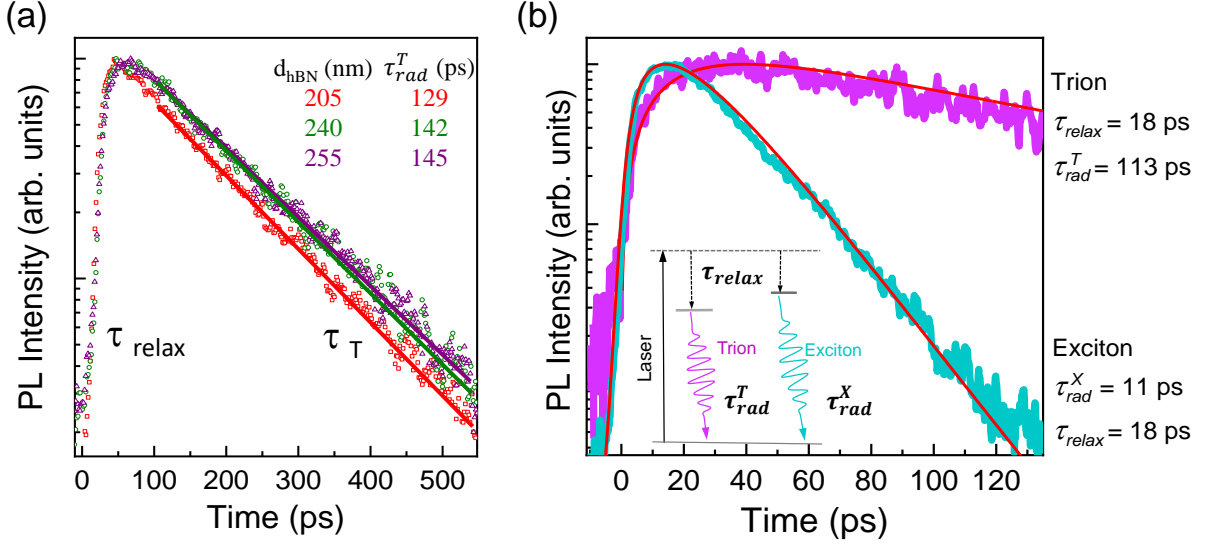


Figure 4.5.6: (a) Normalized PL intensity of the charged exciton (Trion) as a function of time for different bottom hBN layer thicknesses d_{hBN} . The full lines correspond to mono-exponential fits of the decay time τ_{rad}^T . (b) Measured (symbols) and fitted (full line) of neutral exciton (X) and trion (T) dynamics for encapsulated MoSe₂ ML with a bottom hBN layer thickness $d_{hBN} = 273.3$ nm (Sample II). Inset: schematics of the two-levels model used to describe both neutral exciton (X) and trion (T) dynamics.

The control of the radiative lifetime resulting from the hBN encapsulation is further confirmed by measuring the dynamics of the charged exciton, *i.e.* trion (labeled T). Figure 4.5.6(a) displays the normalized luminescence intensity dynamics of the trion for different hBN thicknesses in Sample III. In contrast to the neutral exciton, the variation of the bottom hBN thickness has here an impact on the trion luminescence decay time, but not on its rise-time.

As the trion's oscillator strength is smaller than the neutral exciton one [133, 134], the trion radiative lifetime of the order of ~ 100 ps is now longer than the relaxation/formation time. As a result, the PL rise time corresponding to this energy relaxation time does not vary with the cavity thickness (d_{hBN}). Here, the striking feature is that we find a variation of the trion PL decay time as a function of the hBN thickness (d_{hBN}) very similar to the variation of the neutral exciton radiative time, see Figure 4.5.1(b). Nevertheless, the amplitude of the variation is much smaller for the trion (typically 10%) whereas in the same sample the measured neutral exciton lifetime varies by more a factor two (~ 3 to 7 ps), see Figure 4.5.1(b).

The cavity effects revealed in this work make it possible to elucidate the complex dynamics of relaxation and recombination of excitons in TMD MLs [135]. In general, the exciton lifetime τ_X , measured in time-resolved luminescence dynamics, depends on both radiative and non-radiative (NR) recombination channels through Eq.(4.2) $1/\tau_X = 1/\tau_{rad}^X + 1/\tau_{nr}^X$. The radiative decay channel depends on the electro-dynamical environment characteristics due to the Purcell effect while the non-radiative one, having no electromagnetic origin is assumed unchanged. Remarkably, the strong variation of the

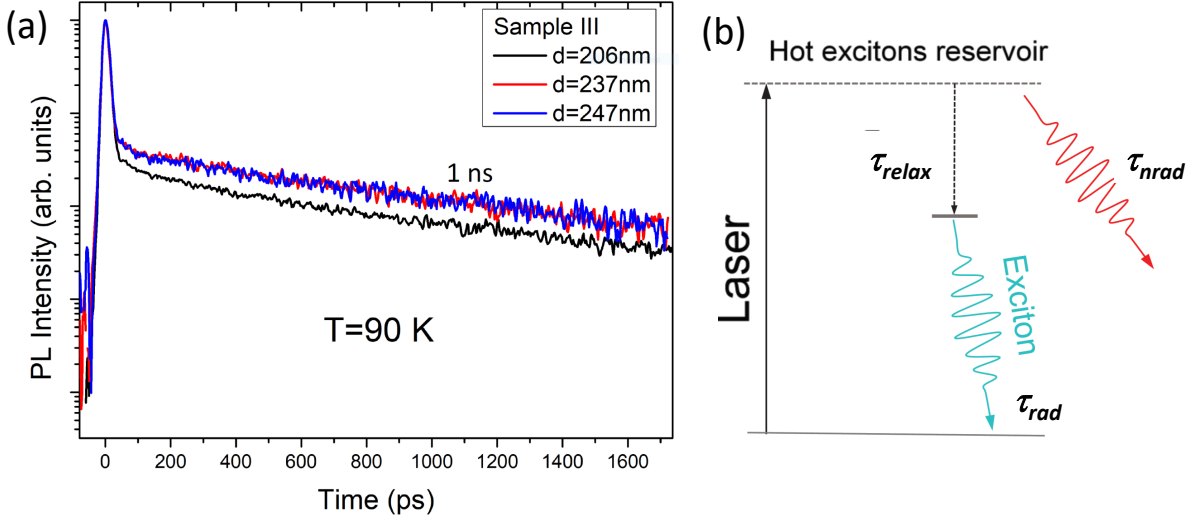


Figure 4.5.7: (a) Neutral exciton PL dynamics at $T=90$ K of sample III for three different bottom hBN thicknesses $d_{hBN} = 206, 237$ and 247 nm. At this temperature the decay time does not depend anymore on the cavity thickness. (b) Alternative scenario of the exciton dynamics which includes non-radiative processes.

neutral exciton lifetime reported in Figure 4.5.1 demonstrates that the neutral exciton lifetime at low temperatures is limited by the radiative recombination (controlled here by the Purcell effect) with negligible contribution of NR channels. However we did not observe any effect of the environment on the exciton dynamics for lattice temperatures above 80 K, see Figure 4.5.7(a). This is due to the fact that the exciton lifetime is no more controlled by purely radiative recombination [136]. The rather small modulation of the trion lifetime observed in Figure 4.5.6 reveals that it is significantly affected by NR recombination, see Figure 4.5.7(b). We can infer a NR trion recombination time of the order of $\tau_{nrad} \sim 100$ ps, i.e. competitive with the radiative one.

Excellent fits of both the neutral and trion PL dynamics can be obtained with the two-level model using the same relaxation time τ_{relax} from the photogenerated high energy states, inset of Figure 4.5.6(b). As already reported for non-encapsulated TMD MLs [126], we do not find here any evidence of electronic transfer from neutral excitons to trions in MoSe₂ ML. This result seems counterintuitive since the PL decay time of the neutral exciton coincides with the measured PL rise time of the trion, see Figure 4.5.6(b), as if the exciton lifetime would be controlled by the trion formation time. This behavior could be simply due to the fact that the same energy relaxation time τ_{relax} drives both the neutral exciton PL decay time and charged exciton PL rise time, see inset of Figure 4.5.6(b).

Another possible scenario is sketched in Figure 4.5.7(b). Our attribution of the decay time of neutral exciton to the relaxation of hot excitons assumes for simplicity the absence of non-radiative channels. Although this work demonstrates that the lifetime of an exciton in the radiative cone is dominated by its radiative recombination (tunable by cavity

effects), we cannot claim that all hot excitons necessarily relax to the light cone. Indeed, any non-radiative channel such as defects trapping, relaxation to a dark state or formation of a trion at a timescale shorter than the relaxation to the light cone would lead exactly to the same dynamics but with smaller neutral exciton PL yield. We briefly analyze this scenario where these non-radiative decay processes of excitons are considered. The occupancies of the hot exciton reservoir and of the excitons in the light cone are given in this case by the following set of rate equations:

$$\frac{dn_{hot}}{dt} = -\frac{n_{hot}}{\tau_{relax}} - \frac{n_{hot}}{\tau_{nrad}} \quad (4.7a)$$

$$\frac{dn_X}{dt} = -\frac{n_X}{\tau_{rad}} + \frac{n_{hot}}{\tau_{relax}} \quad (4.7b)$$

Here the non-radiative decay rate of excitons includes contributions of trapping to defects, trion formation as well as possible formation of dark states. For excitons within the light cone we neglect non-radiative processes since $\tau_{nrad} \gg \tau_{rad}$. The calculation shows that the exciton PL dynamics under the condition

$$\frac{1}{\tau_{decay}} = \frac{1}{\tau_{relax}} + \frac{1}{\tau_{nrad}} \ll \frac{1}{\tau_{rad}} \quad (4.8)$$

is given by the exponential law $\propto \exp(-t/\tau_{decay})$. We emphasize that if the trion formation from the hot exciton reservoir is the dominant process, then it is not surprising to observe the same rise time for the trion than the decay time for the neutral exciton.

To conclude on which scenario: sketch in Figure 4.5.6(b) or sketch in Figure 4.5.7(b) is valid in MoSe₂ ML, further experiments are required to evaluate the PL quantum yield and thus determine if τ_{decay} is governed by τ_{relax} (scenario in Figure 4.5.6(b)) or τ_{nrad} (scenario in Figure 4.5.7(b)).

Our work gives a lower bound on the relaxation time of hot excitons to the light cone ($\tau_{relax} \geq 18$ ps). We can assume that the main relaxation mechanism is through emission of phonons, while exciton-exciton and exciton-electron interaction cannot be excluded. A recent work simulated the relaxation of excitons through interactions with optical and acoustic phonons using a Monte-Carlo approach [82], see Figure 4.5.8. Interestingly, it shows that after a very fast (< 1 ps) relaxation through optical homopolar phonons, the relaxation of kinetic energy smaller than 30 meV (the lowest optical phonon energy in MoSe₂ ML) through the deformation potential interaction with acoustic phonons is much slower (step 3 in Figure 4.5.8) with a characteristic duration time of $20 \sim 30$ ps. This simulation is thus perfectly consistent with our measurement of $\tau_{relax} \sim 18$ ps.

We investigated the influence on the initial kinetic energy of hot excitons in the relaxation by varying the wavelength of the excitation laser. Results are presented in Figure 4.5.9. It clearly shows that in the range of the kinetic energy investigated (7 - 104 meV), there is no variation of the relaxation time. This is again consistent with the Monte-Carlo simulation of Figure 4.5.8, which shows that the cooling of the excitons just outside the light cone is the slowest process. From the results of Chapter 3 (bright - dark exciton splitting $\Delta = 1.5$ meV), we also cannot exclude that dark excitons act as a slow feeding reservoir for the bright states. Further studies on the bright and dark exciton formation processes as well as relaxation between the two states will be required

to determine their role on the exciton dynamics. For instance, we can consider to perform more resonant excitation measurements.

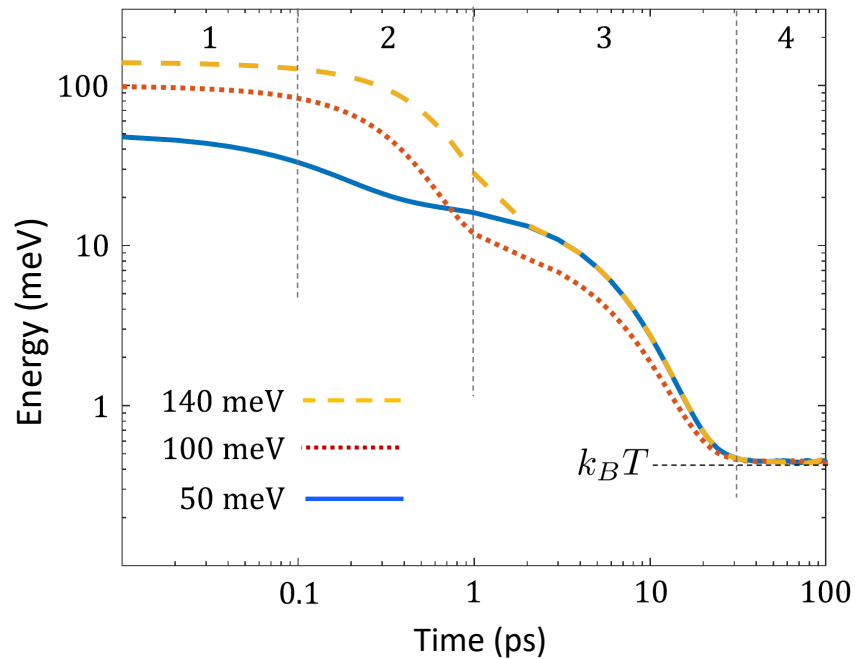


Figure 4.5.8: Monte Carlo simulation of the four-step exciton energy relaxation (separated by vertical dashed lines) in MoSe₂ ML at $T = 5$ K. Results are shown for three initial kinetic energies. The excitons reach thermal equilibrium with the lattice after ~ 30 ps. Figure is extracted from [82].

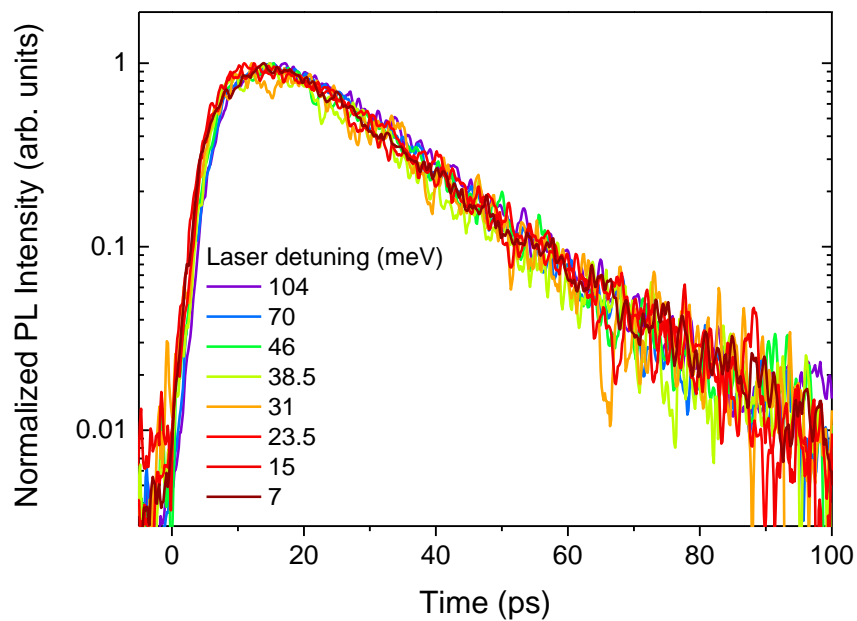


Figure 4.5.9: Normalized exciton PL intensity dynamics for different laser excitation energies, *i.e.* different energy detuning with respect to the exciton resonance measured on a sample with $d_{hBN} = 130$ nm ($\tau_{rad}^X = 6$ ps).

4.6 Conclusion

We have shown in this chapter that the linewidth of encapsulated MoSe₂ ML is not only close to the homogeneous linewidth but is dominated by the radiative linewidth. We demonstrate that we can control the radiative recombination time by one order of magnitude from $\lesssim 1$ ps up to about 10 ps by just changing the thickness of the dielectric layers in agreement with a theoretical analysis based on a transfer matrix simulation. This opens the way to engineer the exciton-photon coupling in these van der Waals heterostructures. An interesting prospect would be to deposit TMD MLs on top of epsilon-near-zero metamaterials [137] to obtain stronger enhancement of the exciton radiative decay rate. These results could be helpful to following experiments on non-linear and quantum optics and also future on-chip quantum processing applications based on coherent manipulations of photon. Finally, this tuning of the radiative lifetime helped us to understand the complex exciton/trion dynamics in this 2D material.

Chapter 5

Exciton Upconversion in Transition Metal Dichalcogenide Monolayers

As explained in the previous chapter, encapsulation in hBN results in very narrow emission/absorption exciton lines (a few meV) in TMD MLs. This allows us to evidence a very efficient PL upconversion effect which is investigated in this chapter. We have measured this effect in 4 different MLs (MoS₂, MoSe₂, WSe₂ and MoTe₂). Here we will present the detailed results on MoSe₂ and MoTe₂ ML samples. The excitation laser is tuned into resonance with the A:1s transition and surprisingly we observe emission of excited exciton states up to 200 meV above the laser energy. The optical transitions are further investigated by white light reflectivity, photoluminescence excitation and resonant Raman scattering, confirming their origin as excited excitonic states in TMD MLs. We also demonstrate bias control of the efficiency of this non-linear optical process. At the origin of upconversion we discuss in our model calculations of an exciton-exciton Auger scattering mechanism specific to TMD MLs involving an excited conduction band thus generating high energy excitons with small wave-vectors.

The chapter is organized according to the following sections:

- 5.1. Upconversion in MoTe₂ and MoSe₂ monolayers
 - 5.1.1. Upconversion probed in MoSe₂ monolayer
 - 5.1.2. Exciton states in MoTe₂ monolayer
 - 5.1.3. Energy separations between A:1s and A:2s states
- 5.2. Model on exciton upconversion
 - 5.2.1. General upconversion regimes in semiconductors
 - 5.2.2. Resonant interband Auger process
- 5.3. Conclusion

5.1 Upconversion in MoSe₂ and MoTe₂ monolayers

Optical excitation of semiconductor above the bandgap typically results in luminescence at lower energy due to energy relaxation of charge carriers and excitons. The phenomenon of PL emission at higher energy than the laser excitation is generally termed upconversion PL or anti-Stokes luminescence. The upconversion has been observed in different semiconductor structures such as InP/InAs heterojunctions, CdTe quantum wells and InAs quantum dots albeit based on different microscopic mechanisms [138–142].

Upconversion has also been reported for WSe₂ MLs [143,144]. The first upconversion result in WSe₂ MLs was realized by doubly resonant anti-stokes phonon scattering where the initial and final states are the trion and neutral exciton, respectively [143]. Then our group observed that the resonant excitation of the lowest A:1s state in hBN encapsulated WSe₂ could lead to upconversion PL of excited exciton states that also govern absorption and emission [144]. These preliminary works help us better understand the phonon-exciton interactions and more importantly offer a way to approach higher excitonic states by exciton upconversion effect. The exciton upconversion effect is also present in MoS₂ MLs [34], suggesting that it could be a general phenomenon for TMD materials.

In this section, we provide an in-depth study of exciton states in MoSe₂ and MoTe₂ MLs comparing upconversion PL with PLE spectroscopy and white light Differential Reflectivity. The fabrication of the encapsulated samples and the optical setups are described in Chapter 2. Unless explicitly specified, all the measurements have been performed at 4 K with an excitation power around 3 microwatt and with CW excitation (even for the upconversion measurements). These experiments allow detailed insight into the light-matter interaction physics of excitons and clarify the origin of upconversion signal, as the origin of excess energy needs to be identified.

5.1.1 Upconversion probed in MoSe₂ monolayers

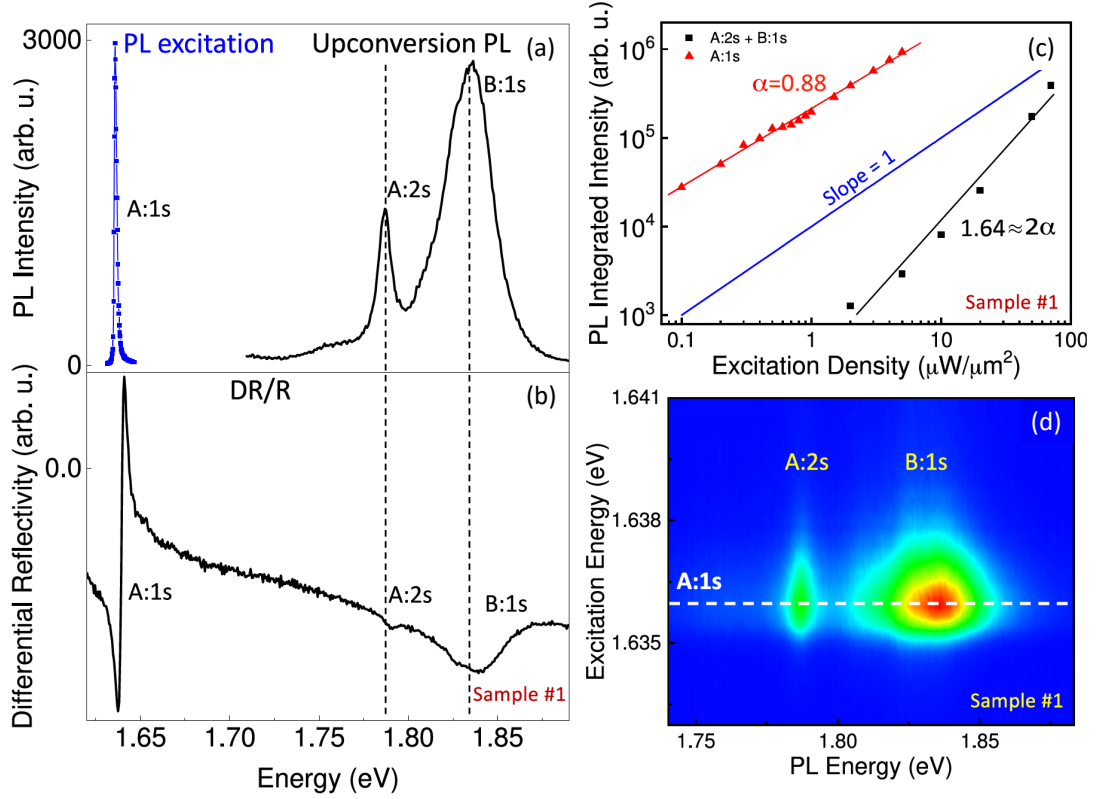


Figure 5.1.1: *Sample 1*. Control of upconversion in MoSe₂ ML at T= 4 K. (a): Scanning a CW Ti-Sapphire laser across A:1s resonance results in upconversion PL at A:2s and B:1s transitions (black curve for excitation exactly at resonance. Blue symbols give integrated upconversion intensity as a function of laser energy.) **(b)** Differential Reflectivity of the same sample spot, confirming energy positions of A:1s, A:2s and B:1s transitions. **(c)** Power dependence of upconversion shows an increase with a slope of roughly 1.64 (black symbols), compared to the standard A:1s exciton emission with a slope roughly half (0.88 – red symbols) using a HeNe laser (at 1.96 eV) for excitation. **(d)** Contour plot of upconversion PL intensity as the excitation energy sweeps across A:1s resonance (blue < 50 counts; red > 2000 counts).

MoSe₂ ML is a versatile TMD material ideally suited to explore coupling to optical cavities [145, 146], voltage control of monolayer mirrors [147, 148] and interplay between charged and neutral excitons [149]. Most of these experiments are based on the optical response of the lowest energy exciton state A:1s, but very little is known about the higher excited exciton states and energy relaxation pathways for PL emission.

The experimental results for *Sample 1* of MoSe₂ ML encapsulated in hBN [62] are summarized in Figure 5.1.1. Figure 5.1.1(b) shows clearly the A and B-exciton 1s states in Differential Reflectivity at T= 4 K [105, 150, 151]. The A:1s resonance has a narrow FWHM of the order of 2 meV [152]. We show in Figure 5.1.1(a) an upconversion result: resonant excitation at the A:1s energy with a low power, continuous wave (CW), narrow linewidth (< 1 μeV) laser results in emission of the B:1s transition at *higher* energy. The blue data points representing the integrated upconversion intensity for different laser energies has a clear maximum when the scanning laser is exactly at the A:1s resonance. In addition to B:1s, another transition appears about 150 meV above the A:1s in both

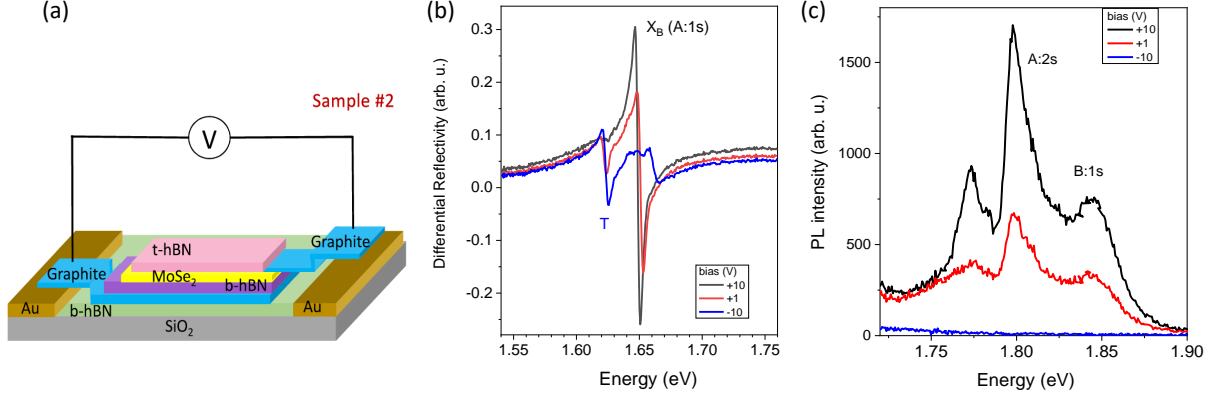


Figure 5.1.2: *Sample 2*. ML MoSe₂ charge tunable device: (a) Schematics of the device. (b) Voltage control of Differential Reflectivity. The oscillator strength of A:1s state decreases and trion resonance (T) shows up at *n*-type regime (-10 V). (c) Voltage control of upconversion. The signal is maximal in neutral regime (+ 10 V) and gets weaker as the *n*-type regime prefers trion than neutral exciton absorption shown in (b). The B:1s and A:2s emission are marked. A third emission peak of yet to be determined origin appears at lower energy.

upconversion PL and Differential Reflectivity. We tentatively assign it to the excited A-exciton, A:2s state. For samples directly exfoliated onto SiO₂ the excited A-exciton states were not directly accessible due to their overlap with the B-exciton 1s state. A fingerprint of the A:2p state was reported in two-photon PL excitation (PLE) experiments [151], where the B:1s state absorption is strongly suppressed [153].

We further investigate the origin of upconversion PL in MoSe₂ ML. We compare the evolution of the standard and upconversion PL intensity as a function of laser power, in Figure 5.1.1(c). For *Sample 1*, the slope of the upconversion intensity versus laser power (1.64) integrated over the A:2s and B:1s emissions is roughly two times the standard PL (0.88) slope, consistent with a two-photon (two exciton) non-linear optical process. We note that the exact power dependence determination for upconversion PL depends slightly on the spectral range used for signal integration. For example, the slope for a narrow spectral range at the A:2s (B:1s) resonance is roughly 2 (1.8). Figure 5.1.1(d) shows the upconversion emission as the laser is scanned across A:1s resonance. It is only detectable over a 2 meV range of scanning laser energy and maximized at A:1s resonance. This indicates upconversion is a resonant process, as observed for WSe₂ MLs [144].

This conclusion gets additional support from upconversion experiments on *Sample 2* corresponding to a charge tunable device in Figure 5.1.2(a). At a bias of +10 V, the excitation laser is tuned into resonance with the neutral A:1s state. The upconversion PL gradually decrease with bias voltage and is not detectable any more at -10 V, in Figure 5.1.2(c). This is because as the applied voltage is lowered, electrons are added to the monolayer, decreasing oscillator strength of A:1s exciton and resulting in a gradually dominant trion absorption (T) [147, 148, 150], as shown in the reflectivity in Figure 5.1.2(b). These experiments confirm that upconversion PL has its origin in resonant A:1s exciton generation and is electrically controllable. Note that for a quantitative analysis of the bias tuning of the upconversion efficiency, the slight shift of the central A:1s resonance energy with bias needs to be taken into account. However, this energy shift for A:1s in our sample is considerably smaller than the transition linewidth.

5.1.2 Exciton states in MoTe₂ monolayer

MoTe₂ is a very interesting layered material in the TMD family [154–156] with unique properties. First it provides interesting opportunity to switch between semiconducting 2H and metallic phases by tuning strain or carrier concentration [157, 158]. This allows working towards devices based on bias controlled phase changes in MoTe₂ ML [159, 160]. Secondly, while early studies of 2H–MoTe₂ flakes exfoliated on SiO₂ have identified monolayers as direct semiconductors [161, 162] the nature of bilayer (BL)’s gap is still under discussion [106, 163]. In practice the difference between mono- and bilayer can be revealed in Raman experiments, see Figure 5.1.4(a). MoTe₂ MLs have an optical gap of 1.17 eV at T = ~ 4 K corresponding to emission wavelength at 1050 nm. Therefore, its alloying with other TMD MLs allows in principle to cover a full spectral range from 630 to 1050 nm for optoelectronics applications. Since it also has strong optical absorption for excited exciton states above excitonic bandgap (A:1s) [15, 20, 27, 28, 30–32, 164], better knowledge of the excited exciton spectrum is needed. This allows in principle to estimate the exciton binding energy by comparing with model calculations of exciton states in a screened 2D potential [20, 34, 165, 166].

Here we show the striking impact of hBN encapsulation on the optical properties of MoTe₂ ML. The PL spectrum in Figure 5.1.3(b) shows very narrow emission lines with a FWHM of 3 meV for the A:1s neutral exciton state at 1.17 eV, approaching the optical quality reported for hBN encapsulated MoS₂ and WSe₂ MLs [75, 144, 167–171]. The typical exciton linewidth measured in non-encapsulated MoTe₂ ML is larger than 10 meV [106]. Figure 5.1.3(a) confirms the high sample quality in reflectivity experiments where this transition locates basically at the same energy as in PL, indicating negligible exciton localization. In Differential Reflectivity we see also a broader transition about 250 meV above the A:1s that we ascribe to the B:1s state, following comparison with the data from the literature [161, 162, 172]. We also observe in reflectivity a transition 120 meV above the A:1s state, not reported previously, which we ascribe to the A:2s state. Strikingly, when exciting with a laser energy of 1.96 eV we also see hot PL emission of this A:2s transition in Figure 5.1.3(b).

To further investigate the nature of these excited exciton states, we carry out PLE experiments. We monitor the PL emission of A:1s state as in Figure 5.1.3(b) as a function of the laser excitation power. PLE probes absorption of higher lying electronic transitions and their subsequent relaxation to A:1s state, usually by emitting phonons. We observe in our experiments clear indications of both processes: absorption by excited exciton states and phonon assisted energy relaxation. In Figure 5.1.3(c), we see clear resonances in PLE at the same energies as the reflectivity spectrum for A:2s and B:1s states. The PL emission is enhanced by orders of magnitude when laser excitation resonates with these excited exciton states, indicating efficient absorption and energy relaxation.

Phonon assisted relaxation and associated resonant and non-resonant Raman scattering in MoTe₂ ML are shown in Figure 5.1.4. Raman scattering can be used to distinguish MoTe₂ ML from BL that also shows clear and narrow PL emission. In Figure 5.1.4(a) we compare Raman spectra of ML and BL. The absence of low-energy A_{1g} peak helps us to identify MoTe₂ ML [173, 174]. Figure 5.1.4(a) shows essentially non-resonant Raman scattering *i.e.* neither the laser energy nor the emission after phonon scattering is resonant with a particular electronic state. This is different in Figure 5.1.4(b): Here we tune the laser to an excess energy about 20 meV above the A:1s resonance. We see a

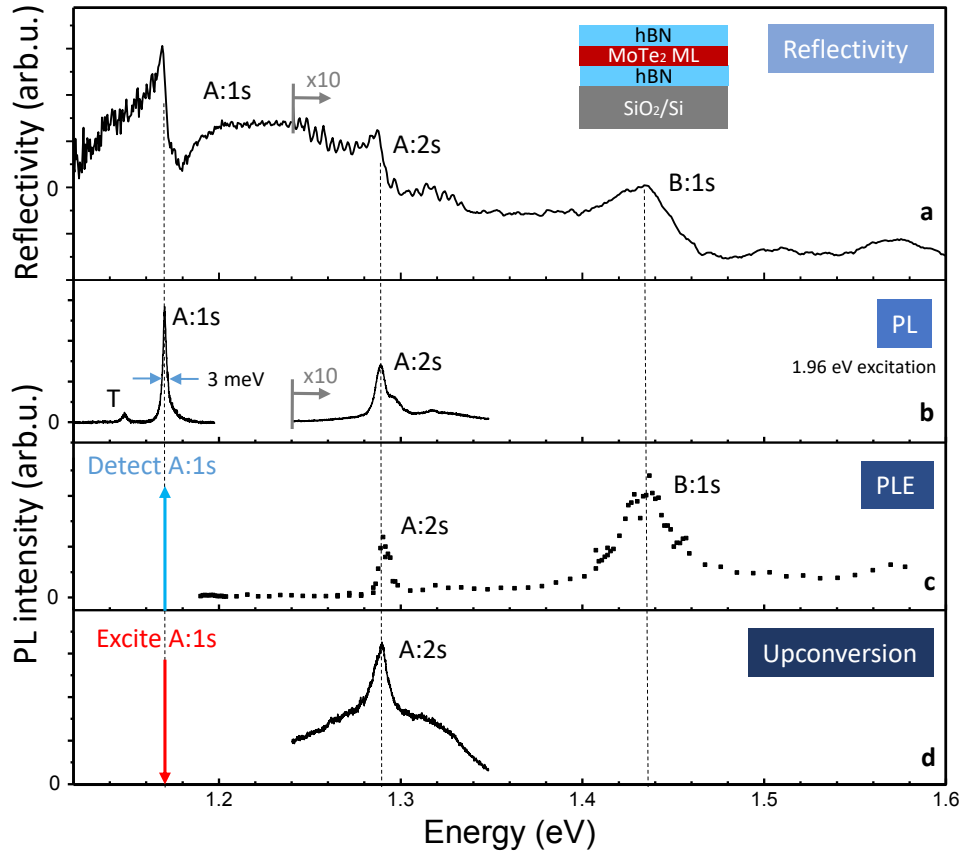


Figure 5.1.3: Exciton spectroscopy in MoTe₂ monolayer encapsulated in hBN. T= 4 K. (a) Differential reflectivity spectrum, the energy positions of the exciton transitions A:1s, A:2s and B:1s are marked. (b) Excitation with a HeNe Laser results in hot PL of the A:2s and PL for the A:1s state. The low energy peak labeled T might be related to the trion or phonon replica. (c) Photoluminescence excitation measurements detecting the emission from the A:1s exciton. Peaks related to the resonant excitation of the A:2s and B:1s are marked. (d) Upconversion PL, the laser tuned into resonance with the A:1s state results in emission about 120 meV higher energy, same as Figure 5.1.1(a).

spectrally sharper feature (shaded blue) superimposed on the PL (shaded orange) shifts with excitation laser energy. This peak corresponds to Raman scattering with the A'_1 phonon, which is particularly efficient with the final state to be a real electronic state after scattering *i.e.* single-resonant Raman scattering experiments [90,168,173,175–177].

As the laser energy is scanned across the A:2s state, we see that the PL of A:1s exciton is enhanced, see intensity plotted in Figure 5.1.4(c) as a function of laser energy. In addition, we observe a Raman feature crossing the PL line, exactly 120 meV below the respective laser energy. When the laser is at the A:2s energy, the Raman process is double resonant [173,176] as the initial state (A:2s) and final state (A:1s) are real electronic states. In Figure 5.1.4(c) we report this double resonant Raman experiments [176,178]. This has already been observed in our group in WSe₂ ML on SiO₂ [176]. Please note that very different electronic states and phonons are discussed in the double resonant Raman experiments in Ref. [173]. Detailed Raman studies of MoTe₂ are also reported for mono- and multilayers in Ref. [156]. In experiments in hBN encapsulated WSe₂ ML samples, similar experiments have been interpreted as being due to phonon related processes only [167]. This interpretation seems unlikely in view of follow-up studies of

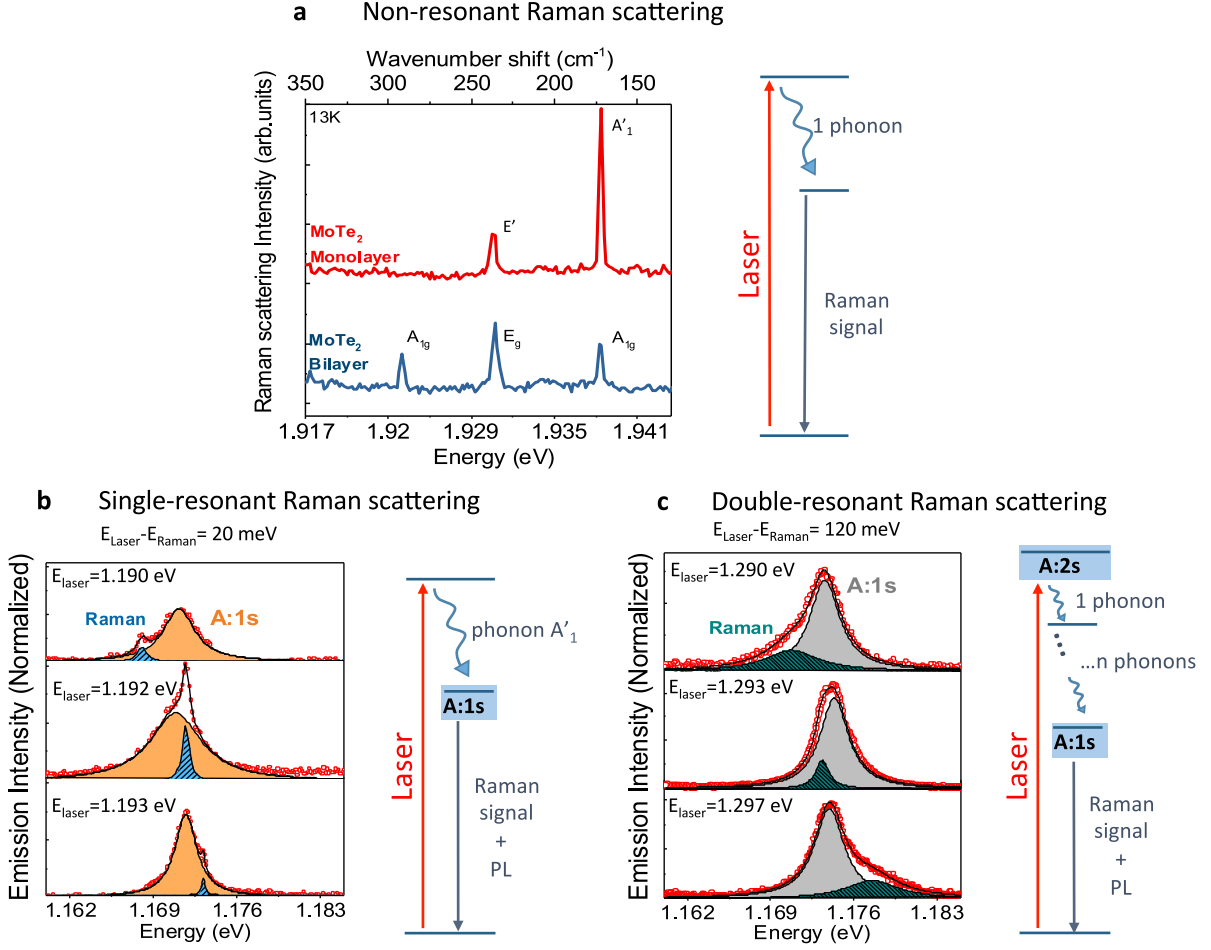


Figure 5.1.4: Raman spectroscopy in ML MoTe₂. $T = 4 \text{ K}$. (a) Non-resonant Raman scattering using a HeNe laser. (b) Single resonant Raman scattering as the excitation laser energy is one phonon energy A'_1 above the A:1s state. (c) Double resonant Raman experiments as a phonon multiple ensures efficient relaxation from the optically excited A:2s state to the emitting A:1s state.

WSe₂ ML in magnetic fields which clearly showed that the excited state is an excitonic transition and not just phonon replica [37]. For the case of MoTe₂ ML we have a strong case for the transition at 120 meV above the A:1s attributed to a real electronic transition, which is confirmed in Figure 5.1.3 by four complementary spectroscopy techniques and in Figure 5.1.4(c) by double resonant Raman scattering. Finally, note that this attribution was recently unambiguously confirmed in high magnetic field experiments [99].

As we already wrote, upconversion PL is a powerful technique for investigating exciton states. Here a CW laser excites the MoTe₂ ML at the A:1s resonance and emission at higher energies is monitored. In Figure 5.1.3(d) we indeed observe emission 120 meV above the laser energy which is resonant with the A:1s state. This emission is exactly at the same energy as the transition ascribed to the A:2s state with the three other spectroscopy techniques: Differential Reflectivity, hot PL and PLE all compared in Figure 5.1.3. We note that the upconversion PL of MoTe₂ ML consists of the A:2s emission superimposed on a broad background. The emission of this global upconversion signal increases linearly with laser power, and not nearly quadratically as expected and demonstrated in WSe₂ ML [144] and MoSe₂ (see Figure 5.1.1).

5.1.3 Energy separations between A:1s and A:2s states

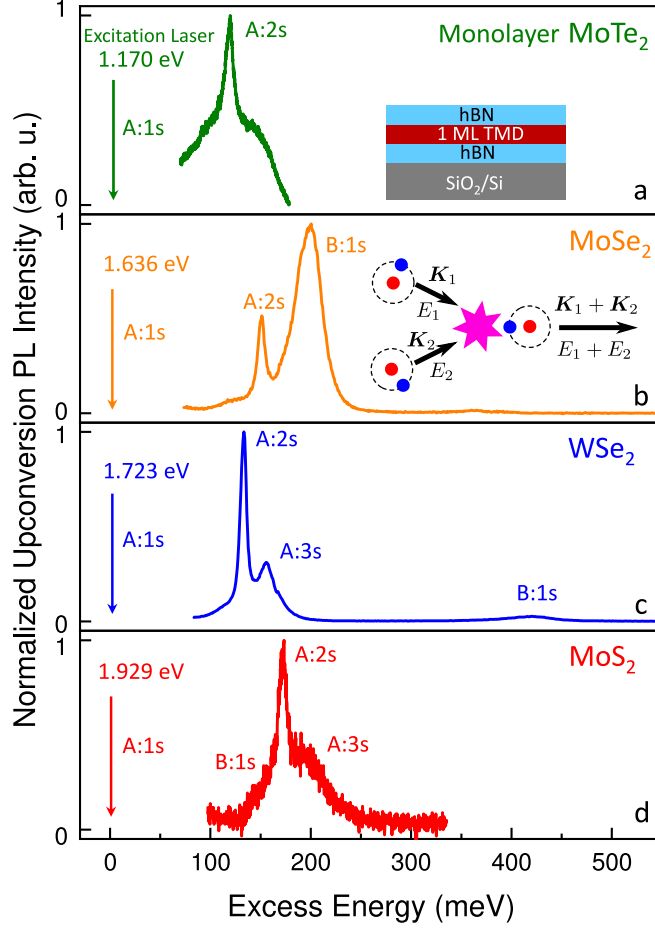


Figure 5.1.5: (a-d) Upconversion measured in TMD MLs of MoTe₂, MoSe₂, WSe₂ and MoS₂. Laser excite resonantly A:1s states. Inset in (b) is the sketch of Coulomb scattering of two excitons. (c) and (d) are data extracted from Refs. [34, 144]

The upconversion effect is also an efficient tool to measure the energy of the exciton excited states. It is a general effect that we have evidenced in the four TMD MLs : MoS₂, MoSe₂, MoTe₂ and WSe₂ as shown in Figure 5.1.5. The values of energy separation between the A:1s and A:2s states:

$$\Delta_{12} \equiv E_{A:2s} - E_{A:1s} \quad (5.1)$$

obtained by the upconversion spectroscopy and other optical techniques in our experiments are summarized in Table. 5.1.1 together with other excitonic parameters calculated and taken from the literature. As an important result of our measurements, we find that the values of Δ_{12} in hBN encapsulated MoSe₂ and MoTe₂ are comparable to the ones in WSe₂ [37, 38, 178]. The fact that the effective masses of electrons and holes in MoSe₂ and MoTe₂ are calculated to be about a factor of two larger than those in WSe₂ and WS₂ [179] (see also Table. 5.1.1 for the summary of values) would imply in principle larger values of Δ_{12} in Mo-based monolayers than measured here. However, in two-dimensional semiconductors the electron-hole interaction law strongly deviates from the $1/r$ dependence due to dielectric screening effects [28, 165, 166] and can be described by the Rytova-Keldysh potential that is shown in Eq. (1.2).

Accounting for this effect, we calculate the energy separation between the ground and excited excitonic states by applying a simple variational approach. The wavefunctions of the ground and first excited states are sought in the two-dimensional hydrogenic form

$$\Phi_{1s}(r) = \sqrt{\frac{2}{\pi a^2}} e^{-r/a}, \quad (5.2a)$$

$$\Phi_{2s}(r) = \sqrt{\frac{2}{27\pi a^2}} \left(1 - \frac{2r}{3a}\right) e^{-r/3a}, \quad (5.2b)$$

with the only trial parameter a which is the same for both functions. Such an approach has an advantage of automatically providing orthogonal ground and excited states at a cost of simplicity. To test the calculation we reproduced within the error of $\leq 2\%$ the results of Ref. [34], where more sophisticated numerical approaches were used, for A: 1s and A: 2s excitons in MoS₂ ML with the same set of parameters.

We obtain good agreement for the A:1s-A:2s separation by means of variational approach, see Table. 5.1.1. Here the only free parameter is r_0 , in reasonable agreement with literature data. Note that both measured and calculated separations are in agreement with previous experimental and theoretical results available for WSe₂ and MoTe₂ MLs, see [34, 37, 38]. For a more detailed understanding of the energy positions of the excited states and more sophisticated modelling may require also going beyond the simple variational scheme, application of various extensions of the screened potential [38, 165, 166] and accounting for the bands non-parabolicity [180]. Also, the exact values of the effective mass values are still discussed in the literature, with interesting new insights from transport measurements in gated samples [100, 178, 181], which provide larger values of effective masses, possibly renormalized by the carrier-carrier interactions.

	MoS ₂	MoSe ₂	WSe ₂	MoTe ₂
$\Delta_{12}^{experiment}$ (meV)	175	150	130	120
m_e/m_0	0.45	0.53	0.34	0.57
m_h/m_0	0.54	0.6	0.36	0.64
μ/m_0	0.25	0.28	0.17	0.3
r_0 (Å)	6.67	10	8.2	14.4
ρ_0 (Å)	30	45	37	65
E_B^{theory} (meV)	214	186	162	156
Δ_{12}^{theory} (meV)	174	148	133	121

Table 5.1.1: Exciton parameters obtained in experiments and calculations. The values of the electron, m_e , and hole, m_h , effective masses are taken from Ref. [179] (averaged over different calculation methods and subbands), m_0 is the free electron mass, $\mu = m_e m_h / (m_e + m_h)$ is the reduced mass of the electron-hole pair; effective dielectric constant of surrounding was chosen as in Ref. [34] $\varepsilon = 4.5$, the value of the r_0 was chosen to obtain similar to experimental values of Δ_{12} , Eq. (5.1).

5.2 Model on exciton upconversion

In the subsection 5.2.1, we briefly recall three general mechanisms usually considered to explain upconversion emission in semiconductor nanostructures. In the subsection 5.2.2, we provide a theoretical model of interband Auger type exciton-exciton scattering developed by Mikhail Glazov and Leonid Golub from Ioffe Institute in Saint Petersburg. It suggests that the upconversion process could be very efficient in TMD MLs as compared to other semiconductor nano-structures. Intraband Auger process and two step absorption that are orders of magnitude smaller effects are also introduced to compare with interband resonant Auger scattering, see Appendix A.1 and A.2.

5.2.1 General upconversion regimes in semiconductors

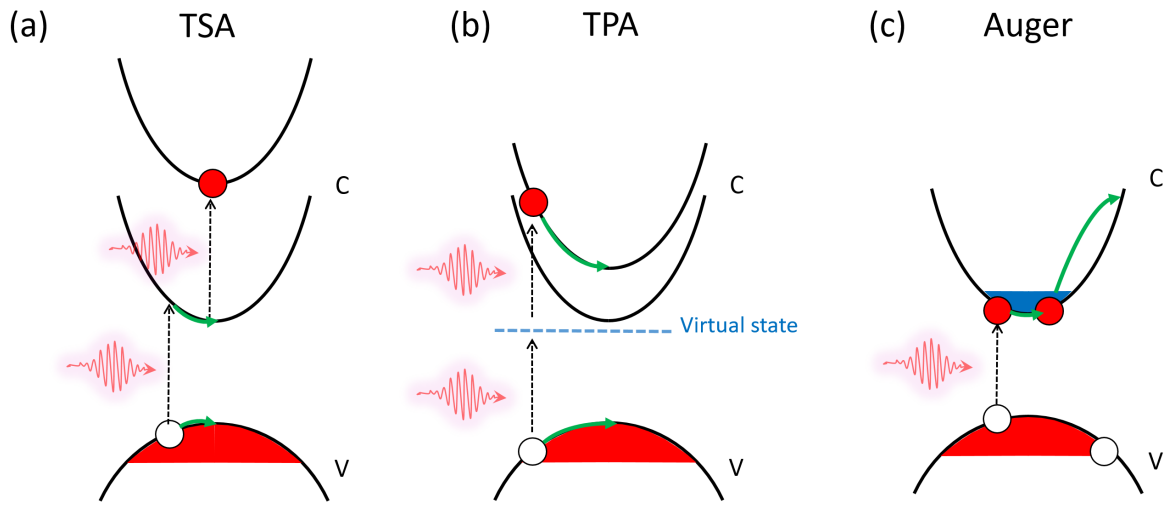


Figure 5.2.1: Generation of high energy carriers in a direct bandgap semiconductor, neglecting the spin degree of freedom and non-parabolicity. The electron and hole are depicted in filled red and hollow circles. The shading areas in red and blue represent filled level. **(a)** two step absorption (TSA) process with a real intermediate state. **(b)** two photon absorption (TPA) with a virtual intermediate state. **(c)** Auger scattering: an electron-hole pair non-radiatively recombine; the energy and wavevector conservation is ensured thanks to the scattering of an electron to higher energy state.

Upconversion normally involves another quanta like phonon, photon, or even residual carriers. The most straightforward mechanism would be thermal activation by absorbing phonons [140, 143]. However, the thermal energy $k_B T \sim 0.34$ meV at a cryogenic temperature of 4 K is too small to explain the effect we observed in TMD MLs where upconverted emission can occur hundreds of meV above the excitation, see Figure 5.1.5.

Let us first recall the characteristics of other two mechanisms in semiconductor nanostructures which involve twice photon “absorption” through an intermediate level: two step absorption (TSA) and two photon absorption (TPA), depicted in Figure 5.2.1(a,b). TSA has real intermediate levels which can reabsorb photons when they have sufficiently long enough recombination lifetime, Figure 5.2.1 (a). These levels could be normal excitonic, localized or defect states. Note that the excitation and upconversion do not necessarily happen in the same material. For instance, exciton generated in quantum dots (QD) and quantum well (QW) could lead to upconversion in their surrounding barriers [139, 141].

In TPA, the intermediate state is virtual, as shown in Figure 5.2.1(b), similar to the general Raman scattering introduced in Figure 5.1.4(a). Therefore, TPA could be regarded as a very fast coherent absorption of two photons. The intensity of the upconversion emissions in both TSA and TPA are proportional to the product of the amount of upconverted excitons and reabsorbed photons, resulting in a quadratic power dependence of on excitation, $I_{up} \propto I^2$.

We know that the upconversion of ground exciton state A:1s exciton to excited states of A:2s, 3s and B:1s... is a general phenomenon in hBN encapsulated TMD MLs, see Figure 5.1.5. A first discussion of possible origin of the upconversion signal in WSe₂ ML can be found [144]. The main ingredients are: the absorption of multiple $m \geq 2$ photons and consequent energy relaxation of photogenerated electron-hole pairs, *i.e.* the TSA process. The TPA process can not be responsible for the strong upconversion emission we evidenced in TMD MLs since we showed that the effect is strongly enhanced when the photon energy is resonant with the real excitonic transition energy.

Auger recombinations depicted in Figure 5.2.1(c) can also yield an upconverted emission, as evidenced in many semiconductor structures [138]. Typical Auger process usually involves three particles, e-e-h or e-h-h in heavily doped regimes. In a n-type regime for instance, an electron-hole pair could recombine non-radiatively and the corresponding energy is transferred to an extra electron which recombines with minority carriers, *i.e.* holes, to give out upconverted PL. The Auger recombination could be of excitonic origin in TMD MLs. In Section 5.2.2, we introduce the resonant interband excition Auger process to explain our experimental results and also compare it with intraband Auger and TSA processes.

5.2.2 Resonant interband Auger process

As shown in the previous sections, the effect vanishes for non-resonant excitation or if the oscillator strength of the A:1s exciton is suppressed by the gate-doping in charge tunable samples. Further insight into the exact mechanism is provided by the laser power dependence of the upconversion PL intensity I_{up} on the incident radiation intensity I . The data presented in Figure 5.1.1(c) for MoSe₂ sample show that this dependence is superlinear and roughly scales as $I_{up} \propto I^{2\alpha}$, where $0.5 < \alpha < 1$ (see also data from our group published in Figure 2(b) of Ref. [144] on WSe₂). Importantly, the emission from the A: 1s state under quasi-resonant excitation with the same power scales as $I_{A:1s} \propto I^\alpha$, *i.e.*, with the twice smaller power. Since the emission intensity is proportional to the occupancy of the corresponding excitonic states the experimental results demonstrate that the formation of the upconversion signal requires two excitons in the ground state.

Hence, the most plausible scenario is related to the exciton-exciton interaction, *i.e.*, the Auger process, where one of the excitons is annihilated while the second exciton acquires large extra energy [182, 183], as depicted in Figure 5.2.2. Subsequently, this exciton relaxes toward the radiative states (particularly A:2s and B:1s) and hot PL from these states is observed since the radiative recombination time is competitive (*i.e.* short enough) compared to the energy relaxation time.

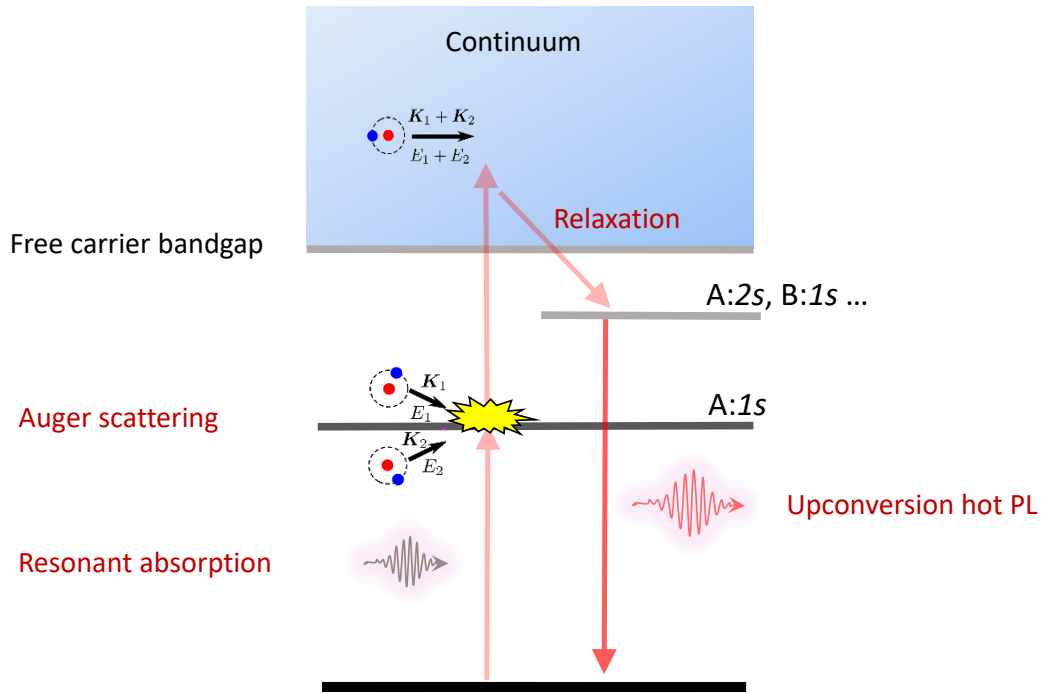


Figure 5.2.2: Sketch of exciton upconversion – exciton picture. The resonant absorption of A:1s exciton state generates a large population. During Auger scattering (yellow clash), one A:1s exciton recombine non-radiatively and transfer its energy to the other A:1s exciton that is then upconverted in the continuum. The upconverted excitons relax to the excited exciton states of A:2s and B:1s, etc and recombine radiatively to give out upconversion PL.

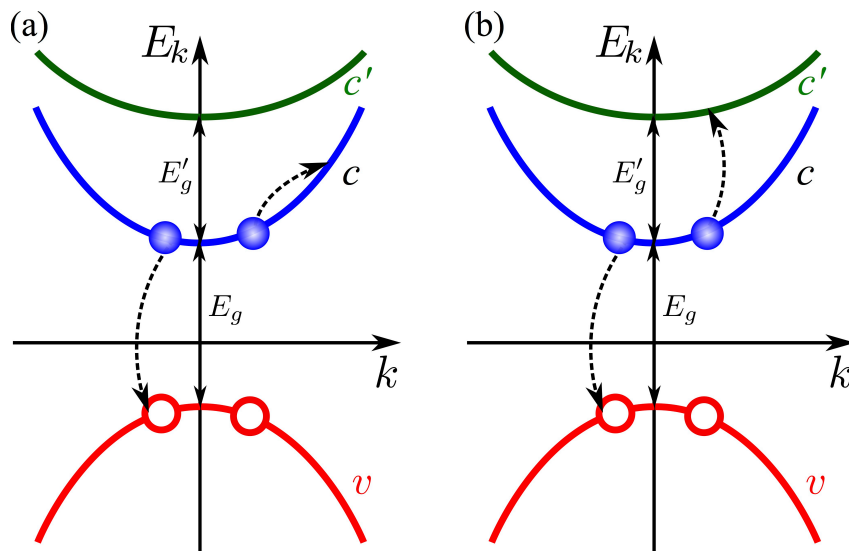


Figure 5.2.3: Model of exciton upconversion – single particle picture. Filled circles denote electrons; open circled denote unoccupied states in the valence band. Dashed arrows show real electronic transitions. (a) Intraband process enabled by excitonic effects. The resulting high energy exciton involves carriers in the bands c and v , the final momentum $\mathbf{K}_f = \mathbf{K}_1 + \mathbf{K}_2$ is large. (b) Resonant Auger process resulting in high energy, low wavevector \mathbf{K}_f excitons involving the excited conduction band c' .

Energy (eV)	MoS ₂	MoSe ₂	WSe ₂	MoTe ₂
E_g	1.8	1.6	1.7	1.7
E'_g	1.1 ... 1.2	1	1.4	1.3

Table 5.2.1: Band gap energies. Data from DFT calculations summarized in Ref. [192] for S and Se-based MLs and from Ref. [106] for MoTe₂ MLs. The direct comparison of the values with experimental data in Figure 5.1.5 is not possible due to different levels of DFT approximations used.

At first glance, this Auger-like exciton-exciton annihilation seems to be quite weak because in order to satisfy the energy and momentum conservation laws, the initial kinetic energy of the involved particles should be very large [184]. As we show here this effect is very efficient in TMD MLs due to (i) strong Coulomb interaction, which makes it possible to relax the single-electron momentum conservation [185, 186] and (ii) the possibility of a resonant processes involving exciton transfer to an excited energy band [144]. In other words, we try to include the particular energy spacing between different conduction bands in the theory of this four particle interaction.

The detailed exciton-exciton Auger processes in a single particle picture is depicted in Figure 5.2.3. We consider three bands, c, v, c' with two excited electron-hole pairs (excitons) with an electron occupying the lowest conduction band c and an empty state in the valence band v . Panel (a) shows an example of a standard Auger process which is possible in any semiconductor: Due to the Coulomb interaction one electron recombines with a hole, while another carrier is transferred to a highly excited state. Panel (b) illustrate a very different process, which is possible in the studied TMD MLs due to their specific band structure: it turns out that there is an excited conduction band (denoted as c') whose distance to the conduction band, E'_g , approximately satisfies the condition of

$$E'_g \lesssim E_g - E_B \quad (5.3)$$

where $E_B \approx 0.3 \dots 0.5$ eV [28] is the exciton binding energy for measurements directly on SiO₂ in Table. 5.2.1 and lower values for E_B of the order of 200 meV in hBN encapsulated samples, see Table. 5.1.1 and Ref. [37]. Thus the electron can be promoted to the c' band in the course of exciton-exciton annihilation with relatively small wavevector rather than be scattered to a large wavevector state within the same band. Note that this high energy band and its role to explain upconverted PL and Second Harmonic Generation (SHG) in the UV range was recently evidenced [187] after our work.

Here for simplicity we disregard the spin degree of freedom of charge carriers, assuming that the spin is conserved in the course of exciton-exciton interaction. Furthermore, we focus on the states in the vicinity of one of the band extrema (K_+ or K_- valley) and disregard here the processes involving intervalley transfer of electron-hole pair studied in Ref. [188]. The Coulomb interaction between the electrons can result in the process shown in Figure 5.2.3(b) where one pair recombines while the remaining electron occurs in the c' band. So, one $c'v$ pair is present in the end. Since in this process both electrons change their quantum states the resonant Auger scattering is due to the electron-electron interaction only, while, e.g., electron-hole interaction does not play a role, in contrast to

the exciton-exciton scattering where all charge carriers remain in the same bands [189, 190].

In the free-particle picture, we have initially two electrons in the c band which are in the c' - and v -bands after the Coulomb scattering. The two-electron wavefunctions of the considered system in the initial and final states can be presented as

$$\begin{aligned} |i\rangle &= \frac{1}{\sqrt{2}}[\Psi_{c\mathbf{k}_c}(\mathbf{r}_1)\Psi_{c\tilde{\mathbf{k}}_c}(\mathbf{r}_2) - \Psi_{c\mathbf{k}_c}(\mathbf{r}_2)\Psi_{c\tilde{\mathbf{k}}_c}(\mathbf{r}_1)] \\ |f\rangle &= \frac{1}{\sqrt{2}}[\Psi_{v\mathbf{k}_v}(\mathbf{r}_1)\Psi_{c'\mathbf{k}_{c'}}(\mathbf{r}_2) - \Psi_{v\mathbf{k}_v}(\mathbf{r}_2)\Psi_{c'\mathbf{k}_{c'}}(\mathbf{r}_1)] \end{aligned} \quad (5.4)$$

Here $\tilde{\mathbf{k}}_c, \tilde{\mathbf{k}}_v$ are the electron and unoccupied state wavevectors in one of the excitons and $\mathbf{k}_c, \mathbf{k}_v$ are the electron and unoccupied state wavevectors in another exciton. The wavefunction in each band $n = c, c', v$ is a product of Bloch amplitude and plane wave:

$$\Psi_{n\mathbf{k}}(\mathbf{r}) = e^{i\mathbf{k}\cdot\mathbf{r}} u_{n\mathbf{k}}(\mathbf{r}) \quad (5.5)$$

the normalization area is set to unity. In $\mathbf{k} \cdot \mathbf{p}$ model, the Bloch amplitudes are:

$$u_{c\mathbf{k}_c} = u_c + \frac{\hbar}{m_0} \frac{\mathbf{k}_c \cdot \mathbf{p}_{vc}}{E_c - E_v} u_v + \frac{\hbar}{m_0} \frac{\mathbf{k}_c \cdot \mathbf{p}_{c'c}}{E_c - E_{c'}} u_{c'} \quad (5.6)$$

$$u_{c'\mathbf{k}_{c'}} = u_{c'} + \frac{\hbar}{m_0} \frac{\mathbf{k}_{c'} \cdot \mathbf{p}_{vc'}}{E_{c'} - E_v} u_v + \frac{\hbar}{m_0} \frac{\mathbf{k}_{c'} \cdot \mathbf{p}_{cc'}}{E_{c'} - E_c} u_c \quad (5.7)$$

$$u_{v\mathbf{k}_v} = u_v + \frac{\hbar}{m_0} \frac{\mathbf{k}_v \cdot \mathbf{p}_{cv}}{E_v - E_c} u_c + \frac{\hbar}{m_0} \frac{\mathbf{k}_v \cdot \mathbf{p}_{c'v}}{E_v - E_{c'}} u_{c'} \quad (5.8)$$

where u_n denotes the Bloch amplitude at the extremum point, m_0 is the free electron mass and $\mathbf{p}_{nn'}$ are the momentum matrix elements between the states in the bands n and n' ($n, n' = c, c', v$).

The wavefunctions $|i\rangle, |f\rangle$ in Eq. (5.4) are antisymmetrized with respect to the permutations of electrons. It gives rise to the *direct* and *exchange* contributions. The matrix element of the direct interaction, where the electron from the state with the wavevector \mathbf{k}_c recombines with the hole from same exciton and transfers to the state \mathbf{k}_v , can be conveniently presented in the form

$$M_{dir} = \langle u_{v\mathbf{k}_v} | u_{c\mathbf{k}_c} \rangle \langle u_{c'\mathbf{k}_{c'}} | u_{c\tilde{\mathbf{k}}_c} \rangle V_C(K_1) \delta_{\mathbf{K}_1, \mathbf{k}_c - \mathbf{k}_v} \delta_{\mathbf{K}_1, \mathbf{k}_{c'} - \tilde{\mathbf{k}}_c} \quad (5.9)$$

where $\mathbf{K}_1 = \mathbf{k}_c - \mathbf{k}_v$ is the exciton center of mass momentum. Note that the hole state corresponds to the time-reversed counterpart of the unoccupied state.

$$V_C(q) = \frac{2\pi e^2}{\varkappa q(1 + qr_0)} \quad (5.10)$$

is the 2D Fourier image of the Coulomb potential with \varkappa being the background average constant of the surrounding structure and r_0 being the dielectric screening parameter [165, 166, 191]. Note that this parameter should be taken in the high-frequency limit because the energy transferred in the course of exciton-exciton interaction is on the order of the band gap E_g . Taking into account that

$$\frac{\hbar}{m_0} \mathbf{k} \cdot \mathbf{p}_{vc} = \gamma_3^* k_+, \quad \frac{\hbar}{m_0} \mathbf{k} \cdot \mathbf{p}_{c'c} = \gamma_6 k_- \quad (5.11)$$

where γ_3 and γ_6 are the band structure parameters introduced in Refs. [179, 192] and $k_{\pm} = k_x \pm ik_y$, we obtain:

$$\langle u_{vk_v} | u_{ck_c} \rangle = \frac{\gamma_3^* K_+}{E_c - E_v}, \quad \langle u_{c'k_{c'}} | u_{c\tilde{k}_c} \rangle = \frac{\gamma_6 K_-}{E_{c'} - E_c} \quad (5.12)$$

Finally, the direct interaction matrix element takes a simple form

$$M_1(K_1) \equiv V_C(K_1) \frac{\gamma_3^* \gamma_6 K_1^2}{E_g E_g'} \delta_{\mathbf{K}_1, \mathbf{k}_c - \mathbf{k}_v} \delta_{\mathbf{K}_1, \mathbf{k}_{c'} - \tilde{\mathbf{k}}_c} \quad (5.13)$$

With account for the excitonic effect Eq. (5.13) should be averaged over the exciton wavefunction [153, 188, 193]. Furthermore, we need to take into account that in the initial state there are two unoccupied states in the valence band. As a result, we have ($K_1, K_2 \ll a_B^{-1}$)

$$M_{dir}(\mathbf{K}_1, \mathbf{K}_2, \mathbf{K}_f, \mathbf{n}) = \delta_{\nu, 1s} \delta_{\mathbf{K}_f, \mathbf{K}_1 + \mathbf{K}_2} \Phi_{1s}(0) \times \frac{1}{2} [V_C(K_1) K_1^2 + V_C(K_2) K_2^2] \frac{\gamma_3^* \gamma_6}{E_g E_g'} \quad (5.14)$$

We recall that $\mathbf{K}_1, \mathbf{K}_2$ are the wavevectors of excitons in initial state, $\mathbf{K}_f = \mathbf{K}_1 + \mathbf{K}_2$ is the wavevector of exciton in the final state, the subscript ν enumerates the relative motion states of the remaining electron-hole pair. In derivation of Eq. (5.14) we neglected the difference of electron effective masses in c and c' bands and assumed that initially both excitons occupy $1s$ state, $\Phi_{1s}(\rho)$ is the envelope function of the relative motion. Correspondingly, the final state relative motion envelope function remains the same.

The typical center of mass wavevectors involved in exciton-exciton scattering are on the order of thermal wavevector $K_T = \sqrt{2Mk_B T / \hbar^2}$ and are much smaller than the screening wavevector r_0^{-1} , therefore the direct exciton-exciton scattering matrix element M_{dir} is proportional to the first powers of the exciton wavevectors: $M_{dir} \propto K_T$.

Next, we consider an exchange process, where the electron occupies the empty state in the valence band related to the hole in the other exciton, i.e. the electron with the wavevector \mathbf{k}_c transfers to the valence band state with the wavevector $\tilde{\mathbf{k}}_v$. As a result for uncorrelated electron-hole pairs we have for the exchange contribution

$$- M_1(|\mathbf{k}_c - \tilde{\mathbf{k}}_v|) \quad (5.15)$$

where M_1 is defined in Eq. (5.13). In order to transform Eq. (5.15) to the form convenient for averaging over the exciton wavefunctions we introduce the relative motion wavevectors for two initial and final exciton states in accordance with

$$\mathbf{k}_1 = \frac{\mathbf{k}_c + \mathbf{k}_v}{2}, \quad \mathbf{k}_2 = \frac{\tilde{\mathbf{k}}_c + \tilde{\mathbf{k}}_v}{2}, \quad \mathbf{k}_f = \frac{\mathbf{k}_{c'} + \mathbf{k}_v}{2} = \mathbf{k}_1 + \frac{\mathbf{K}_2}{2} \quad (5.16)$$

Here we assumed that the effective masses of the electron and hole are the same in agreement with microscopic calculations [179, 192]. Taking into account that, as before, the center of mass wavevectors $K_1, K_2 \sim K_T$ are small compared with the inverse Bohr

radius a_B^{-1} of exciton. We omit \mathbf{K}_f in $\mathbf{k}_c - \tilde{\mathbf{k}}_v = \mathbf{k}_1 - \mathbf{k}_2 + \mathbf{K}_f/2$ and $\mathbf{k}_1 + \mathbf{K}_f/2$ and arrive at

$$M_{exch}(\mathbf{K}_1, \mathbf{K}_2, \mathbf{K}_f, \nu) \approx -\delta_{\mathbf{K}_f, \mathbf{K}_1 + \mathbf{K}_2} \times \sum_{\mathbf{k}_1, \mathbf{k}_2} M_1(|\mathbf{k}_1 - \mathbf{k}_2|) C_\nu^*(\mathbf{k}_1) C_{1s}(k_2) C_{1s}(k_1) \quad (5.17)$$

Here $C_\nu(\mathbf{k})$ are the Fourier transforms of the relative motion exciton functions $\Phi_\nu(\boldsymbol{\rho})$:

$$C_\nu(\mathbf{k}) = \int d\boldsymbol{\rho} e^{i\mathbf{k}\cdot\boldsymbol{\rho}} \Phi_\nu(\boldsymbol{\rho})$$

It follows from Eq. (5.17) that only s -shell states contribute to the matrix element. Compared with its direct counterpart, the transferred momentum here is $|\mathbf{k}_1 - \mathbf{k}_2| \sim a_B^{-1}$. Since $M_1(q) \propto q$ for $qr_0 \ll 0$, direct contribution is by a factor $K_T a_B$ smaller than the exchange one. Thus, in what follows we consider the exchange contribution only.

In order to analyze the exchange process in more detail we first consider a limit where the screening is very strong, *i.e.*, where $|\mathbf{k}_1 - \mathbf{k}_2| r_0 \gg 1$. In this case we can approximate $M_1(q)$ by a constant and arrive at

$$M_{exch}(\mathbf{K}_1, \mathbf{K}_2, \mathbf{K}_f, \nu) \approx -\delta_{\nu, 1s} \delta_{\mathbf{K}_f, \mathbf{K}_1 + \mathbf{K}_2} \frac{2\pi e^2}{\varkappa r_0} \frac{\gamma_3^* \gamma_6}{E_g E'_g} \Phi_{1s}(0) \quad (5.18)$$

For arbitrary screening we evaluate the sum in Eq. (5.17) making use of the two-dimensional hydrogenic functions. For the bound states $\nu = ns$ we have [194]

$$C_{ns}(k) = 2\sqrt{2\pi} a_B \left(\frac{2n-1}{1+\kappa_n^2} \right)^{3/2} P_{n-1} \left(\frac{\kappa_n^2 - 1}{\kappa_n^2 + 1} \right) \quad (5.19)$$

with $\kappa_n = (2n-1)ka_B$ and $P_n(x)$ being the Legendre polynomial. As a result,

$$M_{exch}(\mathbf{K}_1, \mathbf{K}_2, \mathbf{K}_f, ns) = \frac{A_n(r_0)}{a_B^2} \frac{2\pi e^2 \gamma_3^* \gamma_6}{\varkappa E_g E'_g} \delta_{\mathbf{K}_f, \mathbf{K}_1 + \mathbf{K}_2} \quad (5.20)$$

Our target is to evaluate the scattering rate for excitons under the resonant condition $E_g = E'_g + 2E_B - E_{B,n}$, where the energy released at the non-radiative recombination of A:1s exciton with $K = 0$ is equal to the energy of the excited c' -band exciton in the ns -state. To that end, the distribution function $f(K)$ of excitons should be determined. It is determined by the interplay of the generation process and all types of relaxation processes, including exciton-exciton and exciton-phonon scattering as well as the radiative decay for the excitons with small wavevector K within the radiative cone and the redistribution of excitons between the bright and dark (spin-forbidden) states.

The generation rate of the excitons under the resonant excitation used in our experiments can be recast in the resonant form as (Eq. (A.9a) and Refs. [144, 152])

$$\left. \frac{dn_X}{dt} \right|_{gen} \propto \frac{1}{(\hbar\omega - E_{A:1s})^2 + \hbar^2 \Gamma_A^2} \frac{I}{\hbar\omega} \quad (5.21)$$

where $E_{A:1s} = E_g - E_B$ is the resonant energy of A:1s exciton, and Γ_A is the damping rate of this exciton.

Here we abstain of the presenting and solving the full kinetic equation model for exciton distribution and analyze the timescales of the most important processes. The calculations [136, 152, 195, 196] show that at cryogenic temperatures of 2...4 K the exciton-acoustic phonon scattering time is in the picosecond timescale, *i.e.* being on the same order of magnitude as the radiative decay rate (see Chapter 4, Purcell effect of TMD ML encapsulated in hBN). Thus, even at low temperatures photocreated excitons can efficiently leave the light cone to the nonradiative states. Additionally, as recently shown [152, 196], the pronounced high energy tails in the exciton absorption are caused by the exciton-phonon interaction, which can be accounted for by the ω -dependent Γ_A in Eq. (5.21). These tails are also well visible in the upconversion excitation spectra, Figure 5.1.1(d). Such processes can efficiently generate excitons with large wavevectors and energies [152]. By contrast, the rate of exciton-exciton Auger annihilation is about an order of magnitude smaller, see below. Thus, excitons are likely to thermalize [197].

The rate of the Auger processes is described by a parameter R_A such that the generation rate of highly energetic ns excitons through resonant interband scattering of two $1s$ excitons is given by

$$\frac{dn'_X}{dt} = R_A n_X^2 \quad (5.22)$$

Here n'_X is the density of highly energetic excitons, n_X is the density of photoexcited excitons in A:1s state, recombination and energy relaxation processes are disregarded in Eq. (5.22). The same rate $R_A n_X^2$ describes the decay rate of A:1s excitons due to the non-radiative exciton-exciton annihilation: $dn_X/dt = -R_A n_X^2$ [163, 182–185, 198–201]. The rate R_A can be expressed by means of the Fermi golden rule in the form

$$R_A = \frac{2\pi}{n_X^2 \hbar} \sum_{\mathbf{K}_1, \mathbf{K}_2, \nu} |M_{XX}|^2 f(K_1) f(K_2) \times \\ \delta[E_g - 2E_B - E'_g + E(K_1) + E(K_2) - E_\nu(K_f)] \quad (5.23)$$

Here M_{XX} is the matrix element of exciton-exciton interaction. \mathbf{K}_1 and \mathbf{K}_2 are the center of mass wavevectors of two interacting excitons. $f(K)$ is the distribution function of photoexcited A:1s excitons, $E(K) = \hbar^2 K^2 / 2M$ is the exciton dispersion with M being its effective mass, the subscript ν denotes the quantum numbers of final exciton states which include the electron band index [c or c' for the processes shown, in Figure 5.2.3(a) or (b)] as well as of the internal motion ($2s$, $2p$, ...including the continuum states), $E_\nu(K)$ is the dispersion of the exciton in the final state, which accounts for its binding energy. The exciton wavevector in the final state, \mathbf{K}_f is found from the momentum conservation law: $\mathbf{K}_f = \mathbf{K}_1 + \mathbf{K}_2$. For the derivation of Eq. (5.23) we assumed that the occupation of the final states is negligible and omitted the corresponding occupation factor and also disregarded the anisotropy and nonparabolicity of exciton dispersion.

Moreover, we have shown that the exchange contribution of relation Eq. (5.17) to the matrix element dominates over the direct part of relation Eq. (5.14). Thus Eq. (5.23) evolves into

$$R_A n_X^2 = \frac{2\pi}{\hbar} \sum_{\mathbf{K}_1, \mathbf{K}_2} |M_{exch}(\mathbf{K}_1, \mathbf{K}_2, \mathbf{K}_f, ns)|^2 f(K_1) f(K_2) \\ \times \delta[E_g - 2E_B - E'_g + E(K_1) + E(K_2) - E_{ns}(K_f)] \quad (5.24)$$

In order to calculate the rate of transitions, we take into account that the matrix element $M_{exch}(\mathbf{K}_1, \mathbf{K}_2, \mathbf{K}_f, ns)$ depends on the principal quantum number n of the final state and is independent of the initial wavevectors of excitons. Let us first assume that there is exact resonance, i.e., for the certain value of n at $\mathbf{K}_1 = \mathbf{K}_2 = \mathbf{K}_f$, we have

$$E_g = E'_g + 2E_B - E_{B,n} \quad (5.25)$$

where $E_{B,n}$ is the binding energy of ns state. Removing the energy conservation δ -function and assuming that

$$f(K) = \mathcal{N} \exp\left(-\frac{\hbar^2 K^2}{2Mk_B T}\right) \quad (5.26)$$

i.e., the excitons are distributed according to the Boltzmann law at the temperature T , \mathcal{N} is the normalization constant determined from the condition

$$n_X = g \sum_{\mathbf{K}} f(K),$$

where the factor g accounts for the spin and valley degeneracy. Finally, neglecting the difference of exciton masses in the initial and final states and assuming on the basis of the arguments above that excitons are thermalized with the temperature T , we have

$$R_A = R_n, \quad R_n = \frac{\pi}{\hbar k_B T} \left| \frac{2\pi e^2 \gamma_3 \gamma_6}{\varkappa a_B^2 E_g E'_g} \right|^2 |A_n|^2. \quad (5.27)$$

Here k_B is the Boltzmann constant, a_B is the exciton Bohr radius γ_3 and γ_6 are the interband momentum matrix elements (in the units of m_0/\hbar , m_0 being the free electron mass) for electron transition from c to, respectively, v and c' bands, \varkappa is the effective high-frequency dielectric constant. The analytical results of exciton Auger rate Eq. (5.27) is now obtained under the model assumptions $E_B \ll E_g, E'_g$ using $\mathbf{k} \cdot \mathbf{p}$ -perturbation theory for calculating the excitonic states and transition rates.

A_n in Eq. (5.27) is the dimensionless overlap integral for several excitonic states which depends on the screening parameter r_0 in the interaction potential Eq. (1.2). Dependence of $|A_n|^2$ on n for $r_0 = 3a_B$ is shown in Figure 5.2.4. We see that the squared matrix element decreases rapidly with n . It follows from Eq. (5.19) that $C_{n0} \propto n^{-3/2}$ at $n \rightarrow \infty$, therefore $|M_b|^2 \sim n^{-3}$. Figure 5.2.4 shows that this asymptotic is valid already at $n \geq 3$. The inset to Figure 5.2.4 shows the dependences of the scattering probability on the screening radius r_0 . Final states with $n = 1, 2, 3$ are considered. As it is mentioned above, scattering into the ns state for the short-range interaction is only possible at $n = 1$. The probability of this process decreases as $1/r_0^2$, while for $n \geq 2$ it drops as $1/r_0^4$. The corresponding asymptotes are shown by dashed lines in Figure 5.2.4.

For $n = 1$ and reasonable material parameters [192] the quantity R_A at $T = 4$ K in Eq. (5.27) can be estimated to be $1 \dots 10$ cm²/s. Note, that the Auger process is active for collisions of bright (spin-allowed) excitons with bright or dark ones, while for the dark-dark scattering the process is strongly suppressed. In the latter case the $\mathbf{k} \cdot \mathbf{p}$ admixture with the valence band is minor and the recombination via discussed channel is not effective. The Auger decay rate can be recast in the alternative form

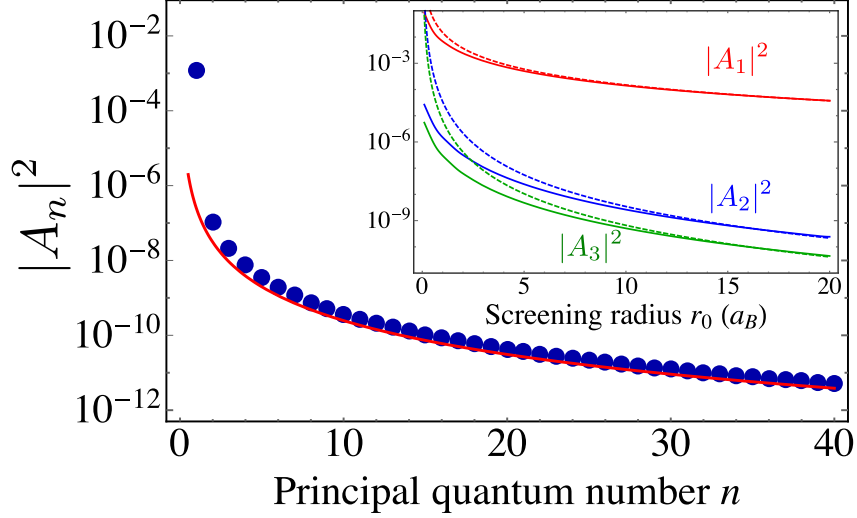


Figure 5.2.4: Dependence of the coefficient $|A_n|^2$ on n for $r_0 = 3a_B$. Red line shows the approximation $|A_n|^2 = 2.47 \times 10^{-7}/n^3$. Inset shows dependences $|A_1|^2$ (red), $|A_2|^2$ (blue) and $|A_3|^2$ (green) on the screening radius r_0 . Dashed lines are fits $|A_1|^2 = 0.015(a_B/r_0)^2$ and $|A_2|^2 = 3.46 \times 10^{-5}(a_B/r_0)^4$, $|A_3|^2 = 6.63 \times 10^{-6}(a_B/r_0)^4$.

$$R_A n_X^2 \equiv \frac{n_X}{\tau_A}, \quad (5.28)$$

where we introduced the Auger recombination time $\tau_A(n_X)$. Since $e^2/a_B \sim E_B$, we have an estimate in the case of the resonance with 1s state

$$\frac{1}{\tau_A} \sim \frac{n_X}{\hbar k_B T} \left(E_g \frac{a_0^2}{a_B} \right)^2, \quad (5.29)$$

where a_0 is the lattice constant. At $T = 4$ K, $a_0 = 3 \text{ \AA}$, $a_B = 1$ nm, $E_B = 0.5$ eV, and the exciton density $n_X = 10^9 \text{ cm}^{-2}$ this estimate yields $\tau_A \sim 25$ ps. Let us now take into account the detuning

$$\Delta = E'_g - E_g - E_{B,n} + 2E_B. \quad (5.30)$$

Accordingly, we have the sum over $K_{1,2}$ in the following form:

$$\sum_{\mathbf{K}_1, \mathbf{K}_2} f(K_1) f(K_2) \delta \left[\frac{\hbar^2 (K_1^2 + K_2^2 - |\mathbf{K}_1 + \mathbf{K}_2|^2)}{2M} - \Delta \right] = \frac{n_X^2}{2k_B T} e^{-|\Delta|/k_B T}. \quad (5.31)$$

We see that the difference with the case of zero detuning is the exponent. The Auger recombination rate including excitation detuning is given by

$$R_A = R_n e^{-|\Delta|/k_B T}. \quad (5.32)$$

Note that our experimental temperature $T = 4$ K corresponds to the thermal energy of $k_B T = 0.34$ meV. Eq. 5.32 shows the Auger recombination rate can thus be reduced by a factor 10...100, if the resonant condition is not fulfilled.

This analysis demonstrates that the dominating contribution to R_A is given by the resonant processes described in Figure 5.2.3(b) where the electron in the exciton is promoted to the excited band c' .

The experimentally observed Auger rates in the literature are 1-2 orders of magnitude smaller than the resonant contribution to R_A investigated here [126, 182, 183, 198–201]. The exact values of R_A will also vary with sample temperature and environment, demonstrating that the exact resonance conditions are not fulfilled in the studied structures. Furthermore, depending on the material, *e.g.* for W-based monolayers, a considerable part of excitonic population can be in the spin-dark states, which also affects the Auger rates, because for the Auger process at least one exciton should be spin-allowed. Our experiments are carried out at 4 K whereas many exciton-exciton scattering studies are carried out at elevated temperatures. The presence of disorder in the sample, especially without hBN encapsulation, may enable to fulfil simultaneously the energy and momentum conservation in TMD MLs making additional scenarios possible.

5.3 Conclusion

Excited exciton states in TMD MLs govern absorption and emission above the A:1s exciton resonance. We show that A:2s state is 120 meV (150 meV) above the A:1s state in ML MoTe₂ (MoSe₂) by using PL, PLE and Differential Reflectivity measurements. These states can also be measured in photoluminescence upconversion experiments. In addition to being a highly selective spectroscopic tool applicable to several TMD materials, this non-linear optical effect also gives insights into exciton-exciton interactions, relevant physical processes for studying population inversion and other density dependent phenomena [201–204].

Conclusions

We have fabricated van der Waals heterostructures based on Transition Metal Dichalcogenides monolayers (TMD MLs) encapsulated in hexagonal Boron Nitride (hBN). Thanks to the improved quality compared to the first generation of TMD MLs just transferred on SiO₂/Si substrates, we made some progress on the understanding and the control of the exciton properties.

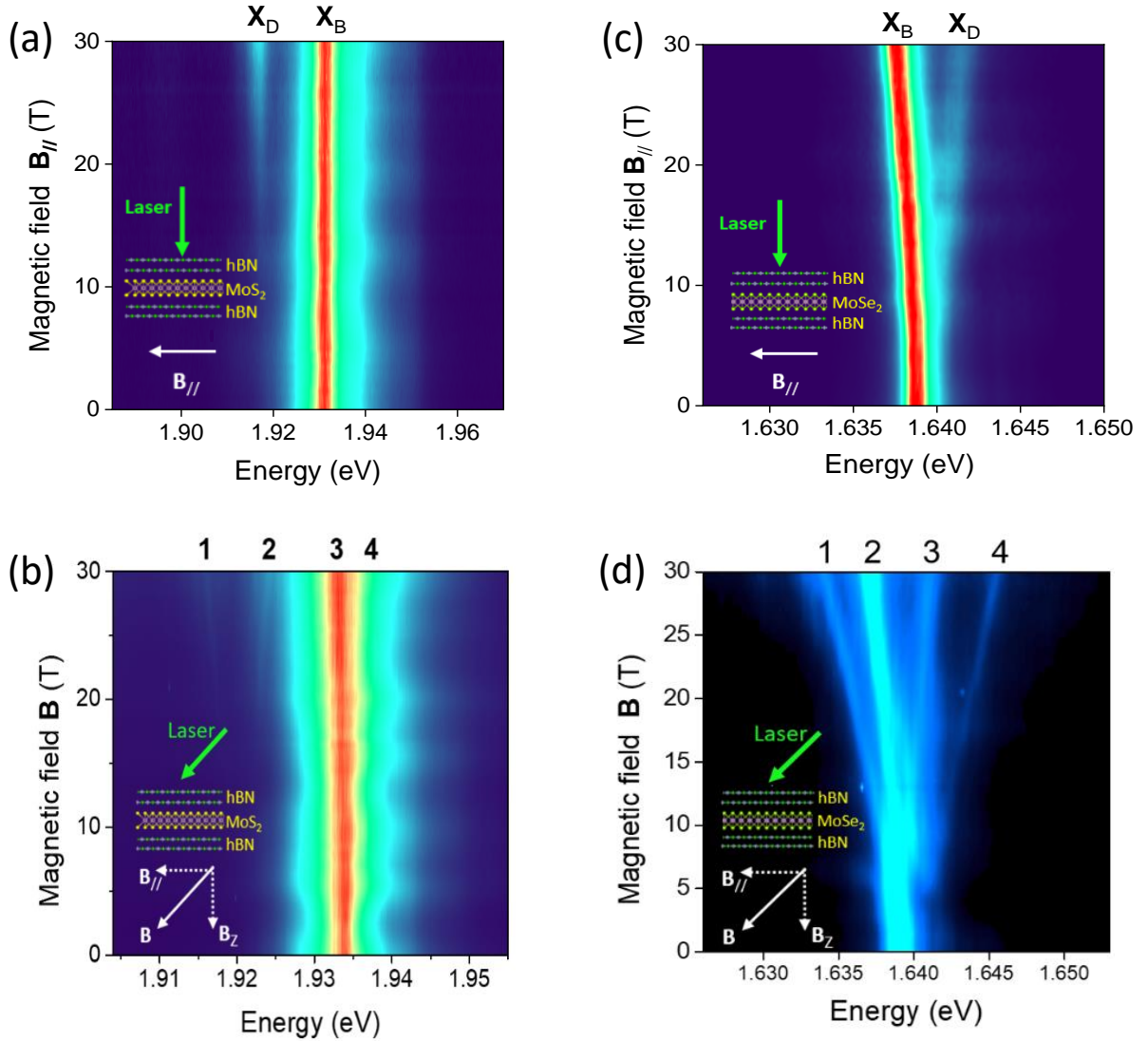


Figure 6.1: Magneto-Photoluminescence at ~ 4 K (a) MoS₂ ML in transverse and (b) 45° tilted magnetic fields. (c) MoSe₂ ML in transverse and (d) 45° tilted magnetic fields. X_B and X_D denote bright and dark exciton states, respectively. 1,2,3 and 4 denote the two bright X_B and two dark X_D mixed states.

First, we have performed Magneto-Photoluminescence (PL) experiments in transverse and tilted magnetic fields (45°) up to 30 T in high quality hBN encapsulated MoS₂ and MoSe₂ MLs. Figure 6.1 illustrates the key results presented in Chapter 3. These investigations, performed in collaboration with LNCMI Grenoble (Clément Faugeras and Marek Potemski), yield the unambiguous determination of the bright - dark exciton splitting: $\Delta = +14$ meV for MoS₂ and -1.4 meV for MoSe₂. Such fundamental parameters are key elements to understand the optoelectronic and spin/valley properties of these 2D semiconductors as well as their associated van der Waals heterostructures.

In Chapter 4, we have shown that the linewidth of hBN encapsulated MoSe₂ ML is not only close to the homogeneous linewidth but it is dominated by the radiative linewidth, see Figure 6.2(b). We demonstrate that we can control the exciton radiative recombination time by one order of magnitude from ~ 1 ps up to about 10 ps by just changing the bottom hBN thickness, as a result of Purcell effect, in agreement with a theoretical analysis based on a transfer matrix simulation, see Figure 6.2(a). This theoretical work was done in collaboration with Mikhail Glazov and Marina Semina from the IOFFE Institute in Saint Petersburg. This tuning of the radiative lifetime also helped us to understand the complex exciton/trion dynamics in TMD MLs. We look forward to engineering the exciton-photon coupling in these van der Waals heterostructures.

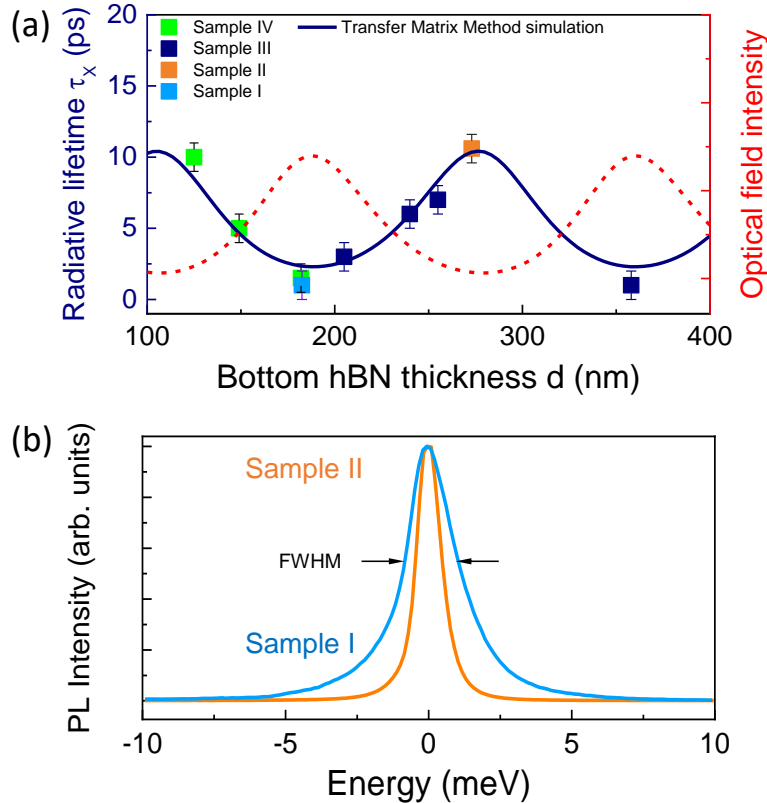


Figure 6.2: Purcell effect in MoSe₂ MLs. (a) Calculated (full line) and measured (symbols) neutral bright exciton radiative lifetime as a function of the hBN bottom layer thickness. The red dashed curve is the calculated intensity of the electromagnetic field. (b) Normalized CW PL intensity of the neutral bright exciton in Sample I and Sample II (MoSe₂ MLs on the anti-node and node of the electromagnetic field, respectively). All experimental data shown are acquired at $T = 7$ K.

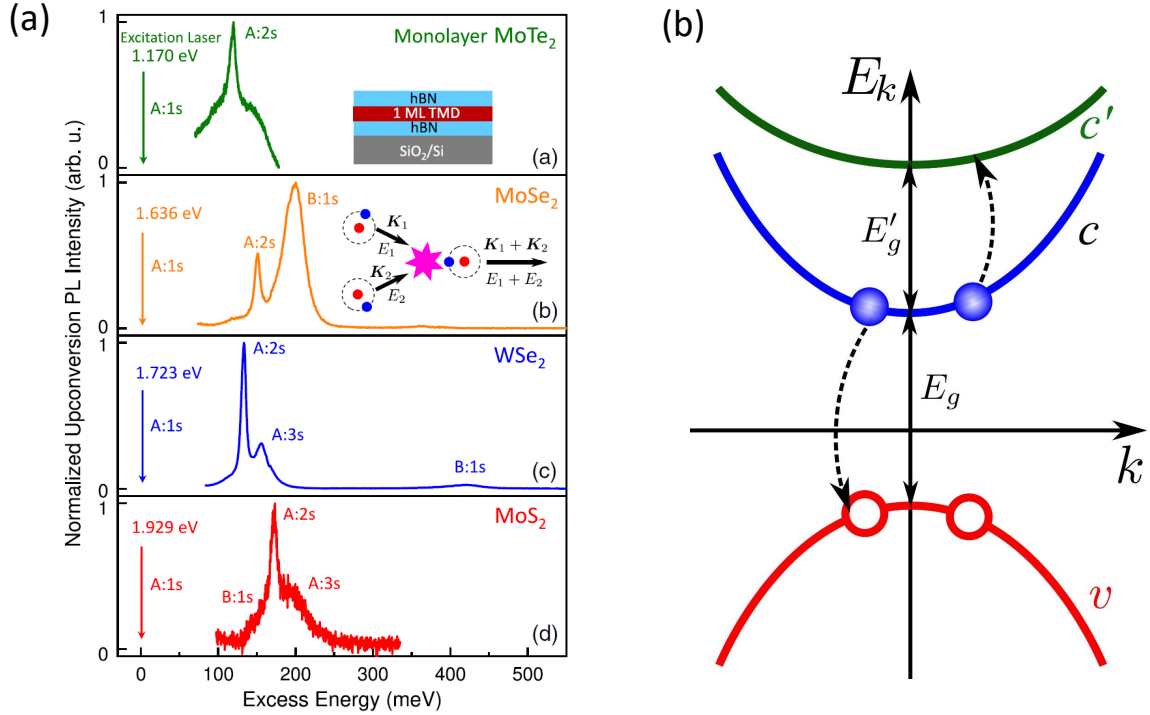


Figure 6.3: Exciton upconversion (a) Upconverted PL in four TMD MLs: MoTe₂, MoSe₂, WSe₂ and MoS₂ at a cryogenic temperature ~ 4 K. (b) Upconversion regime: resonant interband Auger scattering.

In Chapter 5, we explored the excited exciton states in TMD MLs that also govern absorption and emission above the A:1s exciton resonance. We show that A:2s state is 120 meV (150 meV) above the A:1s state in MoTe₂ ML (MoSe₂ ML) by using PL, PLE and differential reflectivity measurements. The exciton excited state series was not measured before in MoTe₂ ML. We also demonstrate that these states can also be measured in photoluminescence upconversion experiments, see Figure 6.3(a) which summarizes our results. In addition to being a highly selective spectroscopic tool applicable to several TMD materials, this non-linear optical effect also gives insights into exciton-exciton interactions, a relevant physical process for studying population inversion and other density dependent phenomena [201–204]. Thanks to a collaboration with Mikhail Glazov, we have developed a model suggesting that the strong exciton upconversion effects in TMD MLs is a result of a very efficient interband Auger scattering process, see Figure 6.3(b).

Perspectives

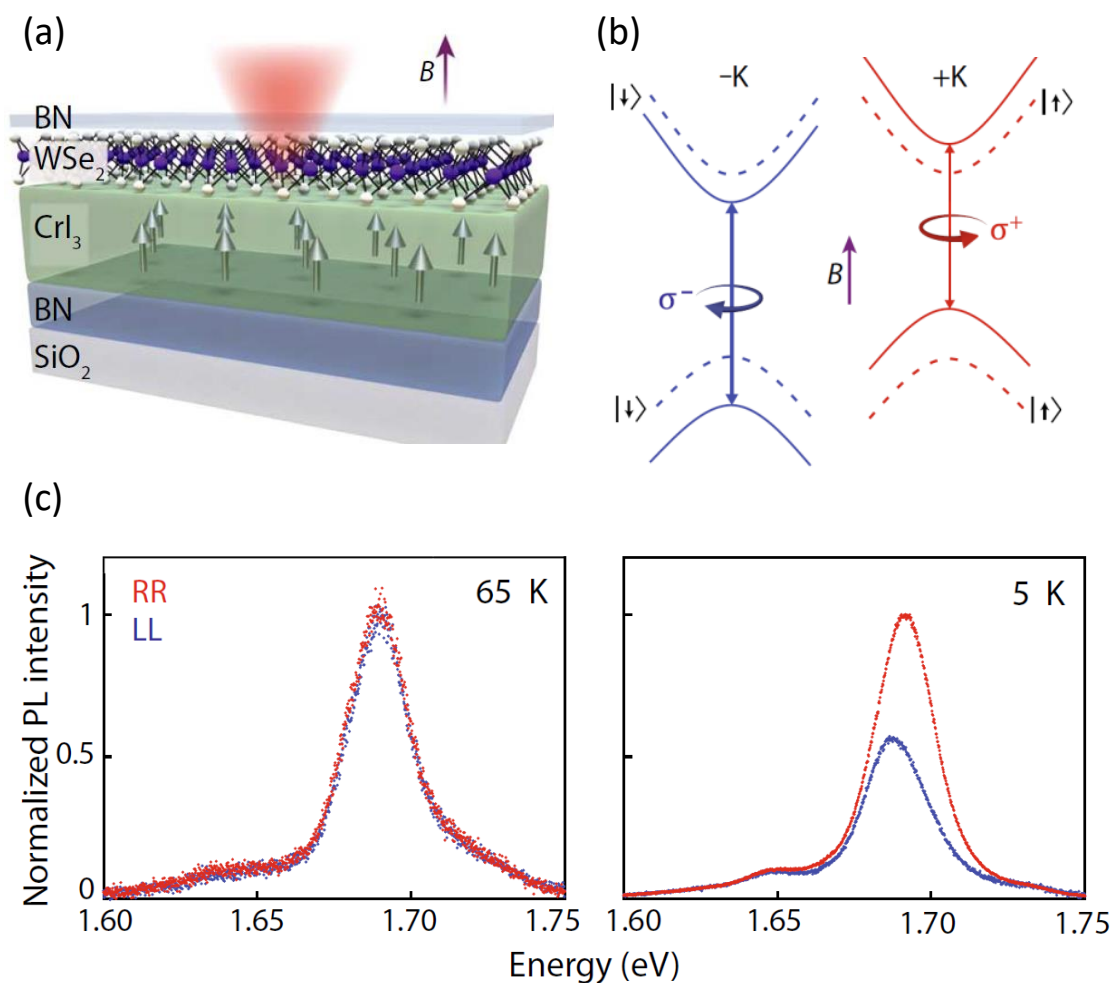


Figure 6.4: Proximity effect in hBN encapsulated WSe₂/CrI₃ heterostructure extracted from Ref. [205]: (a) Sample structure: hBN/WSe₂ ML/CrI₃ (10 nm)/hBN. (b) Schematics of Valley Zeeman splitting in a longitudinal magnetic field. (c) Circular polarization resolved PL measurements at 65 K and 5 K.

The exciton fine structure and excited exciton states in TMD MLs are now better understood. Future works could be towards engineering and manipulating the spin and valley degree of freedom in TMD MLs. One promising way is to combine the TMD MLs with magnetic 2D materials [206], such as the Ising-type CrI₃ and CrBr₃ [54, 207, 208] and Heisenberg-type Cr₂Ge₂Te₆ [209, 210]. The ferromagnetic proximity effects based on in-

terlayer exchange interaction [211] and spin-dependent recombination will play important roles in TMD ML/2D-ferromagnetic heterostructures.

There are several theoretical predictions of the proximity effects between TMD MLs and magnetic substrates [212–214]. The first experimental demonstrations were obtained by Xiaodong Xu’s group from University of Washington [205, 215], in which they performed circular polarization-resolved PL measurements on a hBN encapsulated WSe₂ ML and CrI₃ heterostructure. CrI₃ is a magnetic semiconductor with a Curie temperature $T_c \sim 61$ K and easy axis aligning normal to the 2D plane, see Figure 6.4(a). The monolayer form of CrI₃ is ferromagnetic [216–218] and shows polarized PL emission that depends on the magnetic direction [219]. The interlayer coupling of few-layer CrI₃ was initially determined as antiferromagnetic [54, 219]. Proximity effect between WSe₂ ML and CrI₃ at 5 K is evidenced by the zero-field valley Zeeman splitting of 3.5 meV that corresponds to 13 T longitudinal magnetic field, see Figure 6.4(b,c). Proximity effect has also been observed for systems of WSe₂ ML on EuS [220] and MoTe₂ ML on EuO [221].

During my PhD thesis, I also started to work in this field and got some preliminary results. We have fabricated several hBN/ WSe₂ ML/ CrI₃/ hBN and hBN/ WSe₂ ML/ CrBr₃/ hBN heterostructures. However, we still do not have clear demonstration of the proximity effects. Though the samples were fabricated in clean environment (glovebox), we hypothesize some possible contaminations of interfaces, which further induces a deterioration of CrI₃ properties. We also have some preliminary results on hBN encapsulated WSe₂/CrTe₂ (~ 10 nm) heterostructures. The 1T-CrTe₂ bulk is provided by our collaborator Johann Coraux from NÉEL Institute of Grenoble, France [222]. CrTe₂ is metallic ferromagnet at RT with easy axis lying in-plane [222, 223]. When a longitudinal magnetic field increases, the spins in CrTe₂ flake are gradually aligned perpendicular to the layer. We performed circular polarization-resolved PL measurements. Following circularly polarized excitation, we measured a remarkably large circular polarization ~ 80 % of the trion emissions (X_{T1} and X_{T2}) in the hybrid heterostructure, see Figure 6.5(a). The typical value for an hBN encapsulated WSe₂ ML is only 30 \sim 50 % without any magnetic materials. We observed in Figure 6.5(a) the tuning of this polarization with the longitudinal magnetic field. Though this result is encouraging and seems to show an effect of the CrTe₂ magnetic layer on the WSe₂ properties, it is too early to conclude on a possible proximity effect. As a matter of fact, the large circular polarization measured at zero external magnetic field could be simply due to the reduction of the trion lifetime resulting from the efficient tunneling into the metallic CrTe₂ layer. A possible effect of spin-dependent transfer to this layer should be checked in the future.

Another fingerprint of possible interactions between the semiconducting WSe₂ and the magnetic CrTe₂ layer is shown in Figure 6.5(b). In that case, the laser excitation is linearly polarized and we measure the circular polarization of the luminescence. An interesting feature is that the trion emission is circularly polarized ~ 20 % even for zero external magnetic field. This could be the result of a magnetic proximity effect. However, as explained above, CrTe₂ layers are usually considered to have an in-plane magnetization. This raises problems to interpret the results in Figure 6.5(b). Nevertheless, almost nothing is known about the magnetic properties for CrTe₂ layers as thin as the ones we have used in our WSe₂/CrTe₂ heterostructure. The priority for further investigation is clearly to measure the magnetic properties of thin CrTe₂ layers alone.

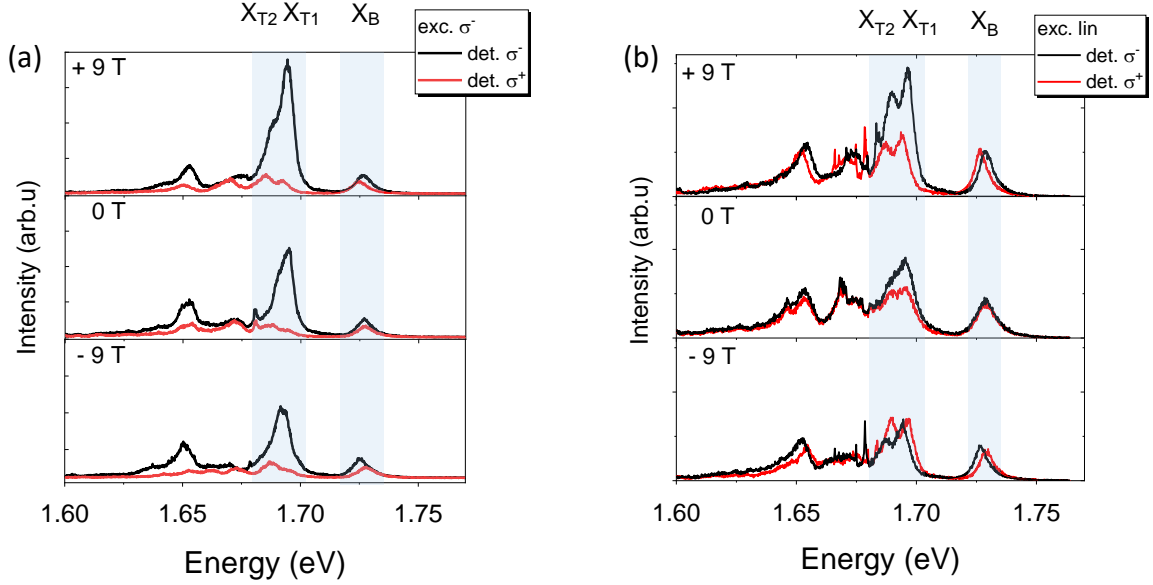


Figure 5.3.1: Polarization measurements of hBN/WSe₂ ML/CrTe₂/hBN at 4K. (a) Circular polarization PL measurements by using σ^- excitation at + 9, 0 and -9 T longitudinal magnetic fields. X_{T1} and X_{T2} denote the trion transitions. X_B denotes bright neutral excitons. (b) Linear excitation with circular detection at + 9, 0 and -9 T.

In order to understand the properties of these hybrid TMD ML/FM heterostructures, substantial work has to be done in the future, for example theoretical calculations of band structure alignment [224] and probing the magnetic properties using Raman scattering [225], second harmonic generation (SHG) [226], magnetic circular dichroism (MCD) [227] and magneto-optical Kerr effect (MOKE) [228], etc. The main challenges for observing these subtle effects and applications lie in following aspects: (i) understand the intrinsic properties of magnetic 2D materials; (ii) ultraclean heterostructure interface; (iii) control of the magnetic domain and possible Moiré effects [229]; (iv) proper experimental methods to extract magnetic interactions; (v) continuous search for materials with ferromagnetic order at room temperature [230, 231] and insensitive to ambient environment [232].

Appendix A

Other Exciton Upconversion Mechanisms

A.1 Resonant intraband Auger process

Let us briefly address the intraband process depicted in Figure 5.2.3(a) where the charge carriers remain in the same bands after the scattering. In the non-resonant case where at $K_1 = K_2 = 0$ the resonant transition is not possible and the detuning $\Delta = E'_g - E_g + 2E_B - E_{B,n}$ is present for the intraband process. This intraband process is only possible when excitons with the kinetic energy on the order of Δ are present. The rate Eq. (5.27) therefore acquires an exponential factor $\exp(-|\Delta|/k_B T) < 1$.

For free carriers the process has a high threshold requiring the initial and final wavevectors to be on the order of $\sqrt{ME_g/\hbar^2}$, otherwise the energy and momentum conservation laws cannot be satisfied simultaneously. With account for the excitonic effect the process becomes allowed because one can find, in the relative motion wavefunction Fourier image, Eq. (5.19), sufficiently large wavevectors due to the Coulomb interaction. In other words, the electron-hole Coulomb interaction either in the initial or in the final state may relax the momentum conservation in the course of the Auger scattering. However, the two band approximation is insufficient to give a correct result, since (i) the model approximations for the band dispersions are, as a rule, invalid at the kinetic energies $\sim E_g$ due to the $\mathbf{k} \cdot \mathbf{p}$ interaction with remote bands [179, 184] and (ii) the asymptotic form of $C_\nu(k)$ at large wavevectors can strongly differ from a simplified hydrogenic model Eq. (5.19) [27, 28, 193]. Thus, we present here only analytical estimations based on the parabolic approximations for the band dispersions and assuming that the ratio E_g/E_B is very large, which allows to take into account the Coulomb effects perturbatively.

We start from the direct process. Instead of Eq. (5.13) we have for the free carrier scattering

$$V_C(K_1) \frac{\gamma_3^* K_{1,+}}{E_g} \delta_{\mathbf{K}_1, \mathbf{k}_c - \mathbf{k}_v} \delta_{\mathbf{K}_1, \mathbf{k}_{c'} - \tilde{\mathbf{k}}_c} \quad (\text{A.1})$$

As compared with Eq. (5.13) the factor $\propto \gamma_6/E'_g$ is absent due to the fact that only one charge carrier changes the band. Making use of the following notations

$$\mathbf{k}_{c'} = \mathbf{k}_f + \frac{\mathbf{K}_1 + \mathbf{K}_2}{2} = \mathbf{k}_f + \frac{\mathbf{K}_f}{2} \quad (\text{A.2})$$

$$\mathbf{k}_c = \mathbf{k}_f + \frac{\mathbf{K}_2 - \mathbf{K}_1}{2} \quad (\text{A.3})$$

we obtain for the exciton Auger scattering matrix element the following expression

$$M'_{dir}(\mathbf{K}_1, \mathbf{K}_2, \mathbf{K}_f, \mathbf{k}_f) = \delta_{\mathbf{K}_f, \mathbf{K}_1 + \mathbf{K}_2} \times \Phi_{1s}(0) \frac{V_C(K_1) \gamma_3^* K_{1,+}}{E_g} \int d\mathbf{r} e^{i\mathbf{K}_1 \cdot \mathbf{r}/2} \Phi_{k_f, l}^*(\mathbf{r}) \Phi_{1s}(\mathbf{r}) + \mathbf{K}_1 \leftrightarrow \mathbf{K}_2. \quad (\text{A.4})$$

Here we take into account that only excitons with positive energies of relative motion can be in the final state, *i.e.*, k_f corresponds to the continuum electron-hole pair state modified by the Coulomb interaction. The final state wavevector can be estimated from the energy conservation condition with the result $k_f = \sqrt{(E_g - 2E_B)M/(2\hbar^2)}$. In this estimate we neglected thermal energy of excitons as compared with $E_g - 2E_B$ and took the same effective masses as before for an electron and a hole.

Since $K_1 \ll a_B^{-1}, k_f$ the integral in Eq. (A.4) can be evaluated by decomposing the exponent in the series. At $K_1 = 0$ the integral in Eq. (A.4) equals to zero due to orthogonality of the functions of discrete and continuous spectra. Therefore we take into account the K_1 -linear term:

$$\int d\mathbf{r} e^{i\mathbf{K}_1 \cdot \mathbf{r}/2} \Phi_{k_f, l}^*(\mathbf{r}) \Phi_{1s}(\mathbf{r}) \approx a_B K_1 D(k_f) \quad (\text{A.5})$$

where

$$D(k_f) = \frac{ia_B}{2} \int d\mathbf{r} r \cos \varphi \Phi_{k_f, 1}^*(\mathbf{r}) \Phi_{1s}(r) \ll 1 \quad (\text{A.6})$$

Within the hydrogenic model, which is used hereafter for crude estimations, $D(k_f) \propto (k_f a_B)^{-3}$ and the ratio of the interband contribution Eq. (5.14) and the intraband contribution Eq. (A.4) can be estimated as

$$\left| \frac{M_{dir}}{M'_{dir}} \right| \sim \frac{\gamma_6}{a_B E'_g} \left(\frac{E_g}{E_B} \right)^{3/2} \sim \frac{E_g}{E_B} \gg 1 \quad (\text{A.7})$$

Similar estimation holds for the exchange contributions. The resonant interband Auger process is thus dominant.

A.2 Two step absorption

Let us briefly address other possible origins of the upconversion effect. The straightforward case is a two step exciton absorption process: hot photoluminescence excited by two-photon absorption. We will show that this process is about 3 orders of magnitude weaker than the resonant Auger process described in Chapter 5.

In order to analyze the two photon absorption via the exciton state we present a simple three-state model describing the dynamics of the ground state of the crystal $|0\rangle$ (no excitons), $|A : 1s\rangle$ (A : $1s$ exciton), and excited state $|f\rangle$ (the exciton formed of the electron in the c' band and the hole in the valence band v). Expanding the wavefunction of the system over these states and introducing the decomposition coefficients, respectively, C_0 , $C_{A:1s}$ and C_f , we obtain from the second-order time-dependent perturbation theory

$$C_0 = 1 \quad (\text{A.8a})$$

$$C_{A:1s} = \frac{V_{A0}}{\hbar\omega - E_{A:1s} + i\hbar\Gamma_A} \quad (\text{A.8b})$$

$$C_f = \frac{V_{fA}V_{A0}}{(2\hbar\omega - E_f + i\hbar\Gamma_f)(\hbar\omega - E_{A:1s} + i\hbar\Gamma_A)} \quad (\text{A.8c})$$

Here ω is the energy of the incident radiation, $E_{A:1s} = E_g - E_B$ is the excitation energy of the A -exciton, E_f is the energy of the exciton in the final state $|f\rangle$, Γ_A and Γ_f are the dampings of these states. In Eq. (A.8) the matrix elements V_{A0} and V_{fA} are the matrix elements of exciton excitation for the processes $v \rightarrow c$ and $c \rightarrow c'$, respectively, see below for explicit expressions. In this simplified approach the steady-state populations of A : $1s$ state and of f state read

$$N_{A:1s} = |C_{A:1s}|^2 = \frac{|V_{A0}|^2}{(\hbar\omega - E_A)^2 + \hbar^2\Gamma_A^2} \quad (\text{A.9a})$$

$$N_f = |C_f|^2 = \frac{|V_{fA}|^2}{(2\hbar\omega - E_f)^2 + \hbar^2\Gamma_f^2} \times N_{A:1s} \quad (\text{A.9b})$$

Note that Eq. (A.9a) gives the spectral shape of one-photon absorption in the vicinity of A : $1s$ exciton resonance, while Eq. (A.9b) gives the spectral shape of the two-photon absorption. It is instructive to estimate the two step photon absorption induced generation rate of excitons in the excited states. Taking into account that in our model the lifetime of the state $|f\rangle$ reads $\tau_f = 1/(2\Gamma_f)$, the generation rate of the excitons in the $|f\rangle$ state can be written as

$$R_{TSA} = \frac{N_{A:1s}}{\tau_{TPA}}, \quad \frac{1}{\tau_{TPA}} = \frac{2\Gamma_f|V_{fA}|^2}{(2\hbar\omega - E_f)^2 + \hbar^2\Gamma_f^2} \quad (\text{A.10})$$

The calculation shows that the absolute values squared of the matrix elements take the form

$$|V_{A0}|^2 = \left| \frac{e\gamma_3}{E_g} \mathcal{E}_\omega \right|^2 \Phi_{1s}^2(0), \quad |V_{fA}|^2 = \left| \frac{e\gamma_6}{E'_g} \mathcal{E}_\omega \right|^2 \quad (\text{A.11})$$

Here the normalization area is set to unity, we neglect the difference between $\hbar\omega$, E_g and E'_g and disregard the difference of the exciton envelope functions in the intermediate and final states, \mathcal{E}_ω is the amplitude of the incident electromagnetic field. For rough estimation, we put $\Gamma_f = \Gamma_A \equiv \Gamma$ as well as $\gamma_3 = \gamma_6$ and assume that the double-resonant condition $2\hbar\omega \approx E_f$, $\hbar\omega \approx E_A$ (which overestimates the rate of transition) we obtain

$$\frac{1}{\tau_{TSA}} \sim \Gamma \frac{n_X}{|\Phi_{1s}(0)|^2} \sim \Gamma n_X a_B^2 \quad (\text{A.12})$$

A reasonable $\Gamma \sim 1$ meV gives $\tau_{TSA} \sim 100$ ns under the exciton density as the resonant Auger time of $\tau_A \sim 25$ ps estimated in Eq. (5.29). The estimation of two-photon absorption is three orders of magnitude smaller. We thus may conclude that the direct two step photon absorption is much weaker than the Auger-like process.

Note that, strictly speaking, both V_{A0} and V_{fA} are proportional to the amplitude of the incident electric field \mathcal{E}_ω . We thus have $N_f \propto I^2$. Therefore, the dependence $I_{up} \propto I^2$ is expected in two-photon absorption process, in contrast to the experimental observations in Figure 5.1.1(c). The saturation of absorption of the A:1s state resulting in Γ_A dependent on $n_{A:1s}$ may somewhat reduce the scaling power of the I_{up} vs. I dependence. However, the present analysis cannot fully rule out such a process as well as more sophisticated processes where the exciton-phonon interaction is involved at one of the steps of the two-photon absorption. The detailed calculation of the rates of these processes can be oversimplified, because of imprecise knowledge of the band structure parameters and therefore it is impossible to know to which extent all needed resonance conditions are fulfilled. We believe that this analysis will stimulate further experimental and theoretical studies aimed in particular at specifying band parameters of two-dimensional materials.

Bibliography

- [1] Jiahao Kang, Wei Cao, Xuejun Xie, Deblina Sarkar, Wei Liu, and Kaustav Banerjee. Graphene and beyond-graphene 2D crystals for next-generation green electronics. In *Micro-and Nanotechnology Sensors, Systems, and Applications VI*, volume 9083, page 908305. International Society for Optics and Photonics, 2014.
- [2] Anasua Chatterjee, Paul Stevenson, Silvano De Franceschi, Andrea Morello, Nathalie de Leon, and Ferdinand Kuemmeth. Semiconductor qubits in practice. *arXiv preprint arXiv:2005.06564*, 2020.
- [3] Konstantin S Novoselov, Andre K Geim, Sergei V Morozov, Da Jiang, Y. Zhang, Sergey V Dubonos, Irina V Grigorieva, and Alexander A Firsov. Electric field effect in atomically thin carbon films. *Science*, 306(5696):666–669, 2004.
- [4] Changgu Lee, Xiaoding Wei, Jeffrey W Kysar, and James Hone. Measurement of the elastic properties and intrinsic strength of monolayer graphene. *Science*, 321(5887):385–388, 2008.
- [5] Alexander A Balandin, Suchismita Ghosh, Wenzhong Bao, Irene Calizo, Desalegne Teweldebrhan, Feng Miao, and Chun Ning Lau. Superior thermal conductivity of single-layer graphene. *Nano Letters*, 8(3):902–907, 2008.
- [6] Qing Hua Wang, Kourosh Kalantar-Zadeh, Andras Kis, Jonathan N Coleman, and Michael S Strano. Electronics and optoelectronics of two-dimensional transition metal dichalcogenides. *Nature Nanotechnology*, 7(11):699, 2012.
- [7] Jan Kopaczek, Maciej P Polak, Pawel Scharoch, Ke Wu, Bin Chen, Sefaattin Tongay, and Robert Kudrawiec. Direct optical transitions at k-and h-point of brillouin zone in bulk MoS₂, MoSe₂, WS₂ and WSe₂. *Journal of Applied Physics*, 119(23):235705, 2016.
- [8] Andrea Splendiani, Liang Sun, Yuanbo Zhang, Tianshu Li, Jonghwan Kim, Chi-Yung Chim, Giulia Galli, and Feng Wang. Emerging photoluminescence in monolayer MoS₂. *Nano Letters*, 10(4):1271–1275, 2010.
- [9] Andor Kormányos, Guido Burkard, Martin Gmitra, Jaroslav Fabian, Viktor Zólyomi, Neil D Drummond, and Vladimir Fal'ko. $k \cdot p$ theory for two-dimensional transition metal dichalcogenide semiconductors. *2D Materials*, 2(2):022001, 2015.
- [10] Yi Zhang, Tay-Rong Chang, Bo Zhou, Yong-Tao Cui, Hao Yan, Zhongkai Liu, Felix Schmitt, James Lee, Rob Moore, Yulin Chen, Hsin Lin, Horng-Tay Jeng, Sung-Kwan Mo, Zahid Hussain, Arun Bansil, and Zhi-Xun Shen. Direct observation of the transition from indirect to direct bandgap in atomically thin epitaxial MoSe₂. *Nature Nanotechnology*, 9(2):111, 2014.
- [11] Sung-Kwan Mo. Angle-resolved photoemission spectroscopy for the study of two-dimensional materials. *Nano Convergence*, 4(1):6, 2017.
- [12] Nasser Alidoust, Guang Bian, Su-Yang Xu, Raman Sankar, Madhab Neupane, Chang Liu, Ilya Belopolski, Dong-Xia Qu, Jonathan D Denlinger, Fang-Cheng Chou, and M Zahid Hasan. Observation of monolayer valence band spin-orbit effect and induced quantum well states in MoX₂. *Nature Communications*, 5(1):1–9, 2014.
- [13] Po-Chun Yeh, Wencan Jin, Nader Zaki, Datong Zhang, Jonathan T Liou, Jerzy T Sadowski, Abdullah Al-Mahboob, Jerry I Dadap, Irving P Herman, Peter Sutter, and Richard M Osgood Jr. Layer-dependent electronic structure of an atomically heavy two-dimensional dichalcogenide. *Physical Review B*, 91(4):041407, 2015.
- [14] Wencan Jin, Po-Chun Yeh, Nader Zaki, Datong Zhang, Jerzy T Sadowski, Abdullah Al-Mahboob, Arend M van Der Zande, Daniel A Chenet, Jerry I Dadap, Irving P Herman, Petter Sutter, James Hone, and Richard M Osgood Jr. Direct measurement of the thickness-dependent electronic band structure of MoS₂ using angle-resolved photoemission spectroscopy. *Physical Review Letters*, 111(10):106801, 2013.
- [15] Miguel M Ugeda, Aaron J Bradley, Su-Fei Shi, Felipe H da Jornada, Yi Zhang, Diana Y Qiu, Wei Ruan, Sung-Kwan Mo, Zahid Hussain, Zhi-Xun Shen, Feng Wang, Steven G Louie, and Michael F Crommie. Giant bandgap renormalization and excitonic effects in a monolayer transition metal dichalcogenide semiconductor. *Nature Materials*, 13(12):1091–1095, 2014.
- [16] Kin Fai Mak, Changgu Lee, James Hone, Jie Shan, and Tony F Heinz. Atomically thin MoS₂: a new direct-gap semiconductor. *Physical Review Letters*, 105(13):136805, 2010.

- [17] Albert F Rigosi, Heather M Hill, Kwang Taeg Rim, George W Flynn, and Tony F Heinz. Electronic band gaps and exciton binding energies in monolayer $\text{Mo}_x\text{W}_{1-x}\text{S}_2$ transition metal dichalcogenide alloys probed by scanning tunneling and optical spectroscopy. *Physical Review B*, 94(7):075440, 2016.
- [18] Ming-Hui Chiu, Chendong Zhang, Hung-Wei Shiu, Chih-Piao Chuu, Chang-Hsiao Chen, Chih-Yuan S Chang, Chia-Hao Chen, Mei-Yin Chou, Chih-Kang Shih, and Lain-Jong Li. Determination of band alignment in the single-layer $\text{MoS}_2/\text{WSe}_2$ heterojunction. *Nature Communications*, 6(1):1–6, 2015.
- [19] Chendong Zhang, Yuxuan Chen, Amber Johnson, Ming-Yang Li, Lain-Jong Li, Patrick C Mende, Randall M Feenstra, and Chih-Kang Shih. Probing critical point energies of transition metal dichalcogenides: surprising indirect gap of single layer WSe_2 . *Nano Letters*, 15(10):6494–6500, 2015.
- [20] Alexey Chernikov, Timothy C Berkelbach, Heather M Hill, Albert Rigosi, Yilei Li, Ozgur Burak Aslan, David R Reichman, Mark S Hybertsen, and Tony F Heinz. Exciton binding energy and nonhydrogenic rydberg series in monolayer WS_2 . *Physical Review Letters*, 113(7):076802, 2014.
- [21] Liam Britnell, Ricardo M Ribeiro, Axel Eckmann, Rashid Jalil, Branson D Belle, Artem Mishchenko, Yong-Jin Kim, Roman V Gorbachev, Thanasis Georgiou, Sergei V Morozov, Alexander N Grigorenko, Andre K Geim, Cinzia Casiraghi, Antonio H Castro Neto, Konstantin S Novoselov. Strong light-matter interactions in heterostructures of atomically thin films. *Science*, 340(6138):1311–1314, 2013.
- [22] Archana Raja, Lutz Waldecker, Jonas Zipfel, Yeongsu Cho, Samuel Brem, Jonas D Ziegler, Marvin Kulig, Takashi Taniguchi, Kenji Watanabe, Ermin Malic, Tony F Heinz, Timothy C Berkelbach, and Alexey Chernikov. Dielectric disorder in two-dimensional materials. *Nature Nanotechnology*, 14(9):832–837, 2019.
- [23] Andreas V Stier, Nathan P Wilson, Genevieve Clark, Xiaodong Xu, and Scott A Crooker. Probing the influence of dielectric environment on excitons in monolayer WSe_2 : insight from high magnetic fields. *Nano Letters*, 16(11):7054–7060, 2016.
- [24] Yeongsu Cho and Timothy C Berkelbach. Environmentally sensitive theory of electronic and optical transitions in atomically thin semiconductors. *Physical Review B*, 97(4):041409, 2018.
- [25] Simone Latini, Thomas Olsen, and Kristian Sommer Thygesen. Excitons in van der waals heterostructures: The important role of dielectric screening. *Physical Review B*, 92(24):245123, 2015.
- [26] Mark Fox. Optical properties of solids, 2002.
- [27] Diana Y Qiu, Felipe H da Jornada, and Steven G Louie. Optical spectrum of MoS_2 : many-body effects and diversity of exciton states. *Physical Review Letters*, 111(21):216805, 2013.
- [28] Gang Wang, Alexey Chernikov, Mikhail M Glazov, Tony F Heinz, Xavier Marie, Thierry Amand, and Bernhard Urbaszek. Colloquium: Excitons in atomically thin transition metal dichalcogenides. *Reviews of Modern Physics*, 90(2):021001, 2018.
- [29] Mikhail M Glazov, Eougenious L Ivchenko, Gang Wang, Thierry Amand, Xavier Marie, Bernhard Urbaszek, and Baoli Liu. Spin and valley dynamics of excitons in transition metal dichalcogenide monolayers. *Physica Status Solidi (b)*, 252(11):2349–2362, 2015.
- [30] Ziliang Ye, Ting Cao, Kevin O’ brien, Hanyu Zhu, Xiaobo Yin, Yuan Wang, Steven G Louie, and Xiang Zhang. Probing excitonic dark states in single-layer tungsten disulphide. *Nature*, 513(7517):214–218, 2014.
- [31] Gang Wang, Xavier Marie, Iann C Gerber, Thierry Amand, Delphine Lagarde, Louis Bouet, M Vidal, Andrea Balocchi, and Bernhard Urbaszek. Giant enhancement of the optical second-harmonic emission of WSe_2 monolayers by laser excitation at exciton resonances. *Physical Review Letters*, 114(9):097403, 2015.
- [32] Keliang He, Nardeep Kumar, Liang Zhao, Zefang Wang, Kin Fai Mak, Hui Zhao, and Jie Shan. Tightly bound excitons in monolayer WSe_2 . *Physical Review Letters*, 113(2):026803, 2014.
- [33] Mikhail M Glazov, Leonid E Golub, Gang Wang, Xavier Marie, Thierry Amand, and Bernhard Urbaszek. Intrinsic exciton-state mixing and nonlinear optical properties in transition metal dichalcogenide monolayers. *Physical Review B*, 95(3):035311, 2017.
- [34] Cédric Robert, MA Semina, F Cadiz, M Manca, E Courtade, T Taniguchi, K Watanabe, H Cai, Sefaattin Tongay, Benjamin Lassagne, et al. Optical spectroscopy of excited exciton states in mos_2 monolayers in van der waals heterostructures. *Physical Review Materials*, 2(1):011001, 2018.
- [35] Pierluigi Cudazzo, Ilya V Tokatly, and Angel Rubio. Dielectric screening in two-dimensional insulators: Implications for excitonic and impurity states in graphene. *Physical Review B*, 84(8):085406, 2011.
- [36] Bo Han, Cédric Robert, Emmanuel Courtade, Marco Manca, Shivangi Shree, Thierry Amand, Pierre Renucci, Takashi Taniguchi, Kenji Watanabe, Xavier Marie, Leonid E Golub, Mikhail M Glazov and Bernhard Urbaszek. Exciton states in monolayer MoSe_2 and MoTe_2 probed by upconversion spectroscopy. *Physical Review X*, 8(3):031073, 2018.

- [37] Andreas V Stier, Nathan P Wilson, Kirill A Velizhanin, Junichiro Kono, Xiaodong Xu, and Scott A Crooker. Magneto-optics of exciton Rydberg states in a monolayer semiconductor. *Physical Review Letters*, 120(5):057405, 2018.
- [38] Dinh Van Tuan, Min Yang, and Hanan Dery. Coulomb interaction in monolayer transition-metal dichalcogenides. *Physical Review B*, 98(12):125308, 2018.
- [39] Gang Wang, Cédric Robert, Aslihan Suslu, Bin Chen, Sijie Yang, Sarah Alamdari, Iann C Gerber, Thierry Amand, Xavier Marie, Sefaattin Tongay, and Bernhard Urbaszek. Spin-orbit engineering in transition metal dichalcogenide alloy monolayers. *Nature Communications*, 6(1):1–7, 2015.
- [40] Di Xiao, Gui-Bin Liu, Wanxiang Feng, Xiaodong Xu, and Wang Yao. Coupled spin and valley physics in monolayers of MoS₂ and other group-vi dichalcogenides. *Physical Review Letters*, 108(19):196802, 2012.
- [41] Alejandro Molina-Sánchez, Davide Sangalli, Kerstin Hummer, Andrea Marini, and Ludger Wirtz. Effect of spin-orbit interaction on the optical spectra of single-layer, double-layer, and bulk MoS₂. *Physical Review B*, 88(4):045412, 2013.
- [42] Ting Cao, Gang Wang, Wenpeng Han, Huiqi Ye, Chuanrui Zhu, Junren Shi, Qian Niu, Pingheng Tan, Enge Wang, Baoli Liu, and Ji Feng. Valley-selective circular dichroism of monolayer molybdenum disulphide. *Nature Communications*, 3(1):1–5, 2012.
- [43] Aaron M Jones, Hongyi Yu, Nirmal J Ghimire, Sanfeng Wu, Grant Aivazian, Jason S Ross, Bo Zhao, Jiaqiang Yan, David G Mandrus, Di Xiao, Yao Wang, and Xiaodong Xu. Optical generation of excitonic valley coherence in monolayer WSe₂. *Nature Nanotechnology*, 8(9):634, 2013.
- [44] Tao Yu and Mingwei Wu. Valley depolarization due to intervalley and intravalley electron-hole exchange interactions in monolayer MoS₂. *Physical Review B*, 89(20):205303, 2014.
- [45] Mikhail M Glazov, Thierry Amand, Xavier Marie, Delphine Lagarde, Louis Bouet, and Bernhard Urbaszek. Exciton fine structure and spin decoherence in monolayers of transition metal dichalcogenides. *Physical Review B*, 89(20):201302, 2014.
- [46] Lee A Walsh and Christopher L Hinkle. van der waals epitaxy: 2D materials and topological insulators. *Applied Materials Today*, 9:504–515, 2017.
- [47] Andre K Geim and Irina V Grigorieva. Van der waals heterostructures. *Nature*, 499(7459):419–425, 2013.
- [48] Kha Tran, Galan Moody, Fengcheng Wu, Xiaobo Lu, Junho Choi, Kyoungwan Kim, Amrithesh Rai, Daniel A Sanchez, Jiamin Quan, Akshay Singh, Jacob Embley, André Zepeda, Marshall Campbell, Travis Autry, Takashi Taniguchi, Kenji Watanabe, Nanshu Lu, Sanjay K. Banerjee, Kevin L. Silverman, Suenne Kim, Emanuel Tutuc, Li Yang, Allan H MacDonald and Xiaoqin Li. Evidence for moiré excitons in van der waals heterostructures. *Nature*, 567(7746):71–75, 2019.
- [49] Atsushi Koma, Kazumasa Sunouchi, and Takao Miyajima. Fabrication and characterization of heterostructures with subnanometer thickness. *Microelectronic Engineering*, 2(1-3):129–136, 1984.
- [50] Minh Tuan Dau, Maxime Gay, Daniela Di Felice, Céline Vergnaud, Alain Marty, Cyrille Beigne, Gilles Renaud, Olivier Renault, Pierre Mallet, Toai Le Quang, Jean-Yves Veuille, Loïc Huder, Vincent T Renard, Claude Chapelier, Giovanni Zamborlini, Matteo Jugovac, Vitaliy Feyrer, Yannick J Dappe, Pascal Pochet, and Matthieu Jamet. Beyond van der waals interaction: the case of MoSe₂ epitaxially grown on few-layer graphene. *ACS Nano*, 12(3):2319–2331, 2018.
- [51] Xiumei Zhang, Haiyan Nan, Shaoqing Xiao, Xi Wan, Xiaofeng Gu, Aijun Du, Zhenhua Ni, and Kostya Ken Ostrikov. Transition metal dichalcogenides bilayer single crystals by reverse-flow chemical vapor epitaxy. *Nature Communications*, 10(1):1–10, 2019.
- [52] Qinghua Zhao, Tao Wang, Yu Kyoung Ryu, Riccardo Frisenda, and Andres Castellanos-Gomez. An inexpensive system for the deterministic transfer of 2D materials. *Journal of Physics: Materials*, 2020.
- [53] Patricia Gant, Felix Carrascoso, Qinghua Zhao, Yu Kyoung Ryu, Michael Seitz, Ferry Prins, Riccardo Frisenda, and Andres Castellanos-Gomez. A system for the deterministic transfer of 2d materials under inert environmental conditions.
- [54] Bevin Huang, Genevieve Clark, Efrén Navarro-Moratalla, Dahlia R Klein, Ran Cheng, Kyle L Seyler, Ding Zhong, Emma Schmidgall, Michael A McGuire, David H Cobden, Wang Yao, Di Xiao, Pablo Jarillo-Herrero, and Xiaodong Xu. Layer-dependent ferromagnetism in a van der waals crystal down to the monolayer limit. *Nature*, 546(7657):270–273, 2017.
- [55] Yuan Cao, Valla Fatemi, Shiang Fang, Kenji Watanabe, Takashi Taniguchi, Efthimios Kaxiras, and Pablo Jarillo-Herrero. Unconventional superconductivity in magic-angle graphene superlattices. *Nature*, 556(7699):43–50, 2018.

- [56] Aaron L Sharpe, Eli J Fox, Arthur W Barnard, Joe Finney, Kenji Watanabe, Takashi Taniguchi, MA Kastner, and David Goldhaber-Gordon. Emergent ferromagnetism near three-quarters filling in twisted bilayer graphene. *Science*, 365(6453):605–608, 2019.
- [57] Chenhao Jin, Emma C Regan, Aiming Yan, M Iqbal Bakti Utama, Danqing Wang, Sihan Zhao, Ying Qin, Sijie Yang, Zhiren Zheng, Shenyang Shi, Kenji Watanabe, Takashi Taniguchi, Sefaattin Tongay, Alex Zettl, and Feng Wang. Observation of moiré excitons in WSe₂/WS₂ heterostructure superlattices. *Nature*, 567(7746):76–80, 2019.
- [58] Kyle L Seyler, Pasqual Rivera, Hongyi Yu, Nathan P Wilson, Essance L Ray, David G Mandrus, Jiaqiang Yan, Wang Yao, and Xiaodong Xu. Signatures of moiré-trapped valley excitons in MoSe₂/WSe₂ heterobilayers. *Nature*, 567(7746):66–70, 2019.
- [59] Andres Castellanos-Gomez, Michele Buscema, Rianda Molenaar, Vibhor Singh, Laurens Janssen, Herre SJ Van Der Zant, and Gary A Steele. Deterministic transfer of two-dimensional materials by all-dry viscoelastic stamping. *2D Materials*, 1(1):011002, 2014.
- [60] Sarah J Haigh, Ali Gholinia, Rashid Jalil, Simon Romani, Liam Britnell, Daniel C Elias, Konstantin S Novoselov, Leonid A Ponomarenko, Andre K Geim, and Roman V Gorbachev. Cross-sectional imaging of individual layers and buried interfaces of graphene-based heterostructures and superlattices. *Nature materials*, 11(9):764–767, 2012.
- [61] Filippo Pizzocchero, Lene Gammelgaard, Bjarke S Jessen, José M Caridad, Lei Wang, James Hone, Peter Bøggild, and Timothy J Booth. The hot pick-up technique for batch assembly of van der waals heterostructures. *Nature Communications*, 7(1):1–10, 2016.
- [62] Takashi Taniguchi and Kenji Watanabe. Synthesis of high-purity boron nitride single crystals under high pressure by using Ba–BN solvent. *Journal of Crystal Growth*, 303(2):525–529, 2007.
- [63] Yangdi Li, Vincent Garnier, Philippe Steyer, Catherine Journet, and Bérangère Toury. Millimeter-scale hexagonal boron nitride single crystals for nanosheet generation. *ACS Applied Nano Materials*, 3(2):1508–1515, 2020.
- [64] Der-Hsien Lien, Jeong Seuk Kang, Matin Amani, Kevin Chen, Mahmut Tosun, Hsin-Ping Wang, Tania Roy, Michael S Eggleston, Ming C Wu, Madan Dubey, Si-Chen Lee, Jr-Hau He, and Ali Javey. Engineering light outcoupling in 2D materials. *Nano Letters*, 15(2):1356–1361, 2015.
- [65] Guillaume Cassabois, Pierre Valvin, and Bernard Gil. Hexagonal boron nitride is an indirect bandgap semiconductor. *Nature Photonics*, 10(4):262, 2016.
- [66] Roman V Gorbachev, Ibtisam Riaz, Rahul R Nair, Rashid Jalil, Liam Britnell, Branson D Belle, Ernie W Hill, Kostya S Novoselov, Kenji Watanabe, Takashi Taniguchi, Andre K Geim, and Peter Blake. Hunting for monolayer boron nitride: optical and raman signatures. *Small*, 7(4):465–468, 2011.
- [67] Claus F Klingshirm. *Semiconductor optics*. Springer Science & Business Media, 2012.
- [68] Eugenius L Ivchenko. *Optical spectroscopy of semiconductor nanostructures*. Alpha Science Int’l Ltd., 2005.
- [69] Lifshitz D Landau and E. M. Lifshitz. *Statistical physics*. butterwoth-hinemann, 2000.
- [70] Emmanuel Courtade, Marina Semina, Marco Manca, Mikhail M Glazov, Cédric Robert, Fabian Cadiz, Gang Wang, Takashi Taniguchi, Kenji Watanabe, Mathieu Pierre, Walter Escoffier, Eougenious L Ivchenko, Pierre Renucci, Xavier Marie, Thierry Amand and Bernhard Urbaszek. Charged excitons in monolayer WSe₂: experiment and theory. *Physical Review B*, 96(8):085302, 2017.
- [71] Gang Wang, Cédric Robert, Mikhail M Glazov, Fabian Cadiz, Emmanuel Courtade, Thierry Amand, Delphine Lagarde, Takashi Taniguchi, Kenji Watanabe, Bernhard Urbaszek, and Xavier Marie. In-plane propagation of light in transition metal dichalcogenide monolayers: optical selection rules. *Physical Review Letters*, 119(4):047401, 2017.
- [72] Xiao-Xiao Zhang, Ting Cao, Zhengguang Lu, Yu-Chuan Lin, Fan Zhang, Ying Wang, Zhiqiang Li, James C Hone, Joshua A Robinson, Dmitry Smirnov, Steven G Louie and Tony F Heinz. Magnetic brightening and control of dark excitons in monolayer WSe₂. *Nature Nanotechnology*, 12(9):883, 2017.
- [73] Samuel Brem, August Ekman, Dominik Christiansen, Florian Katsch, Malte Selig, Cedric Robert, Xavier Marie, Bernhard Urbaszek, Andreas Knorr, and Ermin Malic. Phonon-assisted photoluminescence from indirect excitons in monolayers of transition-metal dichalcogenides. *Nano Letters*, 20(4):2849–2856, 2020.
- [74] K. K. Hamamatsu Photonics. Guide to streak camera. *Hamamatsu, Hamamatsu City Japan*, 2010.
- [75] Fabian Cadiz, Emmanuel Courtade, Cédric Robert, Gang Wang, Y Shen, Hui Cai, Takashi Taniguchi, Kenji Watanabe, Helene Carrere, Delphine Lagarde, Marco Manca, Thierry Amand, Pierre Renucci, Sefaattin Tongay, Xavier Marie, and Bernhard Urbaszek. Excitonic linewidth approaching the homogeneous limit in MoS₂-based van der waals heterostructures. *Physical Review X*, 7(2):021026, 2017.

- [76] Cory R Dean, Andrea F Young, Inanc Meric, Chris Lee, Lei Wang, Sebastian Sorgenfrei, Kenji Watanabe, Takashi Taniguchi, Phillip Kim, Kenneth L Shepard, and James Hone. Boron nitride substrates for high-quality graphene electronics. *Nature Nanotechnology*, 5(10):722–726, 2010.
- [77] Fabian Cadiz, Cédric Robert, Gang Wang, Wilson Kong, Xi Fan, Mark Blei, Delphine Lagarde, Maxime Gay, Marco Manca, Takashi Taniguchi, Kenji Watanabe, Thierry Amand, Xavier Marie, Pierre Renucci, Sefaattin Tongay, and Bernhard Urbaszek. Ultra-low power threshold for laser induced changes in optical properties of 2D molybdenum dichalcogenides. *2D Materials*, 3(4):045008, 2016.
- [78] Xiao-Xiao Zhang, Yumeng You, Shu Yang Frank Zhao, and Tony F Heinz. Experimental evidence for dark excitons in monolayer WSe₂. *Physical Review Letters*, 115(25):257403, 2015.
- [79] F Withers, O Del Pozo-Zamudio, S Schwarz, S Dufferwiel, PM Walker, T Godde, AP Rooney, A Gholinia, CR Woods, P Blake, SJ Haigh, K Watanabe, T Taniguchi, IL Aleiner, AK Geim, VI Fal’ko, AI Tartakovskii, and KS Novoselov. WSe₂ light-emitting tunneling transistors with enhanced brightness at room temperature. *Nano Letters*, 15(12):8223–8228, 2015.
- [80] Ashish Arora, Karol Nogajewski, Maciej Molas, Maciej Koperski, and Marek Potemski. Exciton band structure in layered MoSe₂: from a monolayer to the bulk limit. *Nanoscale*, 7(48):20769–20775, 2015.
- [81] Anna Vinattieri, Jagdeep Shah, TC Damen, DaiSik Kim, Loren N Pfeiffer, Marcelo Zoega Maialle, and Lu Jeu Sham. Exciton dynamics in GaAs quantum wells under resonant excitation. *Physical Review B*, 50(15):10868, 1994.
- [82] Min Yang, Cedric Robert, Zhengguang Lu, Dinh Van Tuan, Dmitry Smirnov, Xavier Marie, and Hanan Dery. Exciton valley depolarization in monolayer transition-metal dichalcogenides. *Physical Review B*, 101(11):115307, 2020.
- [83] Maciej R Molas, Autur O Slobodeniuk, Tomasz Kazimierzczuk, Karol Nogajewski, Miroslav Bartos, Piotr Kapuściński, Kacper Oreszczuk, Kenji Watanabe, Takashi Taniguchi, Clément Faugeras, Piotr Kossacki, Denis Basko, and Marek Potemski. Probing and manipulating valley coherence of dark excitons in monolayer WSe₂. *Physical Review Letters*, 123(9):096803, 2019.
- [84] You Zhou, Giovanni Scuri, Dominik S Wild, Alexander A High, Alan Dibos, Luis A Jauregui, Chi Shu, Kristiaan De Greve, Kateryna Pistunova, Andrew Y Joe, Takashi Taniguchi, Kenji Watanabe, Philip Kim, Mikhail D Lukin, and Hongkun Park. Probing dark excitons in atomically thin semiconductors via near-field coupling to surface plasmon polaritons. *Nature Nanotechnology*, 12(9):856, 2017.
- [85] Cédric Robert, Thierry Amand, Fabian Cadiz, Delphine Lagarde, Emmanuel Courtade, Marco Manca, Takashi Taniguchi, Kenji Watanabe, Bernhard Urbaszek, and Xavier Marie. Fine structure and lifetime of dark excitons in transition metal dichalcogenide monolayers. *Physical Review B*, 96(15):155423, 2017.
- [86] Ermin Malic, Malte Selig, Maja Feierabend, Samuel Brem, Dominik Christiansen, Florian Wendler, Andreas Knorr, and Gunnar Berghäuser. Dark excitons in transition metal dichalcogenides. *Physical Review Materials*, 2(1):014002, 2018.
- [87] Thorsten Deilmann and Kristian Sommer Thygesen. Dark excitations in monolayer transition metal dichalcogenides. *Physical Review B*, 96(20):201113, 2017.
- [88] Diana Y Qiu, Ting Cao, and Steven G Louie. Nonanalyticity, valley quantum phases, and lightlike exciton dispersion in monolayer transition metal dichalcogenides: Theory and first-principles calculations. *Physical Review Letters*, 115(17):176801, 2015.
- [89] J.P. Echeverry, Bernhard Urbaszek, Thierry Amand, Xavier Marie, and Iann C Gerber. Splitting between bright and dark excitons in transition metal dichalcogenide monolayers. *Physical Review B*, 93(12):121107, 2016.
- [90] Maciej R Molas, Karol Nogajewski, Marek Potemski, and Adam Babiński. Raman scattering excitation spectroscopy of monolayer WS₂. *Scientific Reports*, 7(1):5036, 2017.
- [91] Hanan Dery and Yang Song. Polarization analysis of excitons in monolayer and bilayer transition-metal dichalcogenides. *Physical Review B*, 92(12):125431, 2015.
- [92] Patrick Back, Sina Zeytinoglu, Aroosa Ijaz, Martin Kroner, and Atac Imamoğlu. Realization of an electrically tunable narrow-bandwidth atomically thin mirror using monolayer MoSe₂. *Physical Review Letters*, 120(3):037401, 2018.
- [93] Maciej Koperski, Maciej R Molas, Ashish Arora, Karol Nogajewski, Artur O Slobodeniuk, Clement Faugeras, and Marek Potemski. Optical properties of atomically thin transition metal dichalcogenides: observations and puzzles. *Nanophotonics*, 6(6):1289–1308, 2017.
- [94] Thierry Amand, Xavier Marie, Pascale Le Jeune, M. Brousseau, D. Robart, J. Barrau, and R. Planel. Spin quantum beats of 2D excitons. *Physical Review Letters*, 78(7):1355, 1997.
- [95] I.V. Mashkov, C. Gourdon, P. Lavallard, and D Yu Roditchev. Exciton quantum beats in type-II GaAs/AlAs superlattices in longitudinal and in-plane magnetic fields. *Physical Review B*, 55(20):13761, 1997.

- [96] Zhengguang Lu, Daniel Rhodes, Zhipeng Li, Dinh Van Tuan, Yuxuan Jiang, Jonathan Ludwig, Zhigang Jiang, Zhen Lian, Su-Fei Shi, James Hone, Hanan Dery, and Dimitry Smirnov. Magnetic field mixing and splitting of bright and dark excitons in monolayer MoSe₂. *2D Materials*, 7(1):015017, 2019.
- [97] Cédric Robert, Bo Han, Piotr Kapuscinski, Alex Delhomme, Clément Faugeras, Thierry Amand, Maciej R Molas, Miroslav Bartos, Kenji Watanabe, Takashi Taniguchi, Bernhard Urbaszek, Marek Potemski, and Xavier Marie. Measurement of the spin-forbidden dark excitons in MoS₂ and MoSe₂ monolayers. *arXiv preprint arXiv:2002.03877*, 2020.
- [98] Autur O Slobodeniuk, Maciej Koperski, Maciej R Molas, P Kossacki, Karol Nogajewski, Miroslav Bartos, Kenji Watanabe, Takashi Taniguchi, Clément Faugeras, and Marek Potemski. Fine structure of k-excitons in multilayers of transition metal dichalcogenides. *2D Materials*, 6(2):025026, 2019.
- [99] Mateusz M Goryca, Jing Li, Andreas V Stier, Takashi Taniguchi, Kenji Watanabe, Emmanuel Courtade, Shivangi Shree, Cédric Robert, Bernhard Urbaszek, Xavier Marie, and Scott A Crooker. Revealing exciton masses and dielectric properties of monolayer semiconductors with high magnetic fields. *Nature Communications*, 10(1):1–12, 2019.
- [100] Riccardo Pisoni, Andor Kormányos, Matthew Brooks, Zijin Lei, Patrick Back, Marius Eich, Hiske Overweg, Yongjin Lee, Peter Rickhaus, Kenji Watanabe, Takashi Taniguchi, Ataç İmamoğlu, Guido Burkard, Thomas Ihn, and Klaus Ensslin. Interactions and magnetotransport through spin-valley coupled landau levels in monolayer MoS₂. *Physical Review Letters*, 121(24):247701, 2018.
- [101] Jonas Gaël Roch, Guillaume Froehlicher, Nadine Leisgang, Peter Makk, Kenji Watanabe, Takashi Taniguchi, and Richard John Warburton. Spin-polarized electrons in monolayer MoS₂. *Nature Nanotechnology*, 14(5):432–436, 2019.
- [102] Maciej R Molas, Clément Faugeras, Autur O Slobodeniuk, Karol Nogajewski, Miroslav Bartos, D. M. Basko, and Marek Potemski. Brightening of dark excitons in monolayers of semiconducting transition metal dichalcogenides. *2D Materials*, 4(2):021003, 2017.
- [103] Yang Song and Hanan Dery. Transport theory of monolayer transition-metal dichalcogenides through symmetry. *Physical Review Letters*, 111:026601, 2013.
- [104] Zhenghe Jin, Xiaodong Li, Jeffrey T Mullen, and Ki Wook Kim. Intrinsic transport properties of electrons and holes in monolayer transition-metal dichalcogenides. *Physical Review B*, 90:045422, 2014.
- [105] Gang Wang, Étienne Palleau, Thierry Amand, Sefaattin Tongay, Xavier Marie, and Bernhard Urbaszek. Polarization and time-resolved photoluminescence spectroscopy of excitons in MoSe₂ monolayers. *Applied Physics Letters*, 106(11):112101, 2015.
- [106] Cédric Robert, Raphaël Picard, Delphine Lagarde, Gang Wang, J.P. Echeverry, Fabian Cadiz, Pierre Renucci, Alexander Högele, Thierry Amand, Xavier Marie, Iann C Gerber, and Bernhard Urbaszek. Excitonic properties of semiconducting monolayer and bilayer MoTe₂. *Physical Review B*, 94(15):155425, 2016.
- [107] Hans Tornatzky, Anne-Marie Kaulitz, and Janina Maultzsch. Resonance profiles of valley polarization in single-layer MoS₂ and MoSe₂. *Physical Review Letters*, 121(16):167401, 2018.
- [108] Gregory Sallen, Louis Bouet, Xavier Marie, Gang Wang, Chuanrui Zhu, Wenpeng Han, Y. Lu, Pingheng Tan, Thierry Amand, Baoli Liu, and Bernhard Urbaszek. Robust optical emission polarization in MoS₂ monolayers through selective valley excitation. *Physical Review B*, 86(8):081301, 2012.
- [109] Kin Fai Mak, Keliang He, Jie Shan, and Tony F Heinz. Control of valley polarization in monolayer MoS₂ by optical helicity. *Nature Nanotechnology*, 7(8):494–498, 2012.
- [110] Galan Moody, Chandriker Kavir Dass, Kai Hao, Chang-Hsiao Chen, Lain-Jong Li, Akshay Singh, Kha Tran, Genevieve Clark, Xiaodong Xu, Gunnar Berghäuser, Ermin Malic, Andreas Knorr, and Xiaoqin Li. Intrinsic homogeneous linewidth and broadening mechanisms of excitons in monolayer transition metal dichalcogenides. *Nature Communications*, 6(1):1–6, 2015.
- [111] Tomasz Jakubczyk, Valentin Delmonte, Maciej Koperski, Karol Nogajewski, Clément Faugeras, Wolfgang Langbein, Marek Potemski, and Jacek Kasprzak. Radiatively limited dephasing and exciton dynamics in MoSe₂ monolayers revealed with four-wave mixing microscopy. *Nano Letters*, 16(9):5333–5339, 2016.
- [112] Tomasz Jakubczyk, Karol Nogajewski, Maciej R Molas, Miroslav Bartos, Wolfgang Langbein, Marek Potemski, and Jacek Kasprzak. Impact of environment on dynamics of exciton complexes in a WS₂ monolayer. *2D Materials*, 5(3):031007, 2018.
- [113] Caroline Boule, Diana Vaclavkova, Miroslav Bartos, Karol Nogajewski, Lukas Zdražil, Takashi Taniguchi, Kenji Watanabe, Marek Potemski, and Jacek Kasprzak. Coherent dynamics and mapping of excitons in single-layer MoSe₂ and WSe₂ at the homogeneous limit. *Physical Review Materials*, 4(3):034001, 2020.

- [114] Tomasz Jakubczyk, Goutham Nayak, Lorenzo Scarpelli, Wei-Lai Liu, Sudipta Dubey, Nedjma Bendiab, Laëtitia Marty, Takashi Taniguchi, Kenji Watanabe, Francesco Masia, Gilles Nogues, Johann Coraux, Wolfgang Langbein, Julien Renard, Vincent Bouchiat, and Jacek Kasprzak. Coherence and density dynamics of excitons in a single-layer MoS₂ reaching the homogeneous limit. *ACS nano*, 13(3):3500–3511, 2019.
- [115] Eric W Martin, Jason Horng, Hanna G Ruth, Eunice Paik, Michael-Henr Wentzel, Hui Deng, and Steven T Cundiff. Encapsulation narrows excitonic homogeneous linewidth of exfoliated MoSe₂ monolayer. *arXiv preprint arXiv:1810.09834*, 2018.
- [116] Giovanni Scuri, You Zhou, Alexander A High, Dominik S Wild, Chi Shu, Kristiaan De Greve, Luis A Jauregui, Takashi Taniguchi, Kenji Watanabe, Philip Kim, Mikhail D Lukin, and Hongkun Park. Large excitonic reflectivity of monolayer MoSe₂ encapsulated in hexagonal boron nitride. *Physical Review Letters*, 120(3):037402, 2018.
- [117] Kin Fai Mak and Jie Shan. Mirrors made of a single atomic layer, 2018.
- [118] Edward M Purcell, Henry Cutler Torrey, and Robert V Pound. Resonance absorption by nuclear magnetic moments in a solid. *Physical Review*, 69(1-2):37, 1946.
- [119] Daniel Kleppner. Inhibited spontaneous emission. *Physical Review Letters*, 47(4):233, 1981.
- [120] Wonho Jhe, A. Anderson, Edwards A Hinds, D. Meschede, Luigi Moi, and Serge Haroche. Suppression of spontaneous decay at optical frequencies: Test of vacuum-field anisotropy in confined space. *Physical Review Letters*, 58(7):666, 1987.
- [121] Manfred Bayer, Thomas L Reinecke, Frank Weidner, A.V. Larionov, A. McDonald, and Alfred Forchel. Inhibition and enhancement of the spontaneous emission of quantum dots in structured microresonators. *Physical Review Letters*, 86(14):3168, 2001.
- [122] Jean-Michel Gérard, Bernard Sermage, Bruno Gayral, Bernard Legrand, Eric Costard, and Veronique Thierry-Mieg. Enhanced spontaneous emission by quantum boxes in a monolithic optical microcavity. *Physical Review Letters*, 81(5):1110, 1998.
- [123] Jean-Michel Gérard and Bruno Gayral. InAs quantum dots: artificial atoms for solid-state cavity-quantum electrodynamics. *Physica E: Low-dimensional Systems and Nanostructures*, 9(1):131–139, 2001.
- [124] Tobias Korn, Stefanie Heydrich, Michael Hirmer, Johannes Schmutzler, and Christian Schüller. Low-temperature photocarrier dynamics in monolayer MoS₂. *Applied Physics Letters*, 99(10):102109, 2011.
- [125] Delphine Lagarde, Louis Bouet, Xavier Marie, Chuanrui Zhu, Baoli Liu, Thierry Amand, Pingheng Tan, and Bernhard Urbaszek. Carrier and polarization dynamics in monolayer MoS₂. *Physical Review Letters*, 112:047401, 2014.
- [126] Cédric Robert, Delphine Lagarde, Fabian Cadiz, Gang Wang, Benjamin Lassagne, Thierry Amand, Andrea Balocchi, Pierre Renucci, Sefattin Tongay, Bernhard Urbaszek, and Xavier Marie. Exciton radiative lifetime in transition metal dichalcogenide monolayers. *Physical Review B*, 93(20):205423, 2016.
- [127] K. Tanaka, T. Nakamura, W. Takamatsu, M. Yamanishi, Y. Lee, and T. Ishihara. Cavity-induced changes of spontaneous emission lifetime in one-dimensional semiconductor microcavities. *Physical Review Letters*, 74(17):3380, 1995.
- [128] I. Abram, Isabella Robert, and R. Kuszelewicz. Spontaneous emission control in semiconductor microcavities with metallic or bragg mirrors. *IEEE Journal of quantum electronics*, 34(1):71–76, 1998.
- [129] Gertrude Bourdon, Isabella Robert, R. Adams, K. Nelep, Isabelle Sagnes, Jean-Marie Moison, and Izo Abram. Room temperature enhancement and inhibition of spontaneous emission in semiconductor microcavities. *Applied Physics Letters*, 77(9):1345–1347, 2000.
- [130] Christopher Rogers, Dodd Gray Jr, Nathan Bogdanowicz, Takashi Taniguchi, Kenji Watanabe, and Hideo Mabuchi. Coherent feedback control of two-dimensional excitons. *Physical Review Research*, 2(1):012029, 2020.
- [131] You Zhou, Giovanni Scuri, Jiho Sung, Ryan J Gelly, Dominik S Wild, Kristiaan De Greve, Andrew Y Joe, Takashi Taniguchi, Kenji Watanabe, Philip Kim, Mikhail D Lukin, and Hongkun Park. Controlling excitons in an atomically thin membrane with a mirror. *Physical Review Letters*, 124(2):027401, 2020.
- [132] Jason Horng, Yu-Hsun Chou, Tsu-Chi Chang, Chu-Yuan Hsu, Tien-Chang Lu, and Hui Deng. Engineering radiative coupling of excitons in 2D semiconductors. *Optica*, 6(11):1443–1448, 2019.
- [133] Gang Wang, Louis Bouet, Delphine Lagarde, Maël Vidal, Andrea Balocchi, Thierry Amand and Xavier Marie, and Bernhard Urbaszek. Valley dynamics probed through charged and neutral exciton emission in monolayer WSe₂. *Physical Review B*, 90(7):075413, 2014.
- [134] Yia-Chung Chang, Shiue-Yuan Shiau, and Monique Combescot. Crossover from trion-hole complex to exciton-polaron in n-doped two-dimensional semiconductor quantum wells. *Physical Review B*, 98(23):235203, 2018.

- [135] Samuel Brem, Malte Selig, Gunnar Berghäuser, and Ermin Malic. Exciton relaxation cascade in two-dimensional transition metal dichalcogenides. *Scientific Reports*, 8(1):1–8, 2018.
- [136] Malte Selig, Gunnar Berghäuser, Archana Raja, Philipp Nagler, Christian Schüller, Tony F Heinz, Tobias Korn, Alexey Chernikov, Ermin Malic, and Andreas Knorr. Excitonic linewidth and coherence lifetime in monolayer transition metal dichalcogenides. *Nature Communications*, 7:13279, 11 2016.
- [137] Ruben Maas, James Parsons, Nader Engheta, and Albert Polman. Experimental realization of an epsilon-near-zero metamaterial at visible wavelengths. *Nature Photonics*, 7(11):907–912, 2013.
- [138] W. Seidel, A. N. Titkov, J. P. André, P. Voisin, and M. Voos. High-efficiency energy up-conversion by an "Auger fountain" at an InP-AlInAs type-ii heterojunction. *Physical Review Letters*, 73(17):2356–2359, 1994.
- [139] Robert Hellmann, Anna Euteneuer, S.G. Hense, Joachim Feldmann, P. Thomas, Ernst O Göbel, Dmitri R Yakovlev, Andreas Waag, and Gottfried Landwehr. Low-temperature anti-stokes luminescence mediated by disorder in semiconductor quantum-well structures. *Physical Review B*, 51:18053–18056, 1995.
- [140] Ehud Poles, Donald C Selmarten, Olga I Micić, and Arthur J Nozik. Anti-stokes photoluminescence in colloidal semiconductor quantum dots. *Applied Physics Letters*, 75(7):971–973, 1999.
- [141] Plamen P Paskov, Per Olof Holtz, Bo Monemar, Jorge M Garcia, Winston V Schoenfeld, and Pierre M Petroff. Photoluminescence up-conversion in InAs/GaAs self-assembled quantum dots. *Applied Physics Letters*, 77(6):812–814, 2000.
- [142] Hsiao-Hwa Chen, Jan E Stehr, Nandanapalli Koteeswara Reddy, Charles W Tu, Weimin Chen, and Irina A Buyanova. Efficient upconversion of photoluminescence via two-photon absorption in bulk and nanorod ZnO. *Applied Physics B*, 108(4):919–924, 2012.
- [143] Aaron M Jones, Hongyi Yu, John R Schaibley, Jiaqiang Yan, David G Mandrus, Takashi Taniguchi, Kenji Watanabe, Hanan Dery, Wang Yao, and Xiaodong Xu. Excitonic luminescence upconversion in a two-dimensional semiconductor. *Nature Physics*, 12(4):323, 2016.
- [144] Marco Manca, Mikhail M Glazov, Cédric Robert, Fabian Cadiz, Takashi Taniguchi, Kenji Watanabe, Emmanuel Courtade, Thierry Amand, Pierre Renucci, Xavier Marie, Gang Wang, and Bernhard Urbaszek. Enabling valley selective exciton scattering in monolayer WSe₂ through upconversion. *Nature Communications*, 8:14927, 2017.
- [145] Scott Dufferwiel, Thomas P Lyons, Dmitry D Solnyshkov, Aurélien A.P. Trichet, Freddie Withers, Stefan Schwarz, Guillaume Malpuech, Jason M Smith, Konstantin S Novoselov, Maurice S Skolnick, Dmitry N Krizhanovskii, and Alexander I Tartakovskii. Valley-addressable polaritons in atomically thin semiconductors. *Nature Photonics*, 11(8):497, 2017.
- [146] Nils Lundt, Aleksander Marynski, Evgeniia Cherotchenko, Anupum Pant, Xi Fan, Sefattin Tongay, Grzegorz Sek, Alexey V Kavokin, Sven Höfling, and Christian Schneider. Monolayered MoSe₂: a candidate for room temperature polaritons. *2D Materials*, 4(1):015006, 2016.
- [147] Giovanni Scuri, You Zhou, Alexander A High, Dominik S Wild, Chi Shu, Kristiaan De Greve, Luis A Jauregui, Takashi Taniguchi, Kenji Watanabe, Philip Kim, Mikhail D Lukin, and Hongkun Park. Large excitonic reflectivity of monolayer MoSe₂ encapsulated in hexagonal boron nitride. *Physical Review Letters*, 120(3):037402, 2018.
- [148] Patrick Back, Meinrad Sidler, Ovidiu Cotlet, Ajit Srivastava, Naotomo Takemura, Martin Kroner, and Atac Imamoglu. Giant paramagnetism-induced valley polarization of electrons in charge-tunable monolayer MoSe₂. *Physical Review Letters*, 118(23):237404, 2017.
- [149] Kai Hao, Lixiang Xu, Philipp Nagler, Akshay Singh, Kha Tran, Chandriker Kavir Dass, Christian Schuller, Tobias Korn, Xiaoqin Li, and Galan Moody. Coherent and incoherent coupling dynamics between neutral and charged excitons in monolayer MoSe₂. *Nano Letters*, 16(8):5109–5113, 2016.
- [150] Jason S Ross, Sanfeng Wu, Hongyi Yu, Nirmal J Ghimire, Aaron M Jones, Grant Aivazian, Jiaqiang Yan, David G Mandrus, Di Xiao, Wang Yao, and Xiaodong Xu. Electrical control of neutral and charged excitons in a monolayer semiconductor. *Nature Communications*, 4:1474, 2013.
- [151] Gang Wang, Iann C Gerber, Louis Bouet, Delphine Lagarde, Andrea Balocchi, Maël Vidal, Thierry Amand, Xavier Marie, and Bernhard Urbaszek. Exciton states in monolayer MoSe₂: impact on interband transitions. *2D Materials*, 2(4):045005, 2015.
- [152] Shivangi Shree, Marina Semina, Cédric Robert, Bo Han, Thierry Amand, Andrea Balocchi, Marco Manca, Emmanuel Courtade, Xavier Marie, Takashi Taniguchi, Kenji Watanabe, Mikhail M Glazov and Bernhard Urbaszek. Observation of exciton-phonon coupling in MoSe₂ monolayers. *Physical Review B*, 98(3):035302, 2018.
- [153] Mikhail M Glazov, Leonid E Golub, Gang Wang, Xavier Marie, Thierry Amand, and Bernhard Urbaszek. Intrinsic exciton-state mixing and nonlinear optical properties in transition metal dichalcogenide monolayers. *Physical Review B*, 95(3):035311, 2017.

- [154] Ya-Qing Bie, Gabriele Grosso, Mikkel Heuck, Marco M Furchi, Yuan Cao, Jiabao Zheng, Darius Bunandar, Efren Navarro-Moratalla, Lin Zhou, Dmitri K Efetov, Takashi Taniguchi, Kenji Watanabe, Jing Kong, Dirk Englund, and Pablo Jarillo-Herrero. A MoTe₂-based light-emitting diode and photodetector for silicon photonic integrated circuits. *Nature Nanotechnology*, 12(12):1124, 2017.
- [155] Chongyun Jiang, Fucui Liu, Jorge Cuadra, Zumeng Huang, Ke Li, Abdullah Rasmita, Ajit Srivastava, Zheng Liu, and Wei-Bo Gao. Zeeman splitting via spin-valley-layer coupling in bilayer MoTe₂. *Nature Communications*, 8(1):802, 2017.
- [156] Thomas Goldstein, Shao-Yu Chen, Jiayue Tong, Di Xiao, Ashwin Ramasubramaniam, and Jun Yan. Raman scattering and anomalous stokes-anti-stokes ratio in MoTe₂ atomic layers. *Scientific Reports*, 6:28024, 2016.
- [157] Seunghyun Song, Dong Hoon Keum, Suyeon Cho, David Perello, Yunseok Kim, and Young Hee Lee. Room temperature semiconductor-metal transition of MoTe₂ thin films engineered by strain. *Nano Letters*, 16(1):188–193, 2015.
- [158] Yao Li, Karel-Alexander N Duerloo, Kerry Wauson, and Evan J Reed. Structural semiconductor-to-semimetal phase transition in two-dimensional materials induced by electrostatic gating. *Nature Communications*, 7:10671, 2016.
- [159] Ying Wang, Jun Xiao, Hanyu Zhu, Yao Li, Yousif Alsaied, King Yan Fong, Yao Zhou, Siqi Wang, Wu Shi, Yuan Wang, Alex Zettl, Evan J Reed, and Xiang Zhang. Structural phase transition in monolayer MoTe₂ driven by electrostatic doping. *Nature*, 550(7677):487, 2017.
- [160] D. Rhodes, D. A. Chenet, B. E. Janicek, C. Nyby, Y. Lin, W. Jin, D. Edelberg, E. Mannebach, N. Finney, A. Antony, T. Schiros, T. Klarr, A. Mazzoni, M. Chin, Y.-c Chiu, W. Zheng, Q. R. Zhang, F. Ernst, J. I. Dadap, X. Tong, J. Ma, R. Lou, S. Wang, T. Qian, H. Ding, R. M. Osgood, D. W. Paley, A. M. Lindenberg, P. Y. Huang, A. N. Pasupathy, M. Dubey, J. Hone, and L. Balicas. Engineering the structural and electronic phases of MoTe₂ through W substitution. *Nano Letters*, 17(3):1616–1622, 2017.
- [161] Claudia Ruppert, Ozgur Burak Aslan, and Tony F Heinz. Optical properties and band gap of single-and few-layer MoTe₂ crystals. *Nano Letters*, 14(11):6231–6236, 2014.
- [162] Ignacio Gutiérrez Lezama, Ashish Arora, Alberto Ubaldini, Céline Barreateau, Enrico Giannini, Marek Potemski, and Alberto F Morpurgo. Indirect-to-direct band gap crossover in few-layer MoTe₂. *Nano Letters*, 15(4):2336–2342, 2015.
- [163] Guillaume Froehlicher, Etienne Lorchat, and Stéphane Berciaud. Direct versus indirect band gap emission and exciton-exciton annihilation in atomically thin molybdenum ditelluride MoTe₂. *Physical Review B*, 94(8):085429, 2016.
- [164] Ashwin Ramasubramaniam. Large excitonic effects in monolayers of molybdenum and tungsten dichalcogenides. *Physical Review B*, 86(11):115409, 2012.
- [165] Natalia S Rytova. Screened potential of a point charge in a thin film. *Moscow University Physics Bulletin*, 3:30, 1967 [arXiv:1806.00976].
- [166] Leonid V Keldysh. Coulomb interaction in thin semiconductor and semimetal films. *Soviet Journal of Experimental and Theoretical Physics Letters*, 29:658, 1979.
- [167] Chenhao Jin, Jonghwan Kim, Joonki Suh, Zhiwen Shi, Bin Chen, Xi Fan, Matthew Kam, Kenji Watanabe, Takashi Taniguchi, Sefaattin Tongay, Alex Zettl, Junqiao Wu, and Feng Wang. Interlayer electron-phonon coupling in WSe₂/hBN heterostructures. *Nature Physics*, 13(2):127, 2017.
- [168] Colin Ming Earn Chow, Hongyi Yu, Aaron Mitchell Jones, Jiaqiang Yan, David G Mandrus, Takashi Taniguchi, Kenji Watanabe, Wang Yao, and Xiaodong Xu. Unusual exciton-phonon interactions at van der waals engineered interfaces. *Nano Letters*, 2017.
- [169] Obafunso A Ajayi, Jenny V Ardelean, Gabriella D Shepard, Jue Wang, Abhinandan Antony, Takeshi Taniguchi, Kenji Watanabe, Tony F Heinz, Stefan Strauf, Xiaoyang Zhu, and James Hone. Approaching the intrinsic photoluminescence linewidth in transition metal dichalcogenide monolayers. *2D Materials*, 4(3):031011, 2017.
- [170] Zefang Wang, Jie Shan, and Kin Fai Mak. Valley-and spin-polarized landau levels in monolayer WSe₂. *Nature Nanotechnology*, 12(2):144, 2017.
- [171] Jakob Wierzbowski, Julian Klein, Florian Sigger, Christian Straubinger, Malte Kremser, Takashi Taniguchi, Kenji Watanabe, Ursula Wurstbauer, Alexander W Holleitner, Michael Kaniber, Kai Müller, and Jonathan J Finley. Direct exciton emission from atomically thin transition metal dichalcogenide heterostructures near the lifetime limit. *Scientific Reports*, 7(1):12383, 2017.
- [172] Jiong Yang, Tieyu Lu, Ye Win Myint, Jiajie Pei, Daniel Macdonald, Jin-Cheng Zheng, and Yuerui Lu. Robust excitons and trions in monolayer MoTe₂. *ACS Nano*, 9(6):6603–6609, 2015.

- [173] Huaihong Guo, Teng Yang, Mahito Yamamoto, Lin Zhou, Ryo Ishikawa, Keiji Ueno, Kazuhito Tsukagoshi, Zhidong Zhang, Mildred S. Dresselhaus, and Riichiro Saito. Double resonance raman modes in monolayer and few-layer MoTe_2 . *Physical Review B*, 91(20):205415, 2015.
- [174] Philipp Tonndorf, Robert Schmidt, Philipp Böttger, Xiao Zhang, Janna Börner, Andreas Liebig, Manfred Albrecht, Christian Kloc, Ovidiu Gordan, Dietrich R.T. Zahn, Steffen Michaelis de Vasconcellos, and Rudolf Bratschitsch. Photoluminescence emission and raman response of monolayer MoS_2 , MoSe_2 , and WSe_2 . *Optics Express*, 21(4):4908–4916, 2013.
- [175] Bruno R Carvalho, Leandro M Malard, Juliana M Alves, Cristiano Fantini, and Marcos A Pimenta. Symmetry-dependent exciton-phonon coupling in 2D and bulk MoS_2 observed by resonance raman scattering. *Physical Review Letters*, 114(13):136403, 2015.
- [176] Gang Wang, Mikhail M Glazov, Cédric Robert, Thierry Amand, Xavier Marie, and Bernhard Urbaszek. Double resonant raman scattering and valley coherence generation in monolayer WSe_2 . *Physical Review Letters*, 115(11):117401, 2015.
- [177] Pedro Soubelet, Alex E Bruchhausen, Alejandro Fainstein, Karol Nogajewski, and Clément Faugeras. Resonance effects in the raman scattering of monolayer and few-layer MoSe_2 . *Physical Review B*, 93(15):155407, 2016.
- [178] Shao-Yu Chen, Thomas Goldstein, Jiayue Tong, Takashi Taniguchi, Kenji Watanabe, and Jun Yan. Superior valley polarization and coherence of 2s excitons in monolayer WSe_2 . *Physical Review Letters*, 120(4):046402, 2018.
- [179] Andor Kormányos, Guido Burkard, Martin Gmitra, Jaroslav Fabian, Viktor Zólyomi, Neil D Drummond and Vladimir Fal’ko. k.p theory for two-dimensional transition metal dichalcogenide semiconductors. *2D Materials*, 2(2):022001, 2015.
- [180] Maxim Trushin, Mark Oliver Goerbig, and Wolfgang Belzig. Optical absorption by dirac excitons in single-layer transition-metal dichalcogenides. *Physical Review B*, 94(4):041301, 2016.
- [181] Stefano Larentis, Hema C. P. Movva, Babak Fallahazad, Kyounghwan Kim, Armand Behroozi, Takashi Taniguchi, Kenji Watanabe, Sanjay K Banerjee, and Emanuel Tutuc. Large effective mass and interaction-enhanced zeeman splitting of k -valley electrons in MoSe_2 . *Physical Review B*, 97(20):201407, 2018.
- [182] Shinichiro Mouri, Yuhei Miyauchi, Minglin Toh, Weijie Zhao, Goki Eda, and Kazunari Matsuda. Nonlinear photoluminescence in atomically thin layered WSe_2 arising from diffusion-assisted exciton-exciton annihilation.
- [183] Nardeep Kumar, Qiannan Cui, Frank Ceballos, Dawei He, Yongsheng Wang, and Hui Zhao. Exciton-exciton annihilation in MoSe_2 monolayers. *Physical Review B*, 89(12):125427, 2014.
- [184] V. N. Abakumov, V. I. Perel, and I. N. Yassievich. *Nonradiative recombination in semiconductors*. North Holland, Amsterdam, 1991.
- [185] Georgios M Kavoulakis and Gordon Baym. Auger decay of degenerate and bose-condensed excitons in Cu_2O . *Physical Review B*, 54(23):16625–16636, 1996.
- [186] Feng Wang, Yang Wu, Mark S Hybertsen, and Tony F Heinz. Auger recombination of excitons in one-dimensional systems. *Physical Review B*, 73(24):245424, 2006.
- [187] Kai-Qiang Lin, Sebastian Bange, and John M Lupton. Quantum interference in second-harmonic generation from monolayer WSe_2 . *Nature Physics*, 15(3):242–246, 2019.
- [188] Mikhail M Glazov, Thierry Amand, Xavier Marie, Delphine Lagarde, Louis Bouet, and Bernhard Urbaszek. Exciton fine structure and spin decoherence in monolayers of transition metal dichalcogenides. *Physical Review B*, 89(20):201302, 2014.
- [189] Cristiano Ciuti, Vincenzo Savona, Carlo Piermarocchi, Antonio Quattropani, and Paolo Schwendimann. Role of the exchange of carriers in elastic exciton-exciton scattering in quantum wells. 58:7926, 1998.
- [190] Vanik Shahnazaryan, Ivan Iorsh, Ivan A Shelykh, and Oleksandr Kyriienko. Exciton-exciton interaction in transition-metal dichalcogenide monolayers. *Physical Review B*, 96(11):115409, 2017.
- [191] Pierluigi Cudazzo, Ilya V Tokatly, and Angel Rubio. Dielectric screening in two-dimensional insulators: Implications for excitonic and impurity states in graphene. *Physical Review B*, 84(8):085406, 2011.
- [192] Dmitry V Rybkovskiy, Iann C Gerber, and Mikhail V Durnev. Atomically inspired k.p approach and valley zeeman effect in transition metal dichalcogenide monolayers. *Physical Review B*, 95(15):155406, 2017.
- [193] Gennadii Levikovich Bir and Grigoriï Ezekievich Pikus. *Symmetry and Strain-induced Effects in Semiconductors*. Wiley/Halsted Press, 1974.
- [194] Calvin Yi-Ping Chao and Shun Lien Chuang. Analytical and numerical solutions for a two-dimensional exciton in momentum space. *Physical Review B*, 43(8):6530, 1991.

- [195] Malte Selig, Gunnar Berghäuser, Marten Richter, Rudolf Bratschitsch, Andreas Knorr, and Ermin Malic. Dark and bright exciton formation, thermalization, and photoluminescence in monolayer transition metal dichalcogenides. *2D Materials*, 5(3):035017, 2018.
- [196] Dominik Christiansen, Malte Selig, Gunnar Berghäuser, Robert Schmidt, Iris Niehues, Robert Schneider, Ashish Arora, Steffen Michaelis de Vasconcellos, Rudolf Bratschitsch, Ermin Malic, and Andreas Knorr. Phonon sidebands in monolayer transition metal dichalcogenides. *Physical Review Letters*, 119(18):187402, 2017.
- [197] Artur O Slobodeniuk and Denis M Basko. Exciton-phonon relaxation bottleneck and radiative decay of thermal exciton reservoir in two-dimensional materials. *Physical Review B*, 94(20):205423, 2016.
- [198] Dezheng Sun, Yi Rao, Georg A Reider, Gugang Chen, Yumeng You, Louis Brzin, Avetik R Harutyunyan, and Tony F Heinz. Observation of rapid exciton-exciton annihilation in monolayer molybdenum disulfide. *Nano Letters*, 14(10):5625–5629, 2014.
- [199] Yiling Yu, Yifei Yu, Chao Xu, Andy Barrette, Kenan Gundogdu, and Linyou Cao. Fundamental limits of exciton-exciton annihilation for light emission in transition metal dichalcogenide monolayers. *Physical Review B*, 93(20):201111, 2016.
- [200] Long Yuan, Ti Wang, Tong Zhu, Mingwei Zhou, and Libai Huang. Exciton dynamics, transport, and annihilation in atomically thin two-dimensional semiconductors. *The Journal of Physical Chemistry Letters*, 8(14):3371–3379, 2017.
- [201] Yusuke Hoshi, Takashi Kuroda, Mitsuhiro Okada, Rai Moriya, Satoru Masubuchi, Kenji Watanabe, Takashi Taniguchi, Ryo Kitaura, and Tomoki Machida. Suppression of exciton-exciton annihilation in tungsten disulfide monolayers encapsulated by hexagonal boron nitrides. *Physical Review B*, 95(24):241403, 2017.
- [202] Yongzhuo Li, Jianxing Zhang, Dandan Huang, Hao Sun, Fan Fan, Jiabin Feng, Zhen Wang, and CZ Ning. Room-temperature continuous-wave lasing from monolayer molybdenum ditelluride integrated with a silicon nanobeam cavity. *Nature Nanotechnology*, 12(10):987, 2017.
- [203] Sanfeng Wu, Sonia Buckley, John R Schaibley, Liefeng Feng, Jiaqiang Yan, David G Mandrus, Fariba Hatami, Wang Yao, Jelena Vučković, Arka Majumdar, and Xiaodong Xu. Monolayer semiconductor nanocavity lasers with ultralow thresholds. *Nature*, 520(7545):69, 2015.
- [204] Alexey Chernikov, Claudia Ruppert, Heather M Hill, Albert F Rigosi, and Tony F Heinz. Population inversion and giant bandgap renormalization in atomically thin WS₂ layers. *Nature Photonics*, 9(7):466, 2015.
- [205] Ding Zhong, Kyle L Seyler, Xiayu Linpeng, Ran Cheng, Nikhil Sivadas, Bevin Huang, Emma Schmidgall, Takashi Taniguchi, Kenji Watanabe, Michael A McGuire, Wang Yao, Di Xiao, Kai-Mei C Fu, and Xiaodong Xu. Van der waals engineering of ferromagnetic semiconductor heterostructures for spin and valleytronics. *Science Advances*, 3(5):1603113, 2017.
- [206] Marco Gibertini, Maciej Koperski, Alberto F Morpurgo, and Konstantin S Novoselov. Magnetic 2D materials and heterostructures. *Nature Nanotechnology*, 14(5):408–419, 2019.
- [207] Zhaowei Zhang, Jingzhi Shang, Chongyun Jiang, Abdullah Rasmita, Weibo Gao, and Ting Yu. Direct photoluminescence probing of ferromagnetism in monolayer two-dimensional CrBr₃. *Nano Letters*, 19(5):3138–3142, 2019.
- [208] Nitin Samarth. Condensed-matter physics: Magnetism in flatland. *Nature*, 546(7657):216–218, 2017.
- [209] Cheng Gong, Lin Li, Zhenglu Li, Huiwen Ji, Alex Stern, Yang Xia, Ting Cao, Wei Bao, Chenzhe Wang, Yuan Wang, Zi Qiang Qiu, Robert J Cava, Steven G Louie, Jing Xia, and Xiang Zhang. Discovery of intrinsic ferromagnetism in two-dimensional van der waals crystals. *Nature*, 546(7657):265–269, 2017.
- [210] Kamran Shayan, Na Liu, Andrew Cupo, Yichen Ma, Yue Luo, Vincent Meunier, and Stefan Strauf. Magnetic proximity coupling of quantum emitters in WSe₂ to van der waals ferromagnets. *Nano Letters*, 19(10):7301–7308, 2019.
- [211] J. J. Hauser. Magnetic proximity effect. *Physical Review*, 187(2):580, 1969.
- [212] Benedikt Scharf, Gaofeng Xu, Alex Matos-Abiague, and Igor Žutić. Magnetic proximity effects in transition-metal dichalcogenides: converting excitons. *Physical Review Letters*, 119(12):127403, 2017.
- [213] Klaus Zollner, Paulo E Faria Junior, and Jaroslav Fabian. Proximity exchange effects in MoSe₂ and WSe₂ heterostructures with CrI₃: Twist angle, layer, and gate dependence. *Physical Review B*, 100(8):085128, 2019.
- [214] Klaus Zollner, Paulo E Faria Junior, and Jaroslav Fabian. Giant proximity exchange and valley splitting in transition metal dichalcogenide/hBN/(Co, Ni) heterostructures. *Physical Review B*, 101(8):085112, 2020.
- [215] Kyle L Seyler, Ding Zhong, Bevin Huang, Xiayu Linpeng, Nathan P Wilson, Takashi Taniguchi, Kenji Watanabe, Wang Yao, Di Xiao, Michael A McGuire, et al. Valley manipulation by optically tuning the magnetic proximity effect in wse₂/cri₃ heterostructures. *Nano letters*, 18(6):3823–3828, 2018.

- [216] Michael A McGuire, Genevieve Clark, KC Santosh, W Michael Chance, Gerald E Jellison Jr, Valentino R Cooper, Xiaodong Xu, and Brian C Sales. Magnetic behavior and spin-lattice coupling in cleavable van der waals layered CrCl_3 crystals. *Physical Review Materials*, 1(1):014001, 2017.
- [217] Michael A McGuire. Crystal and magnetic structures in layered, transition metal dihalides and trihalides. *Crystals*, 7(5):121, 2017.
- [218] Michael A McGuire, Hemant Dixit, Valentino R Cooper, and Brian C Sales. Coupling of crystal structure and magnetism in the layered, ferromagnetic insulator CrI_3 . *Chemistry of Materials*, 27(2):612–620, 2015.
- [219] Kyle L Seyler, Ding Zhong, Dahlia R Klein, Shiyuan Gao, Xiaou Zhang, Bevin Huang, Efrén Navarro-Moratalla, Li Yang, David H Cobden, Michael A McGuire, Wang Yao, Di Xiao, Pablo Jarillo-Herrero, and Xiaodong Xu. Ligand-field helical luminescence in a 2D ferromagnetic insulator. *Nature Physics*, 14(3):277–281, 2018.
- [220] Chuan Zhao, Tenzin Norden, Peiyao Zhang, Puqin Zhao, Yingchun Cheng, Fan Sun, James P Parry, Payam Taheri, Jieqiong Wang, Yihang Yang, Thomas Scrace, Kaifei Kang, Sen Yang, Guo-xing Miao, Renat Sabirianov, George Kioseoglou, Wei Huang, Athos Petrou, and Hao Zeng. Enhanced valley splitting in monolayer WSe_2 due to magnetic exchange field. *Nature Nanotechnology*, 12(8):757, 2017.
- [221] Qingyun Zhang, Shengyuan A Yang, Wenbo Mi, Yingchun Cheng, and Udo Schwingenschlögl. Large spin-valley polarization in monolayer MoTe_2 on top of EuO (111). *Advanced Materials*, 28(5):959–966, 2016.
- [222] Anike Purbawati, Johann Coraux, Jan Vogel, Abdellali Hadj-Azzem, NianJheng Wu, Nedjma Bendiab, David Jegouso, Julien Renard, Laëtizia Marty, Vincent Bouchiat, André Sulpice, Lucia Aballe, Michael Foerster, Francesca Genuzio, Andrea Locatelli, Tevfik Onur Mentese, Zheng Han, Xingdan Sun, Manuel Núñez-Regueiro, and Nicolas Rougemaille. In-plane magnetic domains and néel-like domain walls in thin flakes of the room temperature CrTe_2 van der waals ferromagnet. *ACS Applied Materials & Interfaces*, 2020.
- [223] Xingdan Sun, Wanying Li, Xiao Wang, Qi Sui, Tongyao Zhang, Zhi Wang, Long Liu, Da Li, Shun Feng, Siyu Zhong, Hanwen Wang, Vincent Bouchiat, Manuel Nunez Regueiro, Nicolas Rougemaille, Johann Coraux, Zhenhua Wang, Baojuan Dong, Xing Wu, Teng Yang, Guoqiang Yu, Bingwu Wang, Zheng Vitto Han, Xiufeng Han, and Zhidong Zhang. Room temperature 2D ferromagnetism in few-layered 1T- CrTe_2 . arXiv preprint arXiv:1909.09797, 2019.
- [224] Thomas P Lyons, Daniel Gillard, Alejandro Molina-Sánchez, A. Misra, Freddie Withers, Paul Keatley, Aleksey Kozikov, Takashi Taniguchi, Kenji Watanabe, Konstantin S Novoselov, Joaquín Fernández Rossier, and Alexander I Tartakovskii. Interplay between spin proximity effect and charge-dependent exciton dynamics in $\text{MoSe}_2/\text{CrBr}_3$ van der waals heterostructures. *arXiv preprint arXiv:2004.04073*, 2020.
- [225] Nicolas Ubrig, Zhe Wang, Jérémie Teyssier, Takashi Taniguchi, Kenji Watanabe, Enrico Giannini, Alberto F Morpurgo, and Marco Gibertini. Low-temperature monoclinic layer stacking in atomically thin CrI_3 crystals. *2D Materials*, 7(1):015007, 2019.
- [226] Zeyuan Sun, Yangfan Yi, Tiancheng Song, Genevieve Clark, Bevin Huang, Yuwei Shan, Shuang Wu, Di Huang, Chunlei Gao, Zhanghai Chen, Michael McGuire, Ting Cao, Di Xiao, Wei-Tao Liu, Wang Yao, Xiaodong Xu, and Shiwei Wu. Giant nonreciprocal second-harmonic generation from antiferromagnetic bilayer CrI_3 . *Nature*, 572(7770):497–501, 2019.
- [227] Tiancheng Song, Zaiyao Fei, Matthew Yankowitz, Zhong Lin, Qianni Jiang, Kyle Hwangbo, Qi Zhang, Bosong Sun, Takashi Taniguchi, Kenji Watanabe, Michael A McGuire, David Graf, Ting Cao, Jiun-Haw Chu, David H Cobden, Cory R Dean, Di Xiao, and Xiaodong Xu. Switching 2D magnetic states via pressure tuning of layer stacking. *Nature Materials*, pages 1–5, 2019.
- [228] Livio Ciorciaro, Martin Kroner, Kenji Watanabe, Takashi Taniguchi, and Ataç İmamoğlu. Observation of magnetic proximity effect using resonant optical spectroscopy of an electrically tunable $\text{MoSe}_2/\text{CrBr}_3$ heterostructure. *Physical Review Letters*, 124(19):197401, 2020.
- [229] Chenhao Jin, Zui Tao, Kaifei Kang, Kenji Watanabe, Takashi Taniguchi, Kin Fai Mak, and Jie Shan. Imaging and control of critical fluctuations in two-dimensional magnets. *Nature Materials*, pages 1–5, 2020.
- [230] Yujun Deng, Yijun Yu, Yichen Song, Jingzhao Zhang, Nai Zhou Wang, Zeyuan Sun, Yangfan Yi, Yi Zheng Wu, Shiwei Wu, Junyi Zhu, Jing Wang, Xian Hui Chen, and Yuanbo Zhang. Gate-tunable room-temperature ferromagnetism in two-dimensional Fe_3GeTe_2 . *Nature*, 563(7729):94–99, 2018.
- [231] Junho Seo, Duck Young Kim, Eun Su An, Kyoo Kim, Gi-Yeop Kim, Soo-Yoon Hwang, Dong Wook Kim, Bo Gyu Jang, Heejung Kim, Gyeongsik Eom, Seung Young Seo, Roland Staniai, Matthias Muntwiler, Jinwon Lee, Kenji Watanabe, Takashi Taniguchi, Youn Jung Jo, Jieun Lee, Byung Il Min, Moon Ho Jo, Han Woong Yeom, Si-Young Choi, Ji Hoon Shim, and Jun Sung Kim. Nearly room temperature ferromagnetism in a magnetic metal-rich van der waals metal. *Science Advances*, 6(3):eaay8912, 2020.
- [232] Dmitry Shcherbakov, Petr Stepanov, Daniel Weber, Yaxian Wang, Jin Hu, Yanglin Zhu, Kenji Watanabe, Takashi Taniguchi, Zhiqiang Mao, Wolfgang Windl, Joshua Goldberger, Marc Bockrath, and Chun Ning Lau. Raman spectroscopy, photocatalytic degradation, and stabilization of atomically thin chromium tri-iodide. *Nano Letters*, 18(7):4214–4219, 2018.